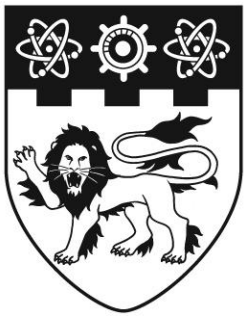

NANYANG TECHNOLOGICAL UNIVERSITY

CARBON DOPED SILICON OXIDES FOR LOW K DIELECTRIC APPLICATIONS IN MULTILEVEL INTERCONNECTS

CARBON DOPED SILICON OXIDES FOR LOW K DIELECTRIC APPLICATIONS IN MULTILEVEL INTERCONNECTS

LIU BO

LIU BO

SCHOOL OF ELECTRICAL & ELECTRONIC ENGINEERING

2008

2008

Carbon Doped Silicon Oxides for Low K Dielectric Applications in Multilevel Interconnects

Liu Bo

School of Electrical & Electronic Engineering

A thesis submitted to the Nanyang Technological University
in fulfilment of the requirement for the degree of
Master of Engineering

2008

Statement of Originality

I hereby certify that the work embodied in this thesis is the result of original research and has not been submitted for a higher degree to any other University or Institution.

Date

Liu Bo

Acknowledgement

First of all, I would like to express my most sincere gratitude to my supervisor Dr. Wong Kin Shun, Associate Professor of Division of Microelectronics, for his generous support, consistent guidance and invaluable advice throughout the project. Without his insightful and highly intelligent advice and guidance, I would not have proceeded so far and learned so much!

I am very grateful to Dr. Foo Pang Dow, Dr. Li Chao Yong, Mr. Babu Narayanan, Mr. Wang Min Rui, Mr. Xie Jie Lin, Dr. Wu Shao Yu, Dr. Yu Ming Bin, and other members from Deep Submicron Integration Circuits (DSICs) department of Institute of Microelectronics (IME) for their support, guidance and fruitful discussion.

My sincere appreciations go to Dr. Valeri Ligatchev for his advice and inspiration. Special thanks also go to Associate Professor Dr. Rusli, Associate Professor Dr. Zhang Dao Hua, Dr. Yang Lie Yong and all other members of Low-k Material Group for their encouragement, discussion and assistance.

I am deeply indebted to Professor Dr. Tay Beng Kang and his staff/students Dr. Sun Zhuo, Dr. Pan-Li Kun, Dr. Zhao Zhi-Wei, Dr. Zhang Ping, and all other members in Ion Beam Process Lab for their kindly guidance. Also thanks to all the technicians in Lab of Clean Room, Sensor, and Photonic II for their kindly support.

This work is partially supported by the Agency of Science, Technology and Research under Grant No. EMT/00/003.

Summary

Dielectric materials with lower permittivity (low k) are required for multilevel interconnect to reduce the propagation delay time, cross-talk noise and power dissipation in deep submicron integrated circuit. In this project, carbon-doped hydrogenated silicon oxide (SiOCH) films, a kind of hybrid films with both organic and inorganic components, have been investigated as a potential low k material. The films are deposited on p-type Si (100) substrates in plasma-enhanced chemical vapor deposition (PECVD) system with trimethylsilane (3MS) and oxygen as precursors at different deposited conditions. The deposition rate, bonding structure, electrical and mechanical properties have been studied with several techniques including nanoindentation, ellipsometry, atomic-force microscope (AFM), Fourier transform infrared (FTIR) spectroscopy, contact angle and C–V measurement techniques.

The first part of this project explored the influence of deposition temperature on the properties of SiOCH films. It is found that the deposition rate decreases more than 67% as the temperature increases from 200 to 400 ^{0}C, and follows a first exponential decay function with the temperature (^{0}C), which has apparent activation energy of -0.157 eV. The SiOCH films prepared at lower temperature show lower dielectric constant and refractive index, but the mechanical properties become poorer because the hardness and Young's modulus decrease largely with the deposition temperature. FTIR spectra reveal that more –CH and –CH_3 groups are introduced into the SiO_2 network of the films at lower deposition temperature. The –CH and –CH_3 groups and cage structure of Si–O bonds in the films are thought to be responsible for lowering the dielectric constant, refractive index, hardness and Young's modulus.

The as-deposited films are thermally stable at as high temperature as 500^0C, which exceeds the highest temperature (400–450^0C) encountered during typical interconnect processing steps.

The effect of oxygen gas flow rate on the properties of SiOCH films is studied in the second part of this thesis. FTIR spectra reveal that the Si-CH_3 content decreases as the oxygen gas flow increases. The lowest dielectric constant and refractive index can be obtained with O_2/3MS flow ratio of about 100:600 sccm, but hardness and Young's modulus also become worst at this gas flow rate region. As the oxygen gas flow rate increases, the deposition rate and surface roughness of the films increase, and the films become more hydrophilic due to increase of polar component of the surface energy increase.

In the last part of this project, the impact of RF power on the properties of SiOCH films is evaluated. Increments of the deposition rate, the refractive index, dielectric constant, hardness and Young's modulus, are observed at the higher RF plasma power. These effects are attributed to enhancement of precursors' decomposition and ionic bombardment, which cause the change in mass density and bond structure in the film. Although the Si-CH_3 content in the film shows no obvious variation with the RF power, T group ($O_3Si(CH_3)$) in the films is found to increase linearly as the RF power increases, which is thought to result in higher hardness and Young's Modulus. It is also found that the mechanical properties become much better with limited sacrificing of the electrical constant and refractive index at higher RF power.

Table of Contents

List of Figures

List of Tables

Chapter 1

Introduction

1.1 Background and Motivation

1.1.1 Problems Caused by Device Scaling on Interconnects

Integrated circuit (IC) density, performance, and cost per function have undergone continued improvements throughout the past forty years. Such advance was benefited from the following three generic strategies: 1) scaling down minimum feature size, 2) increasing die size, and 3) enhancing packing efficiency (defined as the number of transistors or length of interconnect per minimum feature square of silicon area). Scaling of transistor is the most widely used approach to simultaneously improve transistor performance and density [(1)]. The requirement of higher speed chips with more functions and memory bits dictates the need for smaller geometry. The downward scaling of dimensions on silicon-based integrated circuits can increase circuit performance (mainly by increasing circuit speed) and the functional complexity of the circuit. The increase of circuit speed was primarily due to reduction of transistor's intrinsic switching gate time, which results in shorter switching time. Usually, the scale factor S for downward scaling of device is typically $\sqrt{2}$ in device dimension for each IC generation, whereas the device density nearly double.

However, as the device performance and density increase, interconnect performance degrades with scaling. Such deterioration was caused by relatively larger average interconnect length (measured in gate pitches), larger die size and higher packing density for successive generations. Scaling of interconnect has resulted in an

increase in the number of wiring levels and a reduction in the wiring pitch (sum of the metal line width and the spacing between the metal lines) to increase the wire density. Due to reduced wire spacing and metal cross sections, both resistance (R) of the metal-interconnect and capacitance (C) of the intra (line to line) and inter (level to level) rise dramatically. As device dimensions shrink to less than 0.25 um, the interconnect RC delay dominates the total signal propagation and largely determines the chip performance instead of the intrinsic gate delay. Furthermore, due to RC coupling, crosstalk noise and power dissipation become significant [2-4].

1.1.1.1 RC Delay

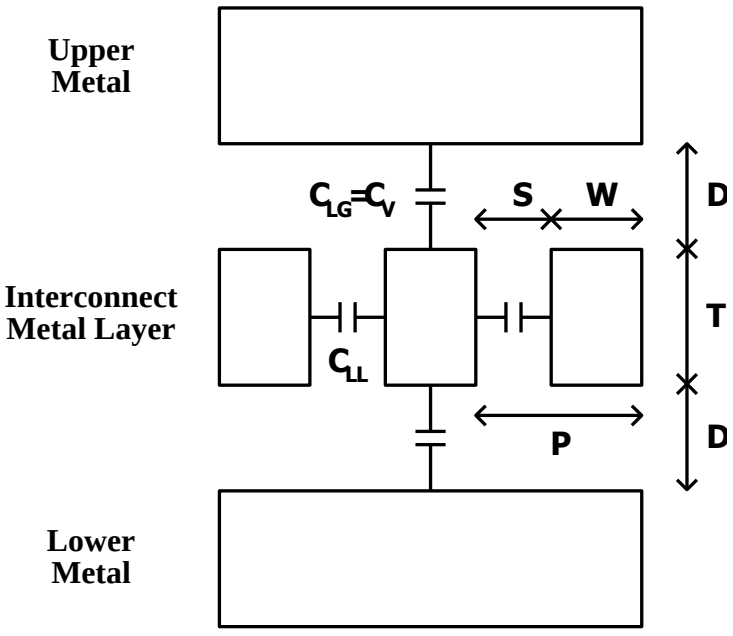

Fig. 1.1 Schematic diagram of an interconnect system cross-section with parasitic capacitance

A simple schematic diagram of a typical multilevel interconnect system, which is similar to the one used in Refs. (4) and (5), is shown in Figure 1.1. T is the metal thickness, D is the dielectric thickness between different metal layer, W is the metal width, S is the space between metals, P is the metal pitch (with P = W + S), C_{LL} is the lateral or horizontal line-to-line capacitance, C_v is the vertical layer-to-layer capacitance, and C_{LG} is the line-to-ground capacitance (with $C_{LG}=C_v$). If the pitch P and the metal thickness T are used as basic parameters, then one can set W = αP and D = βT, where α and β are constant for the given geometry.

The resistance R of a metal line with length of L and resistivity of ρ can be given by:

$$R = \rho L / WT = \rho L / \alpha PT \quad \text{----------} \quad (1.1)$$

For simple first-order model, the dielectric is assumed to have an isotropic relative dielectric constant k. The edge contributions from the metal lines and coupling of the metal lines sidewalls to the ground planes are neglected. With these assumptions, the total capacitance C of a metal line relative to its surroundings, and the RC time delay constant can be expressed as following:

$$\begin{aligned} C &= 2\left(C_{LL} + C_V\right) = 2k\varepsilon_0 L\left(\frac{T}{(1-\alpha)P} + \frac{\alpha P}{\beta T}\right) \\ &= 2k\varepsilon_0 L\left(\frac{\alpha\gamma}{(1-\alpha)} + \frac{1}{\beta\gamma}\right) \end{aligned} \quad \text{----------} \quad (1.2)$$

$$\begin{aligned} RC &= 2\rho k\varepsilon_0\left(\frac{L^2}{P^2}\right)\left(\frac{1}{\alpha(1-\alpha)} + \frac{P^2}{\beta T^2}\right) \\ &= 2\rho k\varepsilon_0\left(\frac{L^2}{P^2}\right)\left(\frac{1}{\alpha(1-\alpha)} + \frac{1}{\alpha^2\beta\gamma^2}\right) \end{aligned} \quad \text{----------} \quad (1.3)$$

where ε_0 is the permittivity of free space, γ is the aspect ratio of the metal lines, and is defined as the ratio of line thickness to line width, γ = T/W, or equivalently γ=T/(α P).

The right hand side of equation (1.3) can be interpreted naturally as following: the factors $\rho k \varepsilon_0$ and $2\left(\frac{L^2}{P^2}\right)\left(\frac{1}{\alpha(1-\alpha)}+\frac{1}{\alpha^2\beta\gamma^2}\right)$ represent the materials and architecture contributions to the interconnect time delay, respectively. It should be noted that the term $\frac{1}{\alpha(1-\alpha)}$ in equation (1.4) signifies the intralayer ("horizontal") and the term $\frac{1}{\alpha^2\beta\gamma^2}$ designates interlayer ("vertical") contribution to the total RC time delay. The similar natural interpretation can also be made for the right hand side of equation (1.2)

It can be clearly seen from equation (1.3) that the RC delay increases quadratically with the decrease of feature size (decreasing pitch P) if other parameters are fixed. Equations (1.2) and (1.3) also suggest that for γ >> 1 the intralayer ("horizontal") capacitance C_{LL} is more important to the total capacitance and RC delay than the interlayer interlayer ("vertical") Cv, whereas the opposite is true for γ << 1.

When explaining equations (1.1) to (1.3), it should be noted that even as devices and their interconnect dimensions keep shrinking, the metal line length L tend to scale less strongly than the metal pitch [(4)], and some rather long lines will still exist

[6], so the ratio L/P does increase instead of staying constant. At the same time, the aspect ratio γ tends to increase in order to keep resistance R as low as possible for minimizing electrical power dissipation. Therefore, as device dimensions decrease, when applied equations (1.2) and (1.3) to a given set of interconnect materials with fixed ρ and k, these geometrical constraints result in two conclusions: (1) the RC delay will increase; (2) the intralayer capacitance C_{LL} will dominate the overall capacitance, and increase crosstalk and power dissipation which will be discussed in later sections.

For simplicity, the effects of fringing fields and finite electrode thickness have been ignored in the calculation of capacitance in equations of (1.2) and (1.3). Jeng et al. [7] have presented more rigorous calculations of interconnect RC time constant and intrinsic gate delay as a function of IC feature size. Figure 1.2 and Figure 1.3 [7] depict the results of their study. As shown in Figure 1.2, the gate delay is important only for device features larger than 1 μm. However, as the feature size shrinks below 0.5 μm, the performance of interconnect degrades dramatically due to the increase of resistance and capacitance. Figure 1.3 shows the influence of the feature size on the line-to-line interconnect capacitance and line-to-ground interconnect capacitance. A simple multilevel interconnect wiring scheme and the definition of these interconnect capacitance are also given in the inset of the figure. Typical inverter circuit was modeled with Al metal, SiO_2 as the dielectric, a wire length of 5000 μm and a metal thickness of 0.7 μm. It can be seen that the line-to-line capacitance becomes more and more important as the feature decrease into submicron region, and it contributes almost 90% of the total capacitance at sub-0.25 μm feature size. Therefore, reducing

the line-to-line capacitance is one of the most critical issues for sub-0.25 μm IC devices.

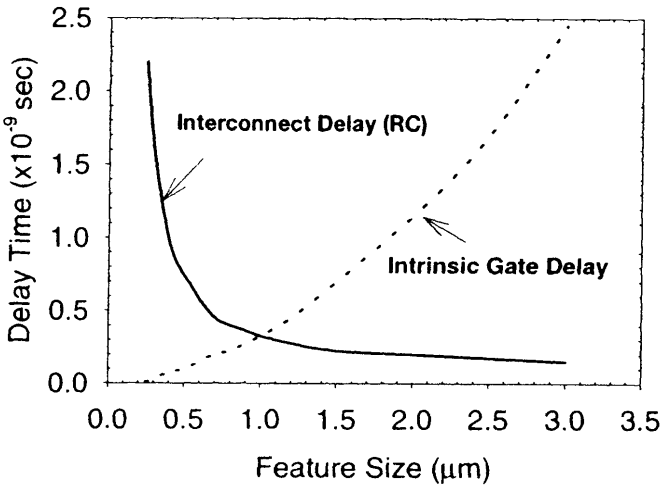

Fig. 1.2 Interconnect RC delay and intrinsic gate delay as a function of the feature size [7]

.

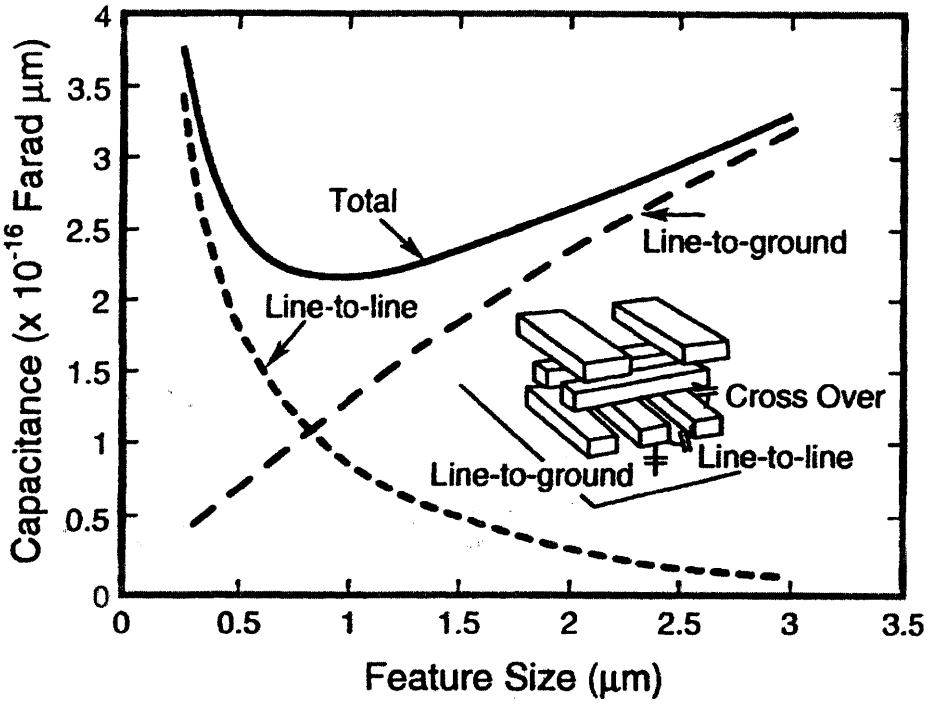

Fig. 1.3 Interconnect capacitance vs. feature size [7]

1.1.1.2 Cross-Talk

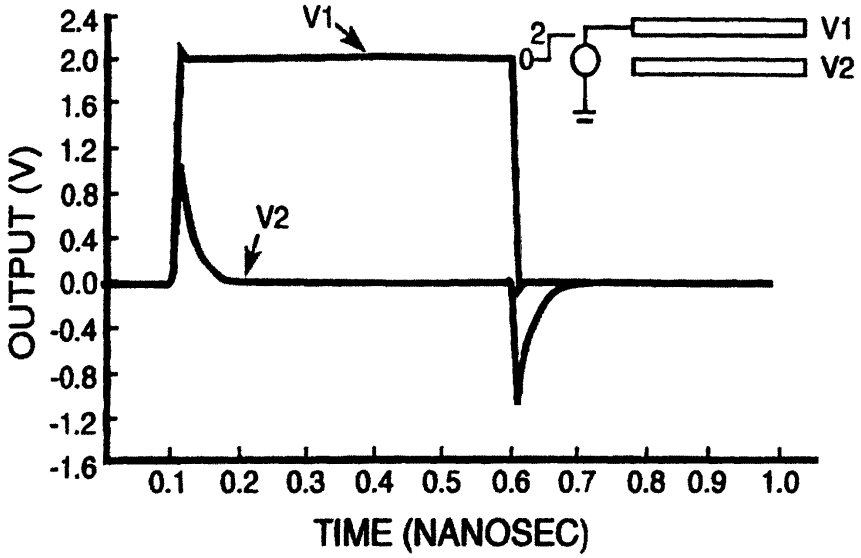

Fig. 1.4 Cross-talk between two interconnects [9]

Cross-talk refers to the disturbance generated on a metal line due to a rapid transition in an adjacent line and is a major issue for high-performance circuits. When the electrical pulses propagate through the interconnect wires very rapidly, e.g. more than 100 MHz, the electromagnetic coupling can impose significant undesirable voltages on the neighboring unpowered lines [8].Thomas et al. have investigated this phenomenon with results presented in Figure 1.4 [9]. In Figure 1.4, two interconnects with a square cross-section of 1 μm^2 are separated by 1 μm with a ground plane 2 μm below it. Each interconnect is 1 mm in length. One of them sees a rise time pulse of about 500 MHz while the other is attached to ground. A dense array of underlying wiring can approximate as a ground plane. During the rise and fall of the waveform on the grounded line, a substantial unwanted voltage (about 50% of V_1) will be generated on the undriven line. If the spacing between the wires decreases, this

situation will become worse. At 0.5 μm spacing, this cross-talk would rise to about 70% of the total voltage applied to the driven line. If lines become smaller and possess more resistance, even larger RC delay is associated with the decay of the unwanted signal. Cross-talk therefore poses a problem for advanced IC as the device feature size scaling down to submicron.

Takayasu Sakurai also gave a model shown in Figure 1.5 to demonstrate that cross-talk between adjacent RC lines can cause unintentional switching [(10)]. According to VLSI design theory [(11)], a point-to-point single-layer interconnection driven by a transistor and connected to the next gate, can be treated as a distributed RC line driven by a voltage source V_{s1} (V_{s2}) with an internal resistor of R_{t1} (R_{t2}) and loaded with capacitor of C_{t1} (C_{t2}) as shown in Fig 1.5. R signifies the total resistance, C designates the total capacitance of the line, and $V_1(l, t)$ (or $V_2(l, t)$) stands for load voltage risen from the source.

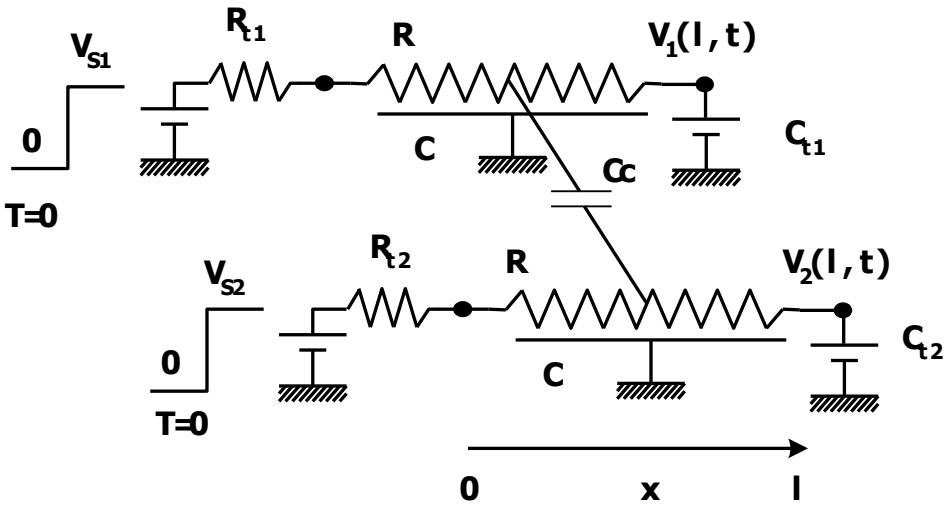

Fig. 1.5 Model for capacitively coupled RC lines [(10)]

The two capacitively coupled distributed RC lines shown in Figure 1.5 can be described by the following basic differential equations [(10)]:

$$\begin{cases} \dfrac{1}{r_1}\dfrac{\partial^2 V_1}{\partial x^2} = (c_1 + c_c)\dfrac{\partial V_1}{\partial t} - c_c \dfrac{\partial V_2}{\partial t} \\ \dfrac{1}{r_2}\dfrac{\partial^2 V_2}{\partial x^2} = (c_2 + c_c)\dfrac{\partial V_2}{\partial t} - c_c \dfrac{\partial V_1}{\partial t} \end{cases} \text{----------(1.4)}$$

where r_1 (r_2) and c_1 (c_2) are resistance and capacitance to the ground per unit length of line 1 (2), respectively. c_c is the coupling capacitance between the two *RC* lines per unit length.

If $V_{s1} \neq 0$ but $V_{s2} \equiv 0$, which means there is signal in line 1, but no signal in line 2, then the peak value of $V_2(l, t)$, V_p, is a noise height induced by the capacitive crosstalk from line 1. If V_p is higher than a logic threshold voltage of any gates in the next stage, a malfunction may occur. From equations (1.4), V_p can be obtained by differentiating [(12)]:

$$\frac{V_p}{V_{s1}} = 1.01\frac{R_T + C_T + 1}{R_T + C_T + \pi/4}\left(\frac{1}{1+2\eta}\right)^{1/2\eta}\left(\frac{\eta}{1+2\eta}\right) \text{----------(1.5)}$$

For simplicity, it is assumed that $r_1=r_2=r$, $c_1=c_2=c$, and $R_{t1}=R_{t2}$ in calculation. *R*, *C*, and *Cc* are *rl*, *cl*, and $c_c l$, respectively, where *l* is the length of the lines. In equation (1.5), $R_T = R_{t1}/R = R_{t2}/R$, $C_T = C_{t1}/C = C_{t2}/C$, and $\eta = C_C/C$.

In the case where the interconnect RC delay dominates the total delay, $C_T = 0$ can be assumed. When R_{t1} is zero and R_{t2} is finite, V_p can be expressed as [(10)]:

$$\frac{V_p}{V_{s1}} \approx \frac{\frac{1}{2} + R_{T2}}{1 + R_{T2}}\left(\frac{\frac{C_c}{C}}{1 + 2\times\frac{C_c}{C}}\right) \text{----------(1.6)}$$

Where $R_{T2}=R_{t2}/R$. Finite R_{t2} means that line 2 is not pinned down so firmly. This case is very important because the value V_p can becomes very high, thus resulting in malfunction of the circuit system.

Formula 1.6 is plotted graphically in Figure 1.6 and can be used to estimate crosstalk noise. As shown in Figure 1.6, the crosstalk noise increases significantly as the coupling capacitance Cc, the capacitance of line 1 to line 2. Figure 1.3 reveals that the capacitance between lines will dominate the overall capacitance as the device shrink into deep sub-micron region, thus the system will show worse crosstalk characteristics. While geometrical improvements in the design can help in reducing the crosstalk noise, it is clear that a lower dielectric constant material can significantly reduce the crosstalk problem.

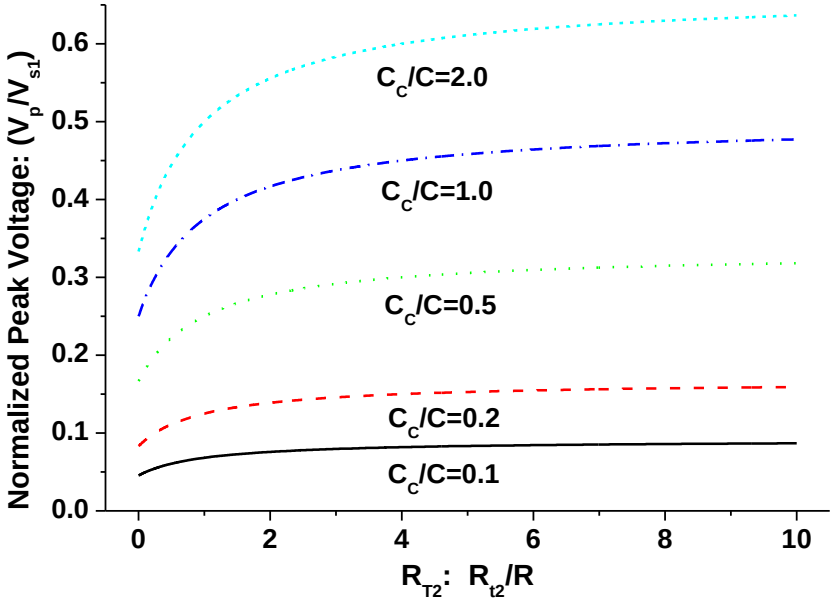

Fig. 1.6 Peak crosstalk voltage

1.1.1.3 Power Dissipation

In the deep sub-micron generation, power dissipation becomes significant due to increased wiring capacitance, especially interline capacitance between the metal lines on the same level. Static and dynamic power dissipations compose the overall on-chip power dissipation, and their contributions are different for bipolar and CMOS (complementary metal-oxide semiconductor) circuit. Generally, the static power factor dominates the overall power dissipation for ECL (emitter-coupled logic), the most modern bipolar circuit style. On the other hand, for CMOS circuit, which is most popular and competitive circuit style in the last decade, the majority of the power dissipation is the dynamic charging and discharging of the capacitances [13]. Figure 1.7 shows a simple CMOS inverter, where V_{dd} is the source voltage and C_L is the load capacitance. Load capacitance C_L is composed of the wiring capacitance C_W and the input capacitance (C_{in}) of the fan-out gates.

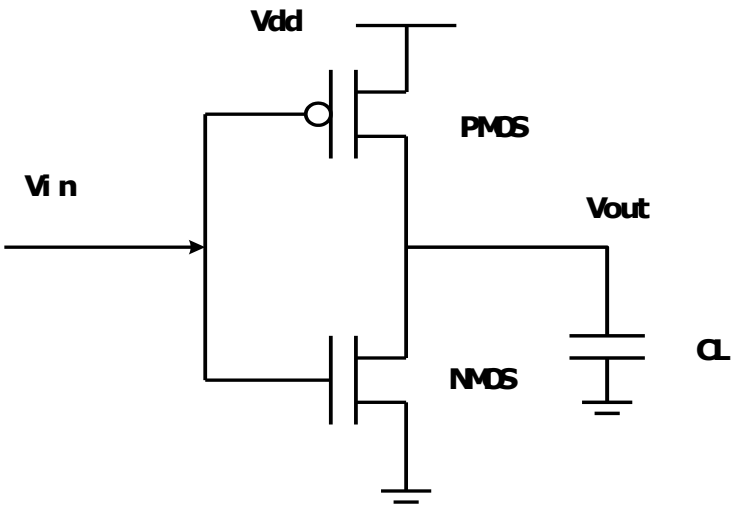

Fig. 1.7 Simple CMOS inverter.

If the CMOS inverter is switched on and off for f times per second, the total power consumption can be expressed as following [(13)]:

$$P_{total} = P_{dyn} + P_{dp} + P_{stat} = C_L V_{dd}^2 f + V_{dd} I_{peak} \left(\frac{t_r + t_f}{2} \right) f + V_{dd} I_{leak} \text{ ----------(1.7)}$$

P_{dyn} is the dynamic consumption due to the dynamic charging and discharging of the load capacitance; P_{dp} denotes the power consumption due to direct-path currents because the signal rise time (t_r) and fall time (t_f) are not zero in reality; P_{dp} is also a kind of dynamic power consumption for it occurs during switching. P_{stat} represents the static power dissipation due to leakage current I_{leak}. In generally, P_{dp} and P_{dp} are substantially smaller than P_{dyn} and can be ignored in first-order calculations.

The above equation holds for more complex gates and other logic elements. Since the interconnect capacitance is the dominate component of load capacitance at small feature sizes (see Figure 1.3), reducing the interconnect capacitance can result in lower power consumption. Therefore, if low k dielectric is introduced into the interconnect system, more devices can be packed in the same area without an increase in the power dissipation.

1.1.2 Low-k materials are needed to Solve the Interconnect Problems

As discussed above, the interconnect problems of RC delay, cross-talk, and power dissipation are substantially caused by the increase of interconnect resistance and capacitance. Any approach to reduce of the resistance and capacitance is a prospective solution to these problems. From equations (1.2) and (1.3), it can be seen that the interconnect resistance and capacitance are composed of two factors:

architecture contribution and material contribution, which suggest two general ways to solve the interconnect problems: design solution and material solution.

1.1.2.1 Design Solution

Before any new process technology changes radically in the industry, it is valuable to extend current technologies and fully realize their potential through the development of circuit design solutions, which includes reduction of interconnect length, hierarchical scaling, and interconnect-centered design.

Equations (1.2) and (1.3) show that RC delay and capacitance will increase with the interconnect length L quadratically and linearly, respectivety, if other parameters are fixed. In order to minimize the RC delay and capacitance, the interconnect length L should be reduce as much as possible. Repeaters and cascaded drivers [(14, 15)] are well-known examples of methods to reduce the interconnect length. Repeaters are minimum-size inverters that can reduce the overall RC delay by breaking a long (global) interconnects into smaller segment. The number of repeaters for partition of a long metal line can easily be optimized to minimize RC delay. A cascaded driver consists of a series of increasingly larger inverters so as to boost the drive current. Since delay time is inversely proportional to the drive current, minimum RC delay can be yielded by optimization of the number of drivers and their size ratio. However, repeater and cascaded driver need extra space, which may not be available in a closely packed layout based only on logic functionality. Another efficient approach to reduce the wire length is so called three-dimensional (3-D) integration of ICs, which is developed in semiconductor process technology for the fabrication of a single IC with multiple device-interconnect layers or wafers stacked

on each other [16]. 3-D integration can narrow the wire-length with higher number of local wires and fewer global wires than 2-D integration, thus resulting in substantial reduction of the longest global interconnects in a distribution by as much as 75% [17]. However, the power dissipation and thermal management are serious concerns for 3-D integration.

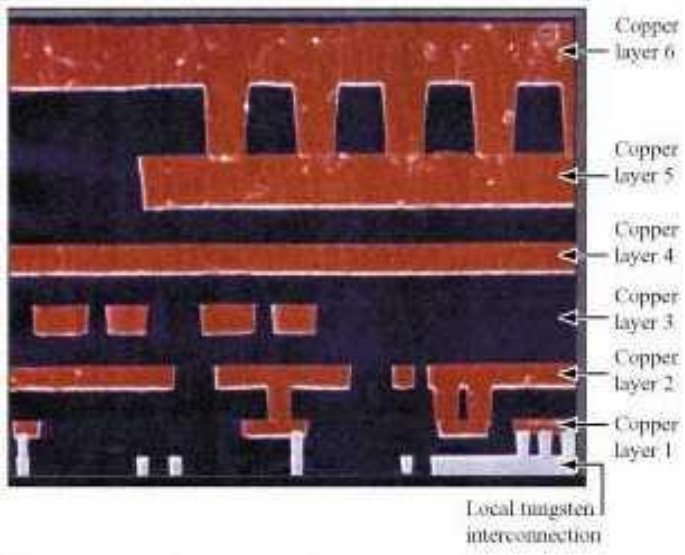

Fig. 1.8 Cross-sectional SEM micrograph of typical CMOS 7S interconnects [19]

In addition to these design schemes, a hierarchical wiring system is proposed to further improve the interconnect performance in deep sub-micron devices. In hierarchical interconnect scheme, the metal pitch and thickness progressively increase from the lower to the upper levels and the wire length changes from local to global accordingly [18]. At the lower metal level, narrow thin short wires dominate the routing, so that the RC delay is not an issue and the packing density can be maximized. At the upper levels, on the other hand, the routing is composed of long thick wires to reduces RC delay and improve the circuit system performance. CMOS 7S is an example of a hierarchical wiring system in which successive wire levels at

increasing thickness and width enable long wire run with low RC delay. Figure 1.8 [19] shows the cross-sectional scanning electron microscope (SEM) photograph of typical CMOS 7S interconnections. Hierarchy should be designed to minimize the number of metal levels, thus involves trade-offs between density, performance, and manufacturability.

Interconnect-centered design is different from the conventional logic function-centered designed with consideration of interconnect effects throughout the whole design flow [20]. Traditionally, IC design has been centered around logic functionality, which generally begins at behavioral-level design, followed by register-level design, and finally verified by simulation. Few, if any, iterations are needed, and interconnect effects are generally ignored. However, as the device feature size shrink beyond 0.25 μm, the physical parameters and constraints from interconnects are too important to be ignored, and the interaction between logic gates and distributed interconnections becomes an integral part of the circuit design process. In interconnect-centered design, interconnect effects are integrated with the whole design process, and interconnect layout is optimized to achieved best performance of circuit, thus resulting in more complicated for the design.

1.1.2.2 Material Solution

While some new design schemes as discussed above will alleviate the interconnect crisis, the traditional Al/SiO_2 interconnect system must be replaced with higher conductivity metals and low-k dielectric materials in the future interconnection systems from a long term of view, so that this problems can be addressed more radically.

Apart from superconductors, very few metals possess lower resistivity than aluminium. The electrical resistivities of some good conductive metals at 68 ^{0}F (20 ^{0}C) are given as following: 1.59 μΩ-cm for extremely pure silver (Ag), 1.67 μΩ-cm for pure copper (Cu), 2.35 μΩ-cm for pure gold (Au), 2.6548 μΩ-cm for pure aluminum (Al) [(21)]. It is apparent that the only few possible options to replace Al are Au, Cu, and Ag. But, the only practical option really is Cu for two reasons. The first reason is costs, manufacturability, and device reliability favor Cu. The second reason is that the difference of the electrical resistivities between Cu and Ag, which has the smallest electrical resistivity, is quite small. Copper is clearly the most suitable alternative conductive material, and some manufacturers have already been using it as metal wires. In terms of improving conductivity, the additional gain in going from Al (ρ_{bulk}=2.6548 μΩ-cm) to Cu (ρ_{bulk}=1.67 μΩ-cm) would be about 37%, so about 37% lower RC delay can be obtained if aluminium wires are replaced by copper wires with the same cross section area. Moreover, copper interconnect made by a dual-damascene process provides additional advantage of both cost and reliability over existing aluminium wiring processes [(22)].

Copper helps to reduce the RC delay, but it is obviously not enough to address interconnect issues by only changes in wiring materials. As mentioned above, line-to-line capacitance dominates interlevel capacitance, and it is one of the most critical issues for sub-0.25 μm IC devices. New materials with low dielectric constant are needed to replace SiO_2 in order to keep device performance. As compared to substitution of aluminium with copper, using low-k material as interlayer dielectrics has other benefits besides reduction of RC delay, such as the reduction of cross-talk

and power dissipation. Therefore, it becomes increasingly important to implement interlayer dielectric (ILD) using low-k dielectrics.

1.1.3 Requirements of Low-k Material Property

Table 1.1: Property requirements of low-k materials as inter-layer Dielectrics

Electrical	Chemical	Mechanical	Thermal
High electric-field strength	Chemical Resistance	Thickness uniformity	High thermal stability
Low dissipation	Low moisture absorption	Good adhesion	Low thermal shrinkage
Low leakage current	Low solubility In H_2O	High hardness	High thermal conductivity
Low charge trapping	Low gas Permeability	High Tensile modulus	Low coefficient of thermal expansion
High reliability	Etch selectivity	Crack resistance	
	High purity		
K Anisotropy	No metal corrosion	Low shrinkage	Low thermal weight loss
	Long storage life		
	Environmentally safe	Low stress	

Since the dielectric acts as both the insulating and the isolating layer between the wires, there are many requirements of the dielectric in addition to just possessing low dielectric constant as discussed in the previous section. Low dielectric constant materials must be chemically and physically compatible with the other materials that constitute the integrated circuits, as well as with the process and package used in manufacturing. Under the sponsorship of SEMATECH, the US semiconductor industry has devised a list of the desired properties of low-k materials as interlayer

dielectric materials, as presented in Table 1.1 [23]. These requirements will need extensive integration and reliability test in addition to the standard film characterization techniques.

1.1.4 Present status and future trends of low k Materials

Silicon dioxide (SiO_2) has been used as an interlayer dielectric (ILD) film for a long time since the invention of integrated circuits. Interconnect delay begins to dominate overall device delay at deep submicron region, making low-k transitions so attractive for advanced interconnect system. The range of low k materials is quite broad, but the choice of the next generation dielectric is an open question. The reason is that low k interlayer dielectric materials must meet lots of electrical, chemical, mechanical and thermal properties (as shown in Table 1.1), and each low k dielectric has it's own advantages and disadvantages related to integration. Typical low k materials are listed in Table 1.2 [24 -28].

Low-k materials can be categorized by their dielectric constant. The k value of the interlayer dielectric must decrease as the technology node goes down. Fluorinated silicon oxide (FSG, k=3.6) act as the 1st generation low dielectric constant ILD material at the 180 nm technology node [29]. Incorporation of more fluorine atoms into FSG can further decrease the dielectric constant, but FSG's k value is typically limited to about 3.6 because of chemical instability when fluorine loadings exceed 5 atomic % (at%). FSG is not incompatible with metal liner materials especially for its moisture absorption. Therefore, the use of fluorine-containing dielectric materials is limited.

Table 1.2: Leading Candidates for low-k materials

Material	Dielectric constant	Deposition method
Low-k materials		
SiO_2 (thermal TEOS)	3.9~4.1	CVD
FSG or SiOF (fluorinated silica)	3.4~4.1	CVD
Polyimides	3.0~3.6	Spin-on
Spin-on glasses	2.7~3.1	Spin-on
DLC (diamond-like carbon)	2.8~3.0	CVD
HSQ (hydrogen silsesquioxane)	2.8~3.0	Spin-on
MSQ (methyl silsesquioxane)	2.8~3.0	Spin-on
SiOCH (OSG) (carbon doped silica)	2.6~3.0	CVD
Poly (arylene ethers)	2.6~2.9	Spin-on
Poly (arylenes)	2.6~2.8	Spin-on
Parylene N	2.6~2.8	CVD
BCB (benzocyclobutene)	~2.6	Spin-on
SiLK (Aromatic Hydrocarbon)	~2.6	Spin-on
Parylenes (& polynaphthalene families)	2.2~2.6	CVD
SSQ (Polysilesquioxanes)	2.5~3.5	Spin-on
a-CF (fluorinated amorphous carbon)	2.0~2.5	CVD
Ultralow k		
Teflon Microemulsion	1.9~2.1	Spin-on
PTFE (Teflonn-AF) (polytetrafluoroethylene)	1.9~2.1	Spin-on
Porous dieletrics		
Polyimide nanofoams	~2.2	Spin-on
Mesoporous silica	1.9~2.2	Spin-on
Silica xerogels	1.2~2.2	Spin-on
Silica aerogels	1.1~1.2	Spin-on
Air gap or Air bridge	< 2.0	

A lot of low k materials (k<3) were introduced at the 130 nm node, but there seems to be little agreement on which low-k dielectric is the best. The problems rose from integration and reliability, such as thermally and mechanically induced cracking

or adhesion loss, poor mechanical strength, moisture absorption, and low dielectric breakdown field.

Much lower k dielectric materials (k<2.5) are in development stage. In order to obtain materials with k value less than 2.5, pores are introduced into the dielectric. The ideal ultra-low-k material (k<2.5) should have a closed pore structure with uniform distribution, and it must be able to withstand polishing, etching and heat treatments. The poor mechanical property is a typical challenge for porous low k. Introducing pores in the films results in the reduction of mechanical strength, causing CMP adhesion failure. Low stiffness properties of porous low-k films are a key factor limiting their introduction into ultra-large scale integrated (ULSI) technology. In order for low k dielectrics to survive technological steps, a compromise must be reached between low dielectric constant and sufficient mechanical strength.

Table 1.3 Classification of Low k Materials

Dielectric Materials	Dielectric Constant	Deposition Method
Oxide Derivatives	**Range: 1.2 ~ 3.9**	
F-doped oxides	K = 3.3 ~ 3.9	CVD
C-doped oxides (e.g. SiOC:H, MSQ)	K = 2.8 ~ 3.5	CVD / (Spin-on)
H-doped oxides (e.g. HSQ)	K = 2.5 ~ 3.3	Spin-on
Porous oxides (Xerogels / Aerogels)	K = 1.2 ~ 2.2	Spin-on
Organics	**Range: 1.2 ~ 4.0**	
Polyimides	K = 3.0 ~ 4.0	Spin-on
Aromatic polymers	K = 2.6 ~ 3.2	Spin-on
Parylene / Parylene-F	K = 2.7 / 2.3	Spin-on
F-doped amorphous carbon	K = 2.3 ~ 2.8	CVD
Teflon / PTFE	K = 1.9 ~ 2.1	Spin-on

Although at least a few dozen of low-k candidates have already under investigation, there seems to be little agreement on which low-k dielectric is the best. Most materials [30-66], as grouped in Table 1.3, can be either oxide derivatives or organics, and can be deposited by either CVD or spin-on techniques. The establishment of a leadership position for the low-k materials depends on numerous fabrication and performance tradeoffs. For example, the typical dilemma is that materials with lower dielectric constant show poorer thermal-mechanical properties. The choice of deposition process for low-k materials is another conflict usually between spin-on and chemical vapor deposition (CVD).

There are two main deposition methods for low-k materials: spin-on and chemical vapor deposition (CVD). When it goes down to ultra low-k or porous dielectrics or air gap, there are other different methods for the preparation of low-k materials besides deposition method.

The contest between spin-on and CVD films, mostly SiLK heralded by IBM and CVD carbon doped silicon dioxide alternatives, is mainly staged by the extendibility of new spin-on dielectric (SOD) and process integration schemes for multiple technology nodes, on one hand, versus the desire to extend CVD tool sets for one more generations. The CVD versus spin-on battle is further affected by business approach. For example, in many cases, CVD suppliers can provide an integrated solution to the customer, the starting point from which the device manufacture's process is developed. The foundries need to rely on vendors for low-k solutions that have been well characterized and can be easily introduced into production.

For more than 30 years since the invention of integrated circuits, silicon dioxide (SiO_2) has been used as an interlayer dielectric (ILD) film because of its excellent electrical, thermal, mechanical and chemical properties. An ideal low-k material should offer low-k with other properties that closely resemble those of traditional thermal silicon dioxide as much as possible. Silicon based low k materials are much more compatible to existing device process flows and could meet less integration issues than other kinds of low k materials. For example, Si-based low k materials obviously have better adhesion to silicon, silicon oxides, nitride, Al and Cu metallization. Also, Si-based low k materials can be easily etched by the familiar F-based etching chemistry. Probably the most important advantage is the greater hardness of Si-based materials with regard to integration issue of chemical-mechanical polish (CMP) process.

The logical method to get Si-based low k material is to modify the structure and composition of silicon dioxide. Modification of SiO_2 can reduce the k value with more good properties of silicon dioxide than other low-k materials like polymer. Doping SiO_2 with fluorine atom in conventional CVD processes and equipment is one of the most straightforward ways to reduce the dielectric constant of IMD films. F-doped oxides (SiOF or FSG, fluorine doped silica, k-3.6) with many good properties closed to that of conventional SiO_2, is the early winner of first generation low dielectric constant ILD material at the 180 nm technology node [(29)]. The logical step for transition to second generation low k materials is to further modify the silicon dioxide. Incorporation of carbon atom into SiO_2 network [(35-38)] using CVD technique can get SiO_2-like low-k materials with lower k value than SiOF. A group of such dielectrics, named as organosilicate glass (OSG) or carbon doped silicon dioxide

(SiOCH), was deposited by PECVD process using organosilicon gases as precursors [36-38]. Therefore, this project will focus on study of carbon-doped dioxide (SiOCH) deposited by PECVD technique. While these materials are denoted by many names, such as SiOCH, SiCOH, SiOC, silicon-oxicarbides, carbon-doped oxide (CDO), organosilicate glass (OSG), carbon doped silicon dioxide, the term SiOCH will be used throughout this thesis to refer to the entire group of the discussed materials.

1.2 Objectives

The main objective of this work is to study SiOCH for low-k dielectric application in multilevel interconnect. It will focus on the development and evaluation of plasma enhanced chemical vapor deposition processes for SiOCH with dielectric constant less than 3.0. The effects of various tunable process parameters on the properties of SiOCH films are investigated systematically. The thermal stability of SiOCH films will be also discussed

1.3 Major Contributions

The major contributions achieved in this study include the deposition and characterization of SiOCH films, and the investigation of their properties after thermal treatment. They can be summarized as following:

1. **Influence of deposition plasma power on the properties of SiOCH films**

It is found that higher RF plasma power can increase the deposition rate, the refractive index, dielectric constant, hardness and Young's modulus, because its

enhance effects of decomposition of precursors and ionic bombardment would cause the change of film density and bond structure in the film.

2. Effects of gas flow rate on the properties of SiOCH films

The ratio of reactant gas flow rate affects significantly the deposition rate, dielectric constant and refractive index by tuning the carbon content in the films. Lowest dielectric constant can be obtained at O_2/3MS ratio of about 1/6. No much influence on hardness and Young's modulus is found at higher gas flow rate.

3. Relationship of deposition temperature and the properties of SiOCH films

The deposition rate, hardness and Young's modulus are found to increase markedly when deposition temperature increases, whereas the variation of the dielectric constant and refractive index is very small.

4. Thermal stability of SiOCH film

Thermal stability of SiOCH film has been evaluated by annealing it at N_2 atmosphere for about 30 minutes at different temperatures. The film is very stable at below 600 ^{0}C. Its properties, such as thickness, FTIR, dielectric constant and refractive index would degrade obviously when the annealing temperature rises up to 700 ^{0}C. The thermal stability of SiOCH film is also investigated at 450 ^{0}C in N_2 atmosphere for different annealing time.

1.4 Organization of the thesis

This thesis is composed of five chapters.

Chapter one introduces the background of low k materials, followed by the motivations, objectives and major contributions of this study.

Chapter two briefly presents the basic background of known mechanism of dielectric constant and methods to reduce the dielectric constant.

Chapter three describes the PECVD system used for SiOCH deposition, and discusses the relative characterization techniques and tools.

Chapter four presents the relationship between deposition temperature and mechanical, electric and optical properties of SiOCH films;

Chapter five discusses the effect of RF power and gas flow rate on the properties of SiOCH films.

Finally, the conclusions and recommendations for low k SiOCH films are given in Chapter six.

Chapter 2

Review of Dielectric Mechanism and Methods to Reduce the Dielectric Constant

2.1 Origin of Dielectric Constant

Dielectric materials are distinguished by having their specific electrical conductivity beyond $10^{-5}(\Omega cm)^{-1}$ due to lack of conduction carriers, especially free electrons. A dielectric material can react to an electric field because it contains charge carriers that can be displaced or polarized. Usually, the polarizing species approximates to a dipole, which is electrical charges of equal and opposite sign, e.g. ±Q separated by a distance R. This dumb-bell-like configuration can rotate, and in order to calculate the effects of this, the dipole moment is defined as $\vec{m} = Q\vec{R}$. The electric dipole moment $\vec{m}$ is a vector quantity, taken along the dipole from negative electrical charge to positive electrical charge as the vector quantity $\vec{R}$, which is sketched in Figure 2.1.

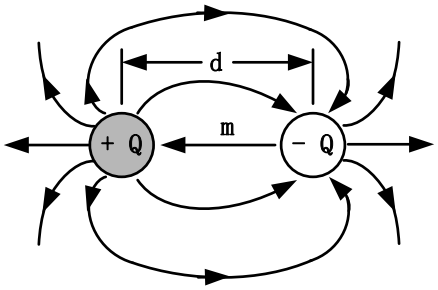

Fig. 2.1 Electric dipole of the moment $\vec{m} = Q\vec{R}$

The phenomenon of dielectric polarization was first recognized by M. Faraday. A dielectric material increases the storage capacity of a condenser by neutralizing charges at the electrode surfaces which otherwise would contribute to the external field. It may be visualized as the action of dipole chains which form under the influence of the applied and bind countercharges with their free ends on the metal surfaces (Figure 2.2).

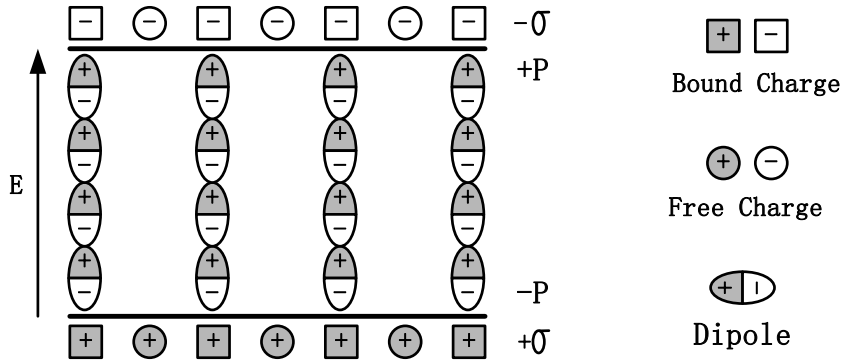

Fig. 2.2 Schematic representation of dielectric polarization

Clearly, the total charge on the metal surfaces consists of free charges and bound charges which come from dielectric polarization. Both the free charges and bound charges contribute to the whole true charge density, which is described by a vector $\vec{D}$, the electric flux density (or dielectric displacement). The bound charge density is called the polarization, and represented by a vector $\vec{P}$. The free charges density is given by $\varepsilon_0 \vec{E}$, where ε_0 is permittivity of free space, and $\vec{E}$ is a vector representing the electric field strength or field intensity. The ratio of bound charge density and free charge density is defined as the electric susceptibility χ, which is express as follow:

$$\chi = \frac{bound\ \ charge\ density}{free\ charge\ density} = \frac{P}{\varepsilon_0 E} \text{ ----------(2.1)}$$

Based on the Gauss theorem, the interrelations between the three field vectors, $\vec{D}$, $\vec{P}$ and $\vec{E}$, are as follows:

$$\vec{D} = \varepsilon_0 \vec{E} + \vec{P} \text{ ----------(2.2)}$$

Combining equations (2.1) and (2.2), the dielectric displacement can be written as:

$$\vec{D} = \varepsilon_0 \vec{E} + \varepsilon_0 \chi \vec{E} = \varepsilon_0 (1+\chi)\vec{E} = \varepsilon_0 \varepsilon_r \vec{E} \text{ ----------(2.3)}$$

where the relative permittivity or dielectric constant ε_r, is defined as $\varepsilon_r = (1+\chi)$. The relative permittivity or dielectric constant can also be represented by symbol k. Symbol ε_r is often adopted by the scientific communities contrast k used by microelectronics community. In this report, ε_r is used in scientific formulas, but k is used in discussion.

The polarization vector $\vec{P}$ corresponds in magnitude to the surface charge density bound at the electrodes by the polarized dielectric, and it points in the direction of the applied field. The polarization $\vec{P}$ is therefore identical with the electric dipole moment per unit volume of the dielectric material. This provides an entrance from the macroscopic view into the molecular world. Therefore, $\vec{P}$ can be thought as resulting from the additive action of N elementary dipole moments $\vec{m}$, and $\vec{P}$ equals to $N\vec{m}$. The average dipole moment is defined as $\vec{m} = \alpha \vec{E}'$. α is called polarizability which measures the electrical pliability of the particle. $\vec{E}'$ is the local electric field strength that acts on the particle. So there are two alternative expressions for the polarization:

$$\vec{P} = (\varepsilon_r - 1)\varepsilon_0 \vec{E} \equiv \chi \varepsilon_0 \vec{E} \text{ ----------(2.4)}$$

$$\vec{P} = N\alpha \vec{E}' \text{ ----------(2.5)}$$

The above two expressions link the macroscopically measured permittivity to three molecular parameters: the number N of contributing elementary particles per unit volume, the locally acting electric field $\vec{E}'$, and their polarizability α which will be discussed in next section).

2.2 Component of Polarization

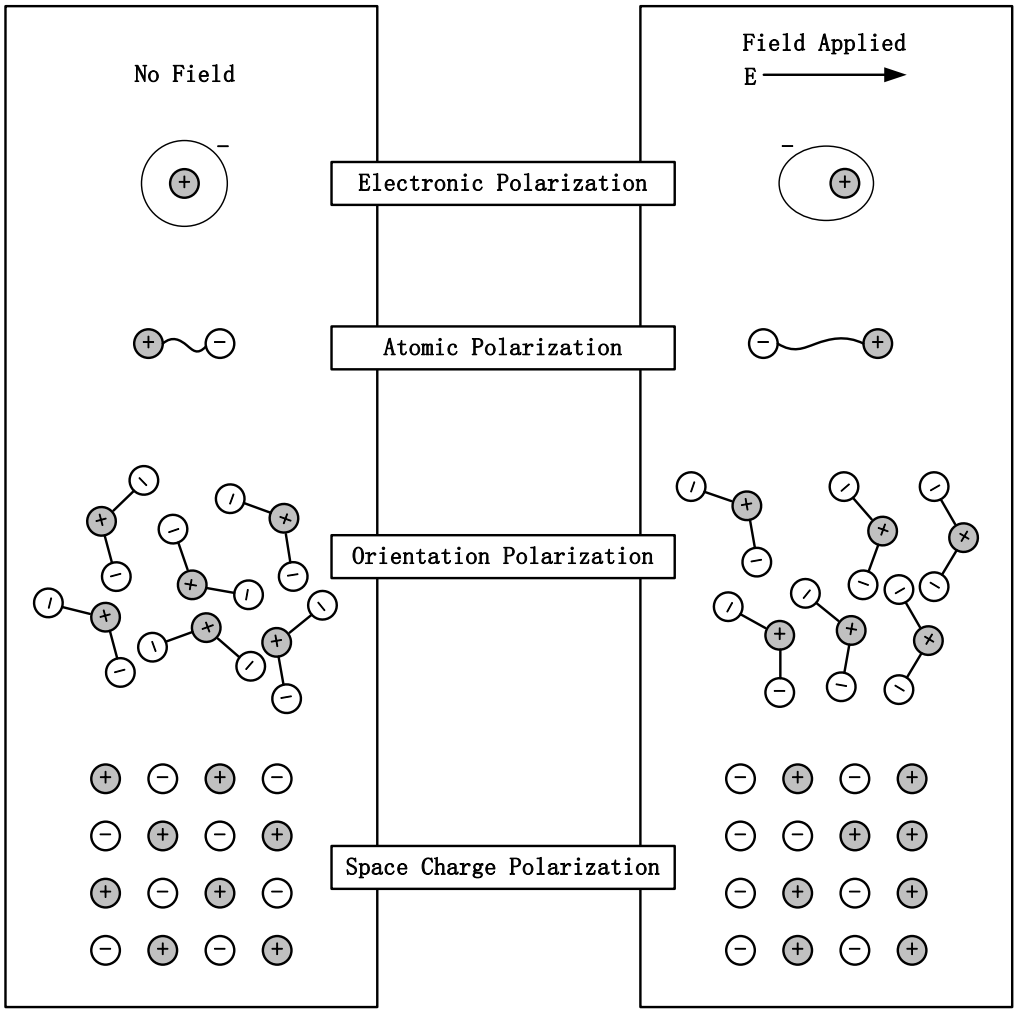

Fig. 2.3 Mechanisms of polarization

The ability to respond to the electric field and obtain an electric dipole moment $\vec{P}$ can be evaluated by the polarizability of a molecule. Electric dipole moments can be permanent or induced by the electric field. Generally, the polarizability α consists of four parts (Figure 2.3): electronic polarizability α_e, atomic polarizability or ionic polarizability α_a, orientation or dipole polarizability α_d, and space-charge (interfacial) polarizability α_s [67-70]. That is:

$$\alpha = \alpha_e + \alpha_a + \alpha_d + \alpha_s \text{ ----------(2.6)}$$

Electronic polarization α_e is caused by the slight displacement of the valence electron cloud with respect to the positive nucleus of the atom under the external electric field. The atom distorts from the original position and the center of the atom's negative charge no longer coincides with the position of the nucleus, thus inducing an electric dipole moment.

Atomic (or ionic) polarization is induced by the displacement of some charged atoms or groups of atoms with respect to each other, i.e., the molecular vibrations in the applied field. The bond length of the molecule can be compressed or stretched depending on the relative orientation between the ionic bond and the electric field. As the molecule is bent and stretched by the applied field, its electronic distribution and nuclear position become distortion, thereby its dipole moment changes accordingly. In this way, even nonpolar molecules may gain an induced dipole moment in an electric field.

Orientation or dipole polarization rises from re-orientation of the permanent dipole moments in the field. The permanent dipole moment stems from the partial charges on the atoms in the molecule that arise from the different electronegativity or other features of bonding. In the polar molecules or some ionic materials, the molecules may have an electric dipole moment even in the absence of an applied electric field. When no electric field is applied, the molecules are randomly oriented and no net charge exists in the material. However, under the influence of an external electric field, the dipoles will rotate and tend to align themselves in a direction paralleled to the applied field so as to cancel part of the applied field, thus leading to an orientation polarization. The contribution of this process of orientation of the permanent dipoles to the polarization is called orientational polarization.

These three types of polarization are due to charges that are locally bound in atoms, in molecules, or in the structures of the materials. From equation 2.5, the total polarization of these three types of polarization is expressed as follow:

$$\vec{P} = N(\alpha_e + \alpha_a + \frac{\mu^2}{3\kappa T})\vec{E}' \text{ ----------(2.7)}$$

where N is the number of molecules per m^3, μ denotes the orientation polarization polarizability, κ represents the Boltzmann constant, and T signifies the temperature in K. The terms α_e and α_a are the electronic and atomic (or ionic) polarization in the molecule, respectivity. The term $\frac{\mu^2}{3\kappa T}$ rises from the thermal averaging of permanent electric dipole moments in the presence of an applied field.

In equation 2.7, the locally acting electric field $\vec{E}'$ at elementary particle is the sum of the electric field $\vec{E}$ from external sources and the field from the nearby dipoles. There are several models to develop the expression for the local field at a general lattice site. One typical expression for the locally acting electric field $\vec{E}'$ is the Lorentz relation:

$$\vec{E}' = \vec{E} + \frac{1}{3\varepsilon_0}\vec{P} \text{ ----------(2.8)}$$

The quantitative relation between the relative dielectric constant (or relative permittivity) and the properties of the molecules can be described by Debye equation, which can be derived from equation (2.4), (2.7) and (2.8) as following:

$$\frac{\varepsilon_r - 1}{\varepsilon_r + 2} = \frac{N}{3\varepsilon_0}(\alpha_e + \alpha_a + \frac{\mu^2}{3\kappa T}) \text{ ----------(2.9)}$$

Another format of (2.9) can be rewritten as following [(71)]:

$$\frac{\varepsilon_r - 1}{\varepsilon_r + 2} = \frac{\rho}{M}\frac{N_A}{3\varepsilon_0}(\alpha_e + \alpha_a + \alpha_d) \text{ ----------(2.10)}$$

where ρ is the density, M is the molecular weight, and N_A is the Avegadeluo Constant. If there is no permanent dipole moment contribution, equation (2.9) can be written as the Clausius-Mossotti equation:

$$\frac{\varepsilon_r - 1}{\varepsilon_r + 2} = \frac{N}{3\varepsilon_0}(\alpha_e + \alpha_a) \text{ ----------(2.11)}$$

Space charge polarization or interfacial polarization arises from accumulation of charges at the interface. Generally, charge carriers can migrate for some distance through the dielectric, but when such carriers are impeded or trapped in their motion

by a physical barrier that inhibits charge migration, space charges and a macroscopic field distortion will be resulted, thus creating space charge (or interfacial) polarization. Surface roughness, defects and impurities can cause large increase in space charge polarization. The space charge polarization usually happens in heterogeneous materials. In these materials, charge carriers may move more easily through one phase but be constricted at phase boundaries. As a result, charges accumulate at interfaces and can be polarized in an applied field. This effect often depends greatly on the conductivities of the phases in the materials.

2.3 Frequent Dependence of Dielectric Constant

If the external electric field is an ac field, the frequency of the signal will affect the polarization phenomena described above [69, 72,73]. Figure 2.4 shows the frequency dependence of dielectric constant with the contribution of polarization mechanisms.

When the frequency of the applied electric field exceeds the characteristic frequency (or critical frequency) of the motion that contributes to the polarization, the dielectric constant is decreased because those motions can no longer follow the time varying field. At frequency above visible optical range, only electronic polarization can follow the electric field almost instantaneously as only the displacement of bound electrons is involved. The mechanism of polarization gives rise to a resonance absorption peak in the optical range, as shown in figure 2.4. Completely covalent structures strongly contribute to electronic polarization even in low frequencies. The index of refraction of the material also depends on the electronic polarization. In this

high frequency range > 10^{14} Hz (visible to ultraviolet range), the dielectric constant is approximately equal to the square of the refractive index if the extinction coefficient of the material can be omitted. Since the ionic (or atomic) polarization requires the displacement of the entire atoms, it can not respond to fast changing electric fields as rapidly as the electronic polarization. It occurs at frequencies in the infrared rang (10^{12}~10^{13} Hz). In contrast, the orientational (or dipolar) polarization involves the motion of complete molecules, so it appears at low frequency. Interfacial or space charge polarization, however, can only follow lower frequency because it demands the migration of charges through the body of the material.

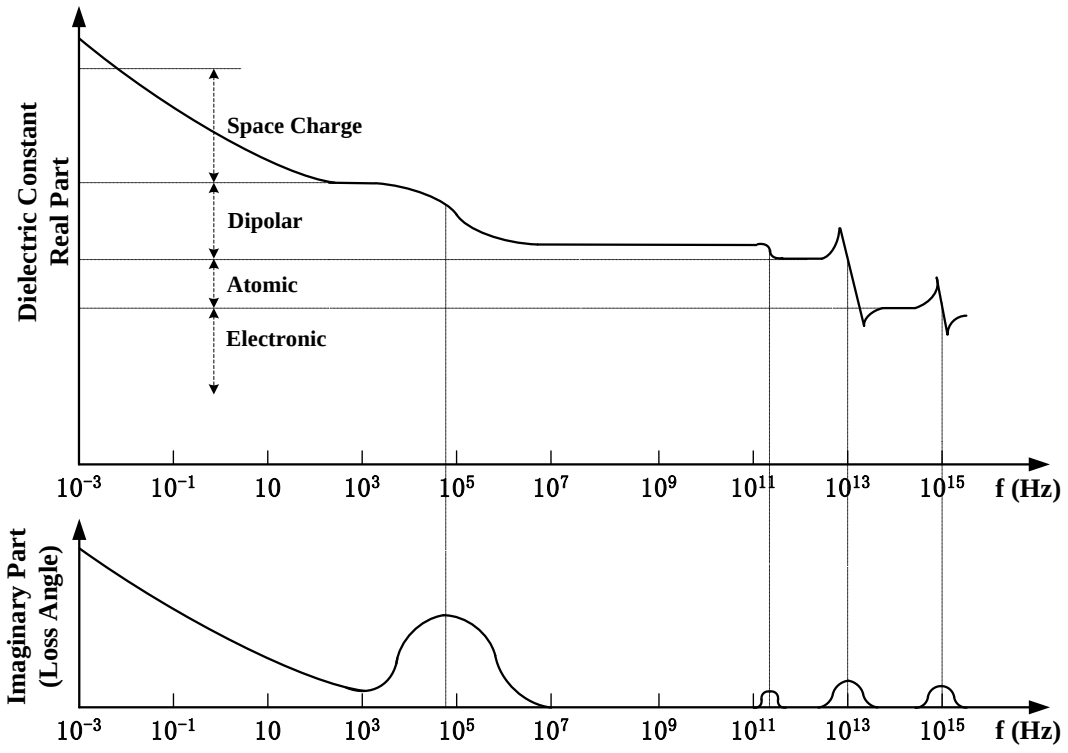

Fig. 2.4 Frequency dependence of polarization mechanisms

In the frequency spectrum of the dielectric constant shown in Figure 2.4, there are resonance frequencies at about 10^{15} Hz for electronic polarization and $10^{12} \sim 10^{13}$ Hz for atomic polarization. Such resonance frequency stems from a counter-active restoring force, which subjects to both electronic and atomic polarization. However, orientation polarization is opposed by thermal disorder instead of counter-active restoring force. Therefore, it does not give rise to a resonance at a critical frequency, but shows critical frequency as relaxation. One critical frequency of relaxation for orientation polarization at high range ($\sim 10^{11}$ Hz) is on account of the rotation of the permanent dipole moment of the molecules against an elastic restoring force about an equilibrium position. Another critical frequency at the range of $10^3 \sim 10^6$ Hz involves the rotation of dipoles between two equivalent equilibrium positions. The frequency behavior of interfacial or space charge polarization depends on the physical barrier that inhibits mobile charge carrier migration. The frequency of sensitivity for interfacial polarization can range from less than 10^{-3} Hz to 10^3 Hz with the change of the barrier structure and the density of charges. In the frequency range of 10^3 Hz, it may be impossible to distinguish the frequency response of a dipole polarization mechanism and an interfacial polarization mechanism.

As the frequency dependence of the real part of the dielectric constant, the imaginary part of the dielectric constant responses to the counteractive restoring force in case of electronic and distortion polarization, the thermal disorder in case of orientation polarization, and the barrier structure and charge density in case of interfacial polarization. The response of the imaginary component of the dielectric constant to the current in the dielectric is no longer exactly $\pi/2$ out of phase with the

electric field, thus resulting in the dissipation (usually represented by loss angle) in the dielectric at the specific frequencies.

Since the application frequencies of microelectronics system is typically less than 10^9 Hz, all the above four components contribute to the dielectric constant and they should be minimized for optimum performance. It should be noted that orientation polarization and space charge polarization contribute largely not only to the real part of dielectric constant, but also to the imaginary part of the dielectric constant which can lead to heat dissipation. In addition, space charge polarization can result in reliability issue for the circuit system. Therefore, it is very important to prevent the orientation and interfacial polarization in the low-k material as much as possible.

2.4 Methods to Reduce Dielectric Constant

Equations (2.6) ~ (2.11) indicate that decrease of all components of polarization (electric, ionic, dipolar and interfacial) or any of them can reduce the dielectric constant of the materials. The materials which consist of atom with low atomic mass, such as C, H, F, usually possess low dielectric constant. Table 2-1 shows more details about some typical electronic polarizabilities and the associated bond enthalpies. The data suggest that covalent (single) bonds with low polarizabilities, e. g. C-H, C-C, C-F, can reduce the dielectric constant. Therefore, incorporation of these atoms (C, H, F) into a given material is particularly effective in lowing the polarizability. Since polar substituents, such as hydroxyl (-OH) and

carbonyl (–C=O) groups, can both increase the orientational component of the polarizability and adsorb water which has large permanent dipole moment, it is wise to avoid the use of such units to design low k materials.

Table 2.1 Electronic polarizability [74] and bond enthalpies [75].

Bond	Polarizability (A^3)	Average bond energy (Kcal/mol)
C-C	0.531	83
C-F	0.555	116
C-O	0.584	84
C-H	0.652	99
O-H	0.706	102
C=O	1.020	176
C=C	1.643	146
C≡C	2.036	200
C≡N	2.239	213

Reducing the density of materials is another effective method to lower the dielectric constant. The qualitatively estimated relationship between the density and the dielectric constant has been related as equation (2.10). It suggests that the dielectric constant of any material can be reduced by decreasing the density. The density can be reduced to a lower level by using lighter atoms or introducing more free space around the atoms. For example, incorporation of light, less space-occupying groups such as H or/and CH_3 in the SiO_2 network can significantly lower the material density and hence the dielectric constant A technological method to reduce film density is introduction of pores into the dielectric materials. The porous materials can be simply modeled as two- component materials: the solid skeleton and

pores. If the dielectric constant of the material inside the pores is ε_1, the dielectric constant of the pore wall material is ε_2, and the film porosity is P, then the dependence of the relative permittivity of porous film on film porosity can be deduced from equation (2.9) as following:

$$\frac{\varepsilon_r - 1}{\varepsilon_r + 2} = P\frac{\varepsilon_1 - 1}{\varepsilon_1 + 2} + (1 - P)\frac{\varepsilon_2 - 1}{\varepsilon_2 + 2} \text{----------(2.12)}$$

If the pores are empty, then $\varepsilon_1 = 1$ and the terms $P(\varepsilon_1-1)/(\varepsilon_1+2) = 0$, and (2.12) should be described as following:

$$\frac{\varepsilon_r - 1}{\varepsilon_r + 2} = (1 - P)\frac{\varepsilon_2 - 1}{\varepsilon_2 + 2} \text{----------(2.13)}$$

Hrubesh et al [(76)] had demonstrated equation (2.13) with their experiment.

Chapter 3

Experiment Procedure

3.1 Why Use PECVD to Deposit Low-k Materials in This Project?

Chemical vapor deposition (CVD) is defined as the formation of a nonvolatile solid film on a substrate by the reaction of vapor-phase chemicals (reactants) that contain the required constituents. The first CVD techniques were employed in the late 1880's to coat thin metallic films onto incandescent filaments [77-79]. Today, CVD techniques become one of the two dominant techniques (another one is physical vapor deposition (PVD) such as evaporation and sputtering fall) for depositing thin films in industry, because it offers many advantages in a continuous process for depositing uniform, adherent, homogeneous and reproducible film with excellent step coverage on large areas at large deposition rates with low cost. In semiconductor processing, CVD technique is most often used for film deposition of dielectrics, polysilicon, metal and metallic compounds. Traditionally, the most common deposition methods for dielectric films are atmospheric pressure CVD (APCVD), low-pressure CVD (LPCVD), and plasma-enhanced CVD (PECVD).

PECVD was first reported [80] in 1965 by Sterling and Swan for the deposition of amorphous silicon, SiO_2, and Si_3N_4 with plasma instead of thermal activation to impart the necessary energy for the reaction to occur. PECVD uses a radio frequency (RF) source of power to generate a glow discharge to transfer energy into the reactant gases, allowing the deposition on the substrate at a lower temperature than in APCVD or LPCVD processes. Hence, low deposition temperature is the major advantage of

PECVD. This characteristic is very important for low dielectric constant (k) materials deposition, because most low-k materials are not stable at high temperature.

The ability to produce films of unique compositions and properties is the other advantage of PECVD. By changing the deposition conditions in a PECVD system, non-stoichiometric films with special structure can be deposited, such as SiOC:H. Desirable properties like low dielectric constant, good adhesion, low pinhole density, adequate electrical properties, and compatibility with fine-line pattern transfer processes can also be obtained in these PECVD films.

It should be noted that High-Density-Plasma CVD (HDP-CVD) is not preferable to this project. One advantage of HDP-CVD is to deposit dielectric films into high-aspect-ratio, narrow spaces without forming voids in the dielectric film. However, inter-metal dielectric (IMD) gap-fill ability is no long necessary for Cu damascene process to form Cu/low-k architecture. In addition, the different types of HDP-CVD, such as electron-cyclotron-resonance CVD (ECR-CVD) and inductively coupled plasma CVD (ICP-CVD), can generate plasma-induced charging damage [(81)] due to high ion density and high energy bombardment in the sputtering component. This damage has been observed mainly during plasma etching and ashing, however it can also occur erratically during plasma assisted IMD deposition. It introduces a formidable challenge to process development that lies ahead as critical dimensions shrink to 0.18um (transistor gate length) and below, as gate oxides get thinner (≤5nm), and as more metallization levels (>6) are required. Furthermore, severe corner sputtering in HDP-CVD can result in undesired materials (such as metal contamination or impurities) in the oxide causing device failures.

Therefore, RF-power PECVD is a more suitable choice for low-k IMD deposition. For this project, PECVD system in Institute of Microelectronics (IME) can be used to deposit silicon-based low-k materials: a-SiCO:H.

3.2 PECVD Deposition System

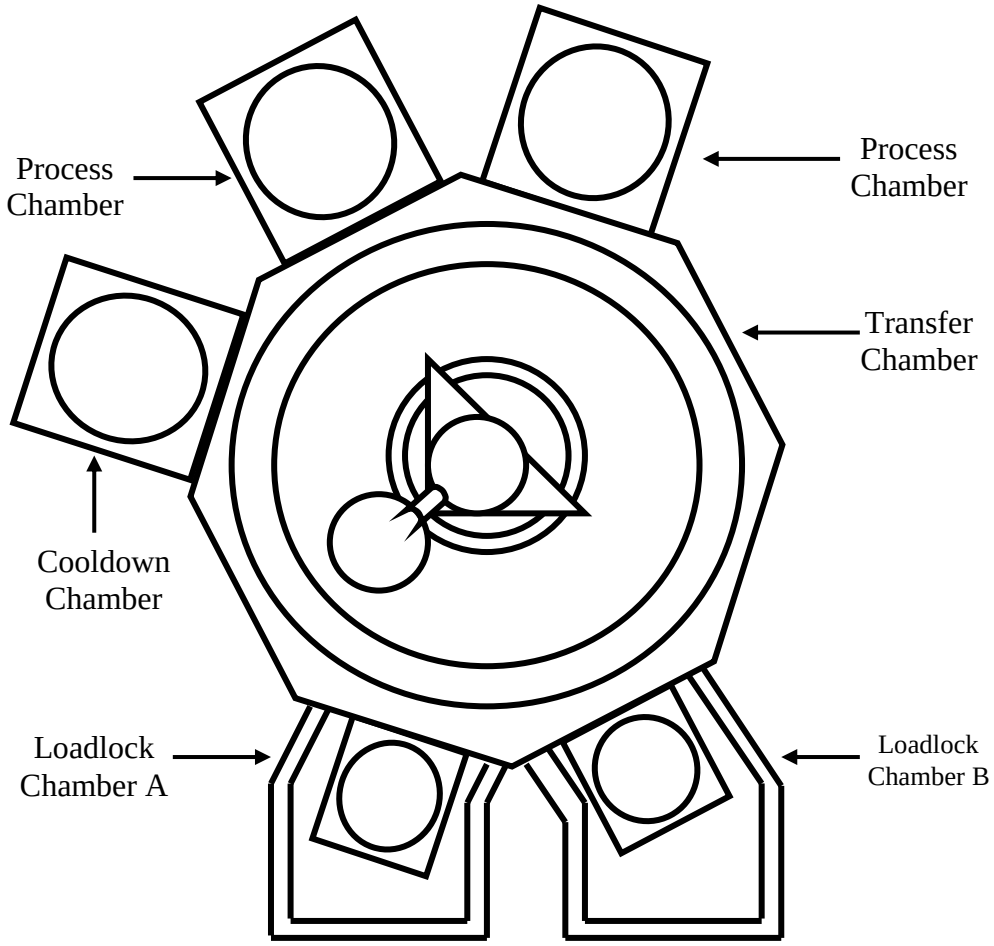

Fig. 3.1 Schematic diagram of the multi-chamber of CENTURA System 5200

At IME, there is a fully automated PECVD system, CENTURA System 5200 (Applied Materials, Inc.), that can accommodate 200mm diameter wafers. This

system employs a single-wafer, multi-chamber design, thus allowing for precise control of all process parameters to enhance uniformity between wafers (Figure 3.1).

Two independently operated loadlock chambers (LLA and LLB) provide independent I/O ports for loading and unloading wafer cassettes and index for wafer selection. They are operated at atmospheric pressure for loading and unloading, and at reduced pressure for system operation. The transfer chamber located in the center of the mainframe contains a robot arm that transfers wafers between the loadlock and other chambers or between chambers. The cool down chamber is used for cooling newly processed wafers. Two independently operated process chambers (A and B) are bolted to the transfer chamber. They contain the wafers for processing and maintain process parameters based on the chamber recipe. The direction of wafer flow is shown as following:

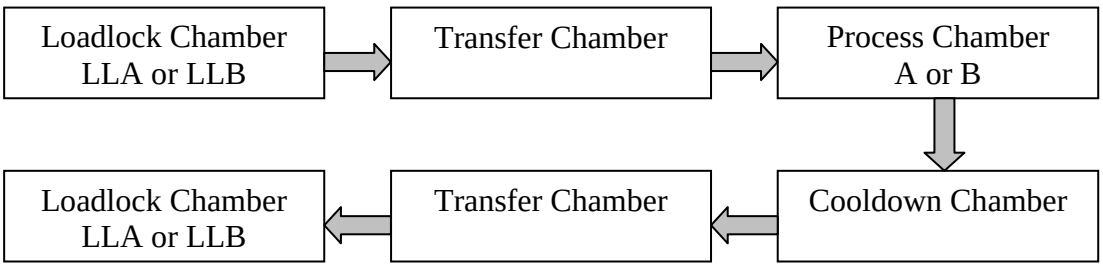

The process chamber is a showerhead reactor clustered with a single radio frequency (RF) structure, and employs a perforated planar surface to dispense reactant precursors over another parallel planar surface to deposit films on an 8-inch wafer. Every process chamber can act as a parallel-plate radio-frequency (RF) PECVD reactor. The plasma is sustained with a RF power generator at 13.56 MHz. The two electrodes of the process chambers are about 216 mm in diameter. This

symmetric configuration will not induce DC bias, thus leading to low density films, which important for obtaining low k values. The electrode spacing in process chambers A and B are about 11.9 mm and 6.7 mm respectively. Each chamber uses an electric heater to heat the wafer to provide the energy for chemical reaction in the CVD process. The heater itself also serves as the pedestal to hold the wafer thus simplifying the design. Mass flow controllers (MFC) are used to accurately measure and control the gas flow. The pressure control of the CVD chamber is provided through the vacuum subsystem. The RF matching allows maximum transmission of RF power from the RF generator. The chamber RF delivery system has a 50 ohm high frequency generator without coaxial cable. It uses a fix match instead of an automatic tuning match network, and it operates into a load that can vary over a certain impedance range. Both the 2 chambers can be used to deposit films separately.

One of the major advantages of plasma deposition processing is its flexibility for deposition films with desirable properties. In PECVD systmes, physical and chemical properties of the deposited low-k IMD films can be altered by varying deposition parameters such as gas flow composition and ratio, pressure, RF power, substrate temperature, DC bias.

Gas flow composition and ratio are the key parameters that determine the properties of the film deposited on the substrate. Amorphous SiOC:H can be deposited using different kind of precursors and gas ratio. In order to obtain optimum low-k IMD film, the flow ratio of the precursors must be carefully selected and adjusted.

The pressure in the chamber can determine the concentration of reactants and the mean free path. It can affect the film formation process (e.g. deposition rate) and the film properties. For low-k IMD film deposition, the pressure is usually adjusted to suitable region so that porosity structure can form in the film.

RF power ionizes the reactant gases and also establishes and sustains the plasma. It can affect the density of ionized species and free radicals in the plasma. High RF power will increase deposition rate. RF power may be varied to suit the gas species, gas composition, flow rate and process pressure. In order to keep the plasma stable, RF power must be tuned so that load can absorb maximum power and reflect minimum power.

Substrate temperature plays an important role in determining film properties and deposition process. It affects not only the growth rate, but also composition and microstructure of the film.

The DC bias voltage determines the energy of the ion bombardment on to the substrate and mainly affects the density, adhesion and other properties of the film. The magnitude of the induced DC bias is inversely proportional to the gas pressure in the system, and related largely to the effective area ratio of the two electrodes and the kinds of the reactant species in the plasma. Varying the RF power will change the DC bias in PECVD system. For HDP-CVD, RF power and DC bias can be independently adjusted.

Treatment of substrate before deposition, and treatment of film and/or annealing film for a moment after deposition may affect some properties of the film.

3.3 Characterization techniques and equipments for the film properties

Several techniques and tools are used to evaluate the properties of the low-k film in this project. They include mercury probe C-V measurement system, Fourier transform IR spectroscopy, Ellipsometry, etc. Thickness, refractive index, dielectric constant, FTIR spectra, and some other properties of the film can be measured using these equipments.

3.3.1 Dielectric Constant Measurement Tool

Dielectric constant, as breakdown voltage and leakage current can be evaluated from C-V and I-V characterization. Usually, dielectric film is first deposited on the silicon surface. Then a layer of metal film (e.g. aluminum) is deposited on it, and finally the C-V and I-V characterizations are carried out on this metal-insulator-semiconductor (MIS) structure. In IME, there is no need to deposit the metal electrode if the SSM 495 is used to measure the C-V and I-V characterizations. SSM 495 Automatic Mercury Probe CV Measuring System (Solid State measurements Inc.) uses liquid mercury to make a non-destructive electrical contact. CV measurements can be made at frequencies of 0.1MHz and 0.9216MHz. For low k dielectric I-V characterizations, breakdown field (electrical strength) is usually measured at 1mA/cm^2, and leakage current is measured at 0.5MV/cm.

3.3.2 Measurement tool for thickness and refractive index (n)

The thickness and refractive index (n) of the film can be measured at 633nm on Opti-Probe 5000 (Therma-Wave, Inc.) which is integrated with three different technologies: full range spectrometry, Beam Profile Ellipsometry ™ (BPE™), and Beam Profile Reflectometry ™ (BPR™). Full range spectrometry uses a variety of dispersion modeling techniques to measure reflectivity and visible/UV (thickness, n and k). BPE™ measures amplitude and differential phase shift for two polarizations of the light reflected from the film and substrate. BPR™ measures reflectivity as a function of angle of incidence for two mutually perpendicular polarization directions. It can eliminate errors due to wavelength dispersion when used together with the standard spectrometry and ellipsometry techniques, so that the Opti-Probe could measure precisely film stacks without seed values and brackets which tools lacking this technology often need. The measurement range of thickness is from 0 Å to 150,000 Å.

3.3.3 Fourier transform Infrared (FTIR)

FTIR absorption spectra are collected on QS 2200A/QS2200ME System (Bio-Rad Laboratories, Inc.) At any temperature above absolute zero, molecule vibration will occur because the atoms in the molecule have kinetic energy and will be oscillating about their equilibrium positions. Molecule vibration includes stretching and bending of the chemical bonds in the molecule. Each of the vibration at mode of different molecules associates with unique characteristic energy in the range of infrared. The vibration will become IR active when it associates with the change of dipole moment (shown in Fig. 3.2). Each IR active vibration has its own

characteristic IR absorption. The complex vibrations of any molecule can be described by combinations of its "normal vibration" modes, and generate the infrared absorption spectrum. Each absorption band, with its position and intensity, is characteristic of a particular chemical bond in a particular molecule. Therefore, FTIR absorption spectra are used to characterize the different bonds in the film. It can also be used to qualitatively estimate the content of some elements in the film.

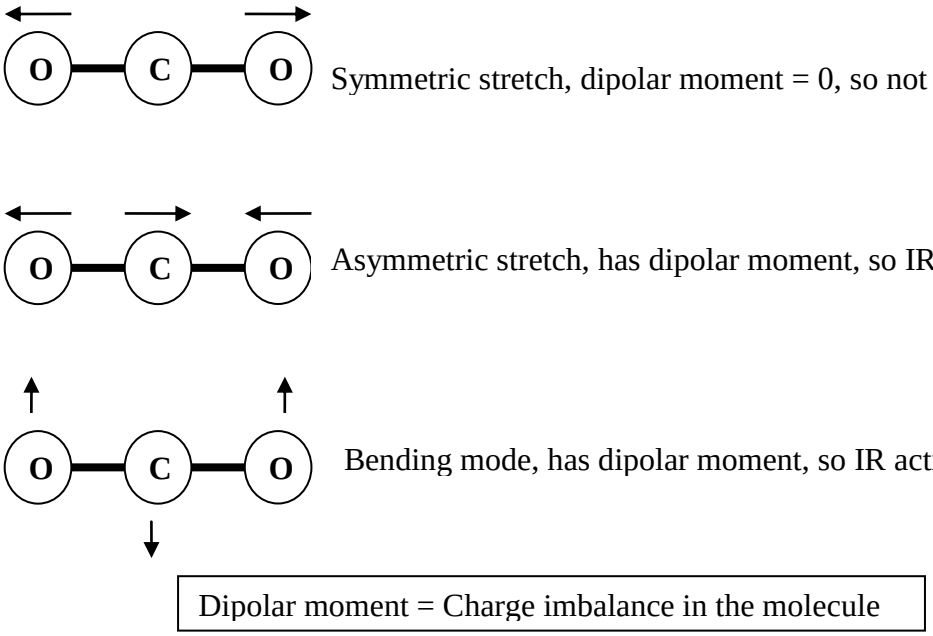

Fig. 3.2 Normal vibrations of a tri atomic molecule

3.3.4 Hardness and Young's modulus

Nanoindentation techniques (Nanoindenter II, Nano Instruments, Inc.) are used to investigate the hardness and Young's modulus of the films by analyzing the loading and unloading curve. It is a new method to characterize the mechanical

properties of materials on a nanometre scale [82-84] very quickly and conveniently without sample preparation step. The valuated samples could be features less than 100 nm across and thin films less than 5 nm thick. Test methods include indentation for comparative and quantitative hardness measurements. In normal depth sensing indentation, an unloading curve can determine the stiffness of contact, from which the hardness and Young's modulus of the films are then calculated. Much thick film has a good unloading curve, but for thin films, the results are inevitably affected by the substrate. To exclude the substrate effect on the measured hardness and Young's modulus of the films, the continuous stiffness measuring capability of the Nanoindenter II is used. This technique provides a method of continuously measuring the film stiffness in a single indentation without the need for discrete unloading cycles. It allows the measurements to obtain the hardness and young's modulus continuously and simultaneously at every data point acquired during the indentation displacement at small penetration depths. A Berkovich-geometry diamond tip is used, and the indenter is operated in the constant displacement rate mode. Three indents are made per film.

3.3.5 Surface Energy analysis and contact angle measurement

Surface free energy, or surface tension, arises from the unbalance of the forces between atoms or molecules inside and at the phase boundary. It can be determined by contact angle measurement (see Fig. 3.3). The measurement of the contact angle of films are carried out in atmospheric conditions at a temperature of 20^{o}C using an OCA device from Data Physics Instrument. In order to calculate the surface free energy of the film, two kinds of test liquids (wafer and formamide) with their known surface energy as well as their dispersive and polar component, are used in the

contact angle measurement. In this measurement, a droplet with the volume of 0.5 μl is released onto the surface of the sample from a syringe needle. After 10 seconds when the liquid drops reach the equilibrium, a CCD camera is used to capture the contour of the liquid drop on the solid surface. Then the contact angle is determined as shown in Fig 3.3. For each sample, the contact angle is measured at least three times. The accuracy of the contact angle is less than 1^{o}.

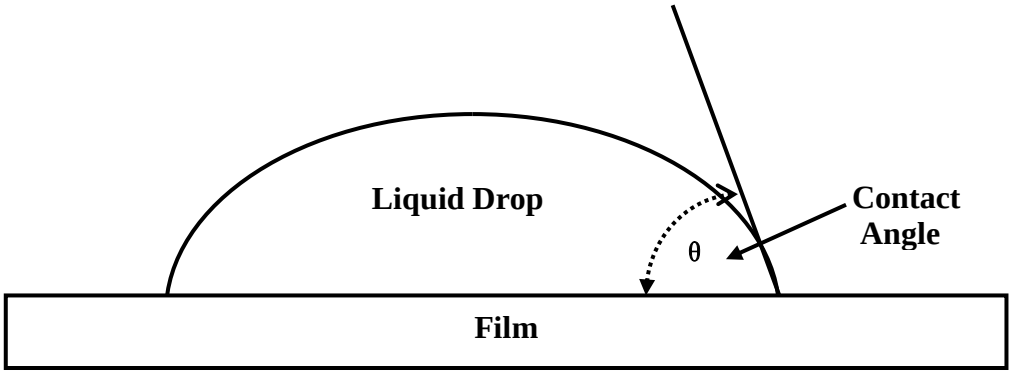

Fig. 3.3 Contact Angle Measurement

Chapter 4

Investigation of Deposition Temperature Effect on Properties of PECVD SiOCH Low k Films

4.1 Introduction

As discussed in Chapter two, carbon-doped dioxide (SiOCH) deposited by PECVD technique using organosilicon gases as precursors is one of the most prospective candidate of low k material for advance interconnect application in term of low dielectric constant, cost saving, ease of retrofit on current industry-standard, and commercial available precussors. In order to dope carbon and hydrogen into the silicon dioxide network, suitable precussor and oxidizing agent should be selected at first.

SiH_4 is the most widely used inorganic precursor for depositing un-dope silicon dioxide. It is logical to get doped silicon dioxide with modified SiH_4 as precussor. If carbon and hydrogen are needed to be doped into silicon dioxide, SiH_4 (the precussor) should be modified by replacement of H with some groups which contain carbon atom. The simplest case for such modification is to replace H in SiH_4 with methyl group $-CH_3$. Silane precursors: Methylsilane (SiH_3CH_3), dimethylsilane ($SiH_2(CH_3)_2$), trimethylsilane (3MS, $SiH(CH_3)_3$) tetramethylsilane (TMS, $Si(CH_3)_4$) will come out if one, two, three, or all of four hydrogen atoms in SiH_4 are replaced by methyl group $-CH_3$. This family of materials $(CH_3)_xSiH_{4-x}$ (x=1,2,3,4) have already been commercially available. The reaction chemistry to synthesize the compounds $(CH_3)_xSiH_{4-x}$ is briefly described as follows[(85)]:

$$CH_3Cl + Si(metal) \rightarrow (CH_3)_x SiCl_{4-x} + (CH_3)_4 Si \quad \text{----------(4.1)}$$

$$(CH_3)_x SiCl_{4-x} + (CH_3)_4 Si + LiAlH_4 \rightarrow (CH_3)_x SiH_{4-x} + reaction by-products \quad \text{----------(4.2)}$$

Firstly, methylchlorosilanes are formed by chlorinating silicon-metal compound. Then these materials are chemically reduced by replacement of the chlorine atom with a hydrogen atom. Finally, the compounds are synthesized as well as other reaction by-products. Changing the ambient reaction conditions (e.g. pressure, temperature, etc.) can control the yields of the different methylsilanes.

Table 4.1: Basic Properties of $(CH_3)_xSiH_{4-x}$ Precursors

		CH_3SiH_3	$(CH_3)_2SiH_2$	$(CH_3)_3SiH$	$(CH_3)_4Si$
Material Phase at 20 ^{0}C		Gas	Gas	Gas	Liquid
Dissociation Energy (kcal/mol)	Si-H Bond	89.6	89.4	90.3	99.2 (CH_2-H)
	Si-CH_3 Bond	88.2	88.1	88.1	89.4
Vapor Pressure at 20^{0}C (torr)		10249	2964	1218	601
Approximate Boiling Point (^{0}C)		-57	-20	7	27
Hazards		Flammable-Pyrophoric due to SiH_4 impurity		Flammable	

The basic physical properties of the methylsilane compounds are listed in Table 4.1. It is clear that trimethylsilane ($(CH_3)_3SiH$, or TMS, or 3MS) and

tetramethylsilane ($(CH_3)_4Si$, or 4MS) are safer than CH_3SiH_3 and $(CH_3)_2SiH_2$, as well as SiH_4.

In plasma-based processes, the plasma decomposition of the $(CH_3)_xSiH_{4-x}$ precursors generates some Si-C compounds named silenes (neutrals) and silylenes (bi-radicals).

$$(CH_3)_x SiH_{4-x} + h\nu \rightarrow \begin{matrix} CH_2 = SiH_2(\alpha) + CH_2 = Si(H)CH_3(\beta) + CH_2 = Si(CH_3)_2(\gamma) \\ + \\ CH_2^* - ^* SiH_2(\alpha) + CH_2^* - ^* SI(H)CH_3(\beta) + CH_2^* - ^* Si(CH_3)_2(\gamma) \end{matrix} \quad (4.3)$$

These Si-C-based meta-stable compounds are responsible for highly efficient incorporation of carbon into the plasma deposited film relative to process chemistry that employs separate Si and C precursors. The number of carbons and bonding by which carbon is linked to the silicon in the silane determines the amount of carbon which is carried to the substrate and available for incorporation into the film. Once the reactive species are adsorbed, they can be incorporated into the film network through reaction with surface Si-H or C-H bonds and subsequent elimination of hydrogen gas or methane.

In formula (4.3), monomethylsilane (CH_3SiH) generates more α species and larger amounts of SiH_x*, and tetramethylsilane (4MS) produces γ species and $(CH_3)_3SiCH_2$-H, but only trimethylsilane (3MS) yields comparable amounts of all

three species, α, β, and γ. Therefore, it is more efficient to deposit organosilicate (OSG) by PECVD using 3MS precursor than other $(CH_3)_xSiH_{4-x}$ precursors.

The oxidizing agent is usually N_2O, NO, O_2, H_2O_2, CO_2, or O_3. However, N_2O and NO gas can easily introduce nitrogen atoms into the low-k film, and nitrogen atoms are known to form poisoned-via holes in the dual damascene process, so N_2O and NO gas cannot be used. H_2O_2 is not good choice because H_2O_2 may introduce water or –OH group into the film thus resulting in high dielectric constant. Therefore, oxygen (O_2) gas, the most popular oxidant gas, is used as oxidizing agent in this project.

In this chapter, carbon-doped hydrogenated silicon oxide (SiOCH) films are deposited on p-type Si (100) substrates by using PECVD with trimethylsilane (3MS) and oxygen as precursors at different deposition temperatures. The deposition rate, bonding structure, electrical and mechanical properties will be discussed.

4.2 Experiment

All the SiOCH films investigated in the present study are deposited in a parallel-plate radio-frequency (RF) PECVD reactor. The plasma is sustained with a 600 watt RF power generator at 13.56 MHz under 4 torr pressure. Process gases consisted of trimethylsilane ($SiH(CH_3)_3$, referred to as 3MS, Semiconductor Grade) and oxygen, with the $3MS/O_2$ gas flow rate ratio fixed at 6. The substrates are 200mm single-side polished <100> p-type (boron-doped) silicon wafers with ρ=1~10 Ωcm. The temperatures vary from 200^0C to 400^0C during deposition. To study the thermal

stability, the as-deposited films were annealed at 450, 500, 600, 700, and 800°C for 30 min at N_2 ambient using the system TEL ALPHA-8S-ZVFNS.

Film thickness and refractive index (n) value at 632.8 nm are measured by the 5240i Opti-Probe system. The deposition rates are calculated from the film thickness and deposition time. Bond structures of the films are characterized spectroscopically by using Fourier transform infrared (FTIR). The acquisition number of each FTIR spectrum is 64 with resolution of 4 cm^{-1} over a wavenumber range between 4000 and 400 cm^{-1}. Dielectric constant is evaluated at frequency of 0.9216 MHz on mercury probe CV measuring system. The hardness and Young's modulus of film are investigated by a nanoindenter with a Berkovich diamond tip pyramid-shaped with an angle of 65.3 normal to the base.

4.3 Deposition of SiOCH low k films

Generally speaking, the deposition mechanisms for plasma CVD process can be divided into several sequential steps: (1) Mass transportion of the gaseous reactants from the reactor inlet to the deposition zone; (2) Production of new reactive species and byproducts from Chemical reactions in the gas phase; (3) Mass transport of the initial reactants and reaction products to the substrate surface; (4) Adsorption of these species to the substrate surface; (5) Surface migration of adsorbed species over the surface to the growth centre; (6) Surface reactions at the growth centre; (7) Desorption of by-products; (8) Diffusive mass transport of the by-products away from the surface; (9) Mass transportation of the by-products to the outlet of the reactor. The above 9 steps could be grouped into three major process steps: the gas phase diffusion

with steps of (1), (3), (8) and (9), the gas phase reaction with step of (2), and the surface reaction with steps of (4), (5), (6) and (7). Each of major process steps has its own characteristics of dependence on the process conditions. The gas phase diffusion relies on the travel distance and mean free path (or diffusion coefficient) of the intermediates, which is affected by susceptor spacing, gas molecular size and chamber pressure. The gas phase reaction is controlled by the chamber pressure, reactant concentration (adjusted by gas flow rate), and temperature inside the gas phase, which depends on the thermoconductivity of the gas phase molecules; Surface processes are dominated by the surface temperature and less affected by the total pressure inside the chamber.

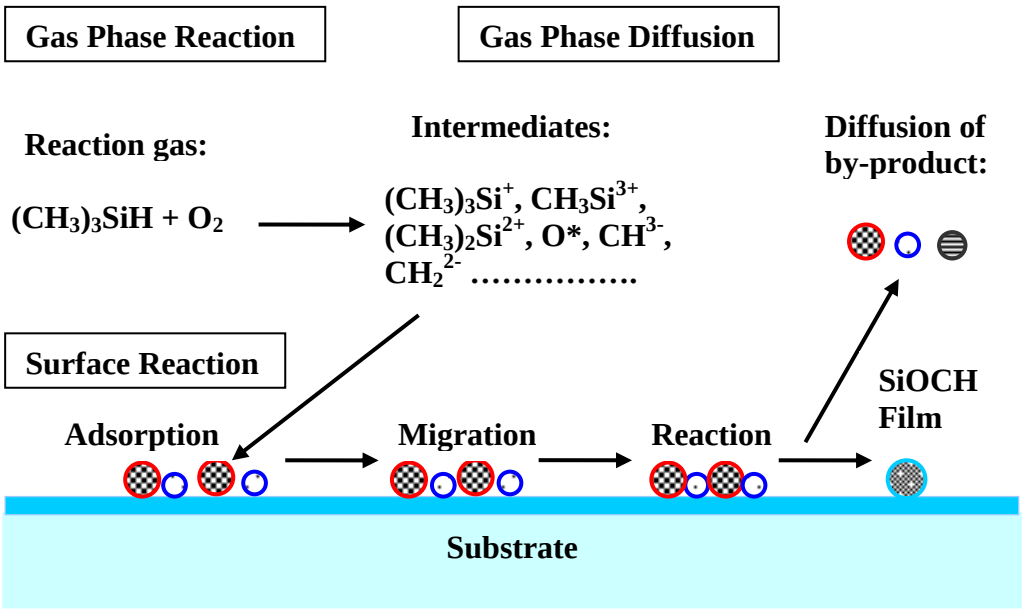

Fig. 4.1 Reaction process steps of SiOCH low k film deposition using 3MS and O_2

Fig 4.1 proposes the reaction steps of SiOCH deposition process steps using 3MS and oxygen. The primary initial electron-impact reaction between electron and reactant gases (3MS/O2) produces intermediate compounds which include ions and

radical reactive species. Then the intermediate compounds diffusion from the plasma to the substrate surface concurrently with many elastic and inelastic collisions in the plasma environment, which is classified as ion and radical generation steps [(86)]. The physisorption, migration and/or reaction of reactive species (radical absorption and ion incorporation) occur on the substrate surface. The reactive species and/or reaction products are either incorporated into the deposited films or desorbed as by-product from the substrate surface and diffusion back to the gas phase.

4.4 Result and Discussion

4.4.1 FTIR Spectra Analysis

FTIR stands for Fourier Transform InfraRed, the preferred method of infrared spectroscopy, which is an extremely analytical tool for both qualitative and quantitative analysis. This technique is based on the principle that the vibrational energy transitions associating with the dipole change in the molecules are sensitive to electromagnetic energy corresponding to the mid-infrared region (wavenumber between 4000 cm^{-1} and 400 cm^{-1}). When an infrared beam passes through a sample, some frequencies of the infrared radiation pass through (transmit) the sample, some of them are absorbed and are absent in the transmission spectrum. The transmission spectrum represents the molecular absorption and transmission, creating a molecular fingerprint of the sample. It can be used to identify the presence of specific chemical bonds in the sample based on absorptions. In this work, each FTIR spectrum of the deposited SiOCH low k films is acquired on QS 2200A/QS2200ME System (Bio-Rad Laboratories, Inc.) for 64 times with resolution of 4 cm^{-1} over a wavenumber range

between 4000 and 400 cm^{-1}. The FTIR transmission spectrum is transferred to absorption spectrum for analysis.

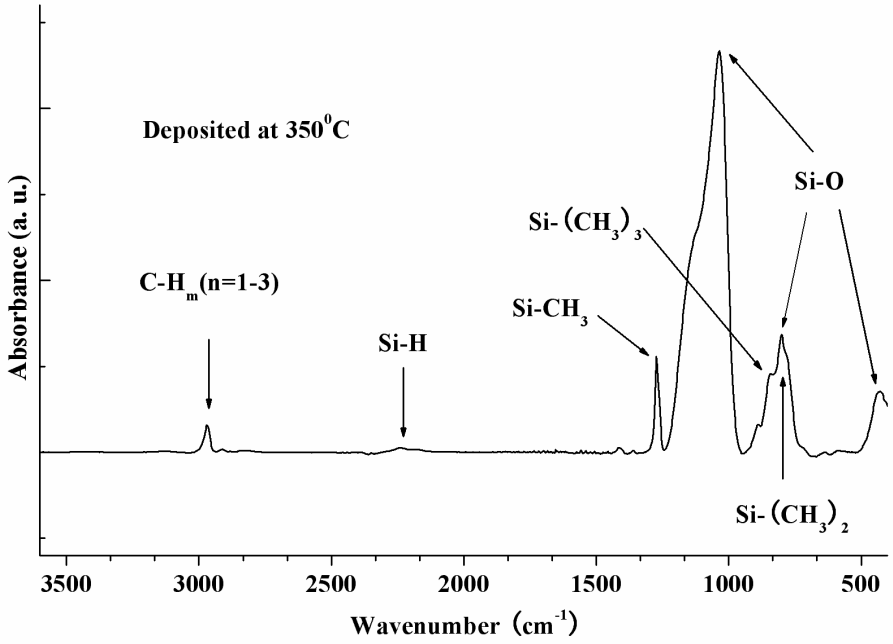

Fig. 4.2 FTIR absorption spectrum of SiOCH film

Fig. 4.2 shows a typical FTIR absorption spectrum over the range of 400~4000 cm^{-1} of the PECVD SiOCH low k film deposited at 350^{0}C. The characteristic band of such SiOCH low k film is the absorption band with a sharp peak at about 1273 cm^{-1}, corresponding to stretching vibration modes of Si- CH_3 [87-90]. Rocking vibration modes of CH_3 in Si-$(CH_3)_2$ and Si-$(CH_3)_3$ are also observed in the bands centered at about 800 cm^{-1} and 840 cm^{-1} respectively [89,90]. The peak near 2250 cm^{-1} indicates Si–H stretching band. CH_m (m = 1~3) stretching vibration modes are at the band of about 2968 cm^{-1} [88]. The absorption band centered at about 434 cm^{-1}, 840 cm^{-1} and 1034 cm^{-1}, correspond to Si-O rocking, bending and stretching vibration modes, respectively [91], which are characteristic of SiO_2 network. The broadness of the bands suggests a wide dispersal of vibrational states which is

characteristic of an amorphous network. Fig. 4.3 indicates the displacements of Si and O atoms of the three characteristic FTIR bands of Si-O-Si group [91-92]. For each band, the oxygen atom motion is in a direction opposite to that of silicon atom. In the rocking band mode, oxygen atom motion is out of the plane of the Si-O-Si bond. In bending band, the oxygen atom motion is in the plane of the Si-O-Si bond and along the direction of bisector of the Si-O-Si angle. In stretching band, the oxygen atom motion is in the plane of the Si-O-Si bond and in a direction parallel to a line joining the two silicon atoms. These strong Si-O bands exhibit in the FTIR spectrum indicates that the SiO_4 tetrahedron structure is the backbone of the film, and carbon and hydrogen are bonded into SiO_2 network.

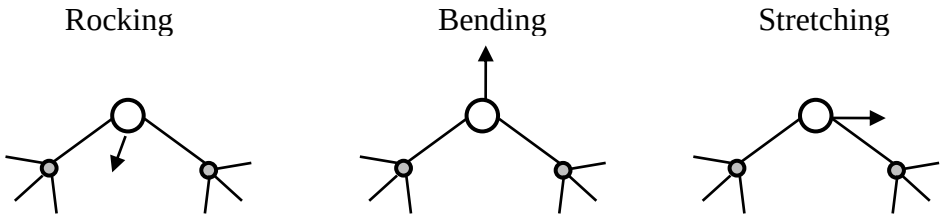

Fig. 4.3 Three Characteristic FTIR Bands of Si-O-Si group [91]

It should be noted that a strong shoulder at a wavenumber of about 1135 cm^{-1} can be observed clearly in the Si-O stretching band (see Fig. 4.2). This shoulder indicates that there is another type of structural configuration for this bond in the random covalent network of Si and O in the film. A carefully deconvolution of this band fitted with three Gaussian curves, shown in Fig. 4.4, reveals that it comprises three bands with peaks at 1027 cm^{-1}, 1061 cm^{-1}, and 1128 cm^{-1}, respectively. The bands with peaks at 1061 cm^{-1} and 1128 cm^{-1} correspond to the Si-O-Si stretch vibration in a open chain [93] and a cage (or ring) structure [94], respectively, while the

bands with a peak at 1027 cm^{-1} corresponds to the Si-O stretch vibration in C-Si-O bonds [(95)]. It is believed that the cage structure Si-O-Si can produce a microporous structure and a lower film density [(96)].

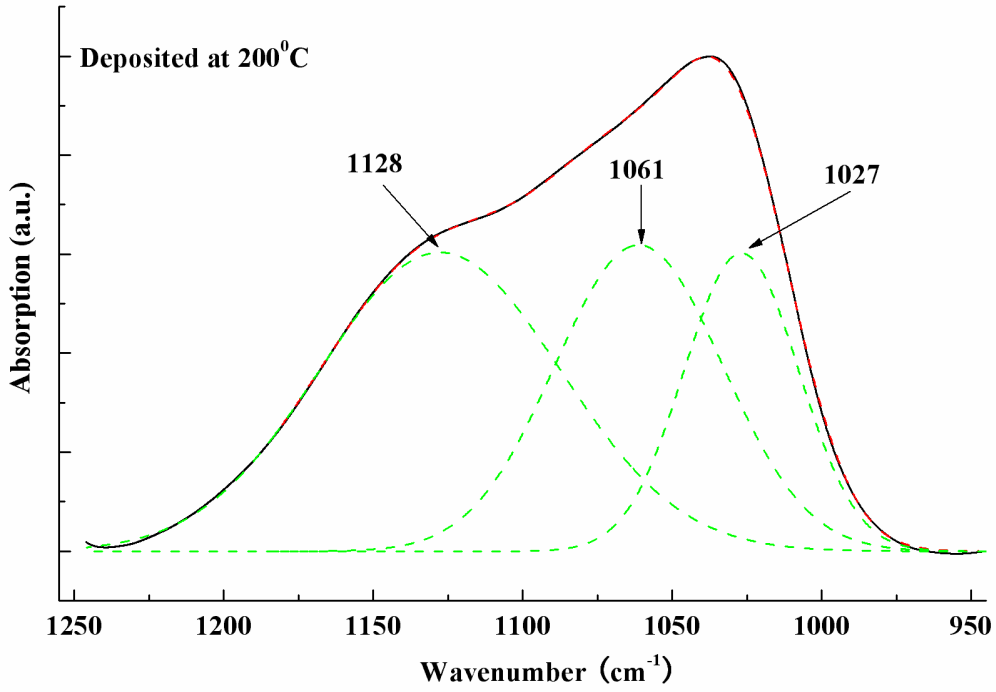

Fig. 4.4 Deconvolution of the Si-O stretching band for SiOCH film deposited at 200^0C

The magnitude of the dipole change during the vibration can affect the intensity of an absorption band. The larger the change is, the stronger the absorption band. For a particular functional group, the band intensity also depends on the number of the groups which present in the sample (molecule), the neighbouring atoms/groups, and the intramolecular/intermolecular bonding. The intensity of the absorption bands of the FTIR spectra can be used for quantification of the composition of a sample by applying Beer's law, which states that the absorbance of a kind of specie is proportional to the concentration of the specie in the sample:

$$A = \log [I(\lambda)/ I_0(\lambda)] = \alpha(\lambda) * [C] * L \quad \cdots\cdots (4.4)$$

where A is the measured absorbance, $I(\lambda)$ and $I_0(\lambda)$ are the wavelength-dependent intensity measured by the detector after the beam has passed a sample and background (without the sample present) respectively, $\alpha(\lambda)$ denotes the wavelength-dependent absorption coefficient or extinction coefficient, [C] presents the concentration of the specie in the sample, and L is the path-length of the beam through the sample (it actually is the thickness of the sample).

For the FTIR spectrum in Fig. 4.2, the relative intensity of bonds can be compared by normalizing the peak height to that of Si-O stretching band at 1034 cm^{-1}, which has the strongest peak in the spectrum. In this way, the FTIR spectra become the ratios of the measured absorbance of other bands to that of Si-O stretching band, and can be written as formula 4.5 based on formula 4.4:

$$R_i = \frac{A_i}{A_{Si-O\ stretching\ peak}} = \frac{\alpha_i(\lambda)}{\alpha_{Si-O\ stretching\ peak}(\lambda)} \times \frac{[C_i]}{[C_{Si-O\ stretching\ peak}]} \quad \cdots\cdots\cdots\cdots\cdots\cdots (4.5)$$

where i presents the band of i, and R_i is the ratio of the measured absorbance of i band to that of Si-O stretching band.

For the same bands in two SiOCH samples (e.g. sample 1 and sample 2), the ratio of R is:

$$\frac{R_1}{R_2} = \left(\frac{[C_1]}{[C_{Si-O\ stretching\ peak\ of\ sample\ 1}]} \right) \Big/ \left(\frac{[C_2]}{[C_{Si-O\ stretching\ peak\ of\ sample\ 2}]} \right) \quad \cdots\cdots\cdots\cdots\cdots\cdots (4.6)$$

Based on formula 4.6, the change of the band content in the samples can be compared by normalizing the peak height to that of Si-O stretching band at 1034 cm^{-1}, which has the strongest peak in the spectrum.

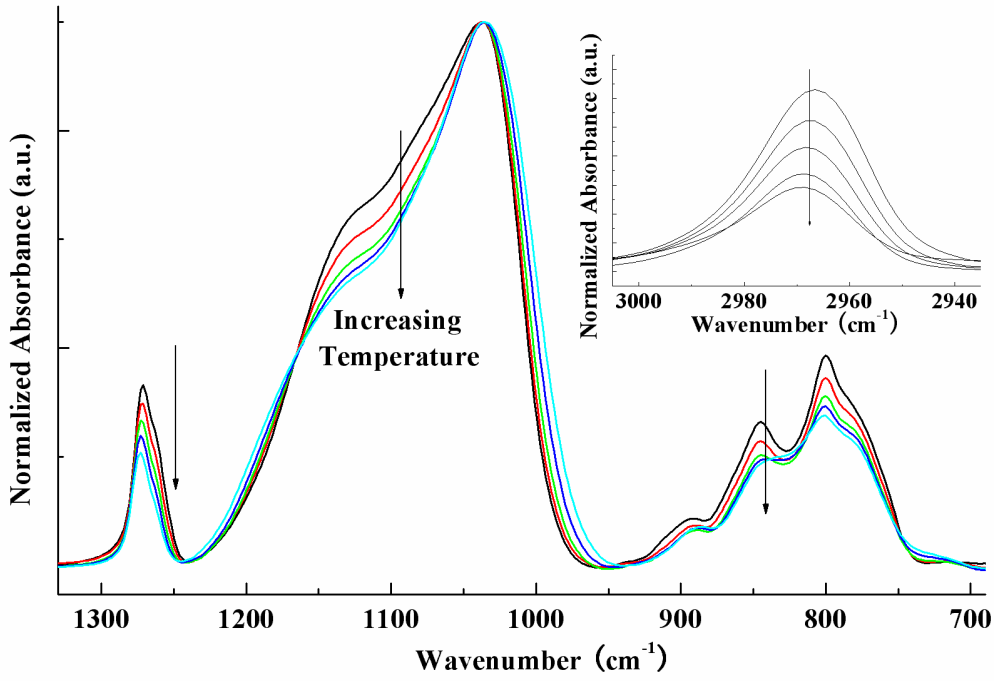

Fig. 4.5 FTIR spectra of SiOCH film prepared at different deposition temperatures

Fig. 4.5 shows the FTIR spectra of SiOCH film prepared at different deposition temperatures over a wavenumber range between 700 and 1330 cm^{-1}. The CH_m (m=1~3) stretching band from 2940 to 3000 cm^{-1} is also presented in the insert graph. The maximum intensity of each spectrum is normalized to 1.0. The label arrows in Fig. 4.5 represent a progressively low to high temperature variation. It is very clear that all the height ratios of other peaks to that of Si-O stretching bond decrease as the deposition temperature increases. Apparently at higher deposition temperature, the weaker $Si-CH_3$ and C-H bonds break leaving the films with a lower concentration of these bonds, and the SiOCH films become more similar to SiO_2.

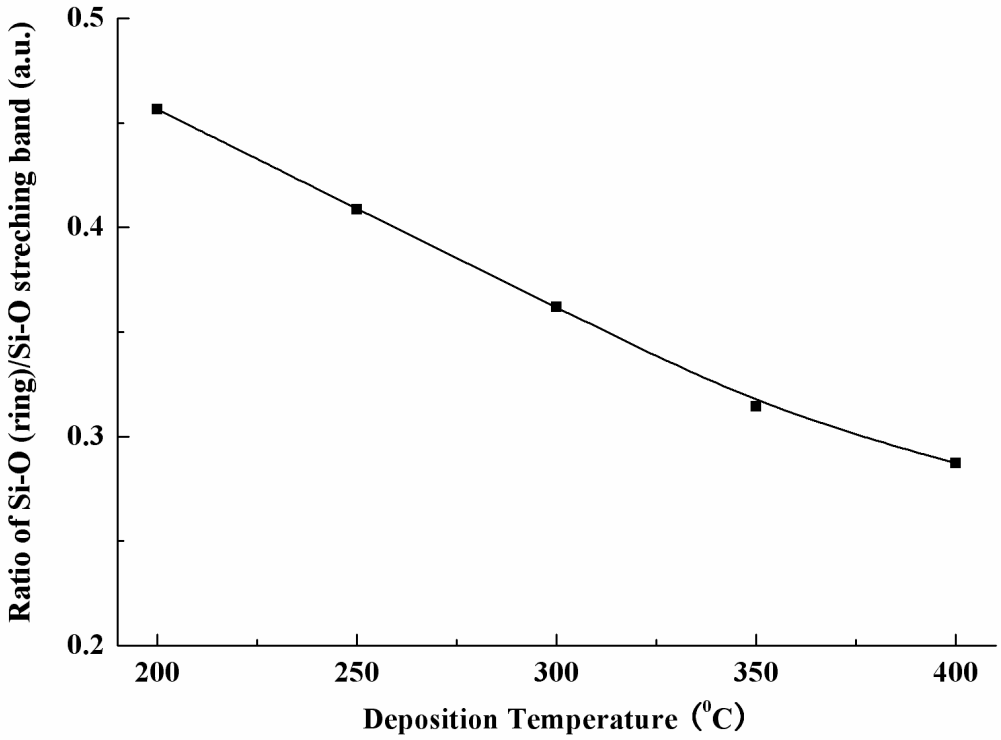

Fig. 4.6 Ratio of Si-O (ring) bonds/Si-O stretching band of SiOCH films deposited at different temperatures

In order to investigate the dependence of Si-O bond structure on the deposition condition deeply, each Si-O stretching band is deconvoluted into three bands, and the ratio of the area of Si-O ring band to that of whole Si-O stretching band is presented in Fig. 4.6. Obviously, more cage structure is incorporated in the film at lower deposition temperature, so the film density should be small. This is confirmed by the data of refractive index, dielectric constant, and hardness, which will be discussed in the later sections.

4.4.2 Deposition rate

Film thickness and refractive index (RI at 633 nm wavelength) are measured together by the 5240i Opti-Probe system. Each reading is taken at 49 points per wafer (as shown in Fig. 4.7) and averaged. Deposition rate is calculated from film thickness divided by deposition time.

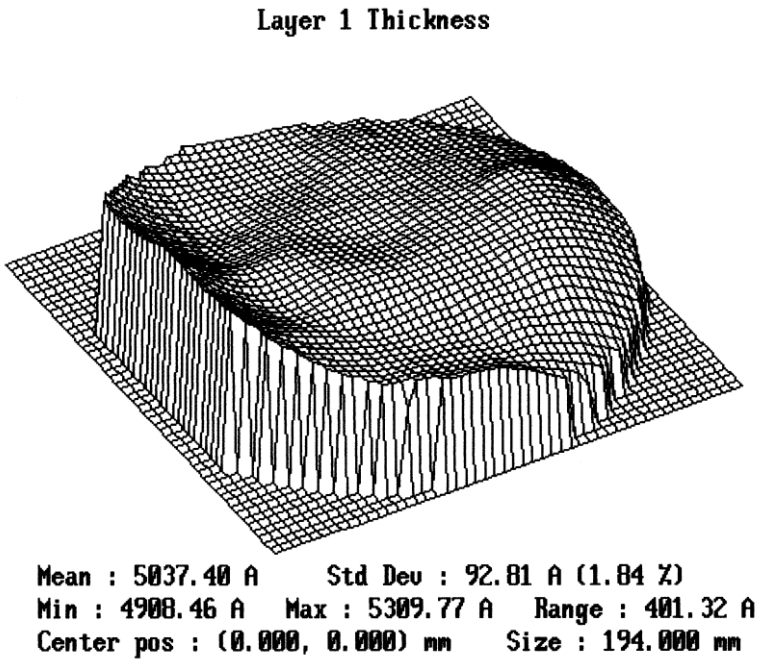

Fig. 4.7 3D map of thickness of SiOCH film

Figure 4.8 shows the deposition rate of SiOCH film as a function of temperature (^{0}C). Clearly, the deposition rate reduces as the deposition temperature increases. Such behavior is contrary to the typical thermally activated process which occurs in the formation of films such as SiO_2 or Si_3N_4. The apparently higher deposition rate at lower temperatures may be associated with the presence of voids within the films due to Si-CH_3 bonds [97], and such void structure of SiOCH films is shown in figure 2.6. This explanation is match with the observation of FTIR spectra with more Si-CH_3 and C-H bonds (shown in figure 4.5) and more Si-O (ring) bonds

(shown in figure 4.6) at lower deposition temperature. The variation of the deposition rate with the increase of deposition temperature follows a first-order exponential decay function very well. The apparent activation energy of such thermally "inactivated" process [97] is about –0.157ev, which is calculated using Arrhenius plot (shown in Fig. 4.9). The negative activation energy indicates that the deposition rate is controlled by surface absorption / desorption [98]. The activation energy of PE-(3MS+N_2O) SiOCH deposition was reported to be about -0.032 eV [98]. It means our PE-(3MS+O_2) SiOCH deposition process is more temperature sensitive than PE-(3MS+ N_2O).

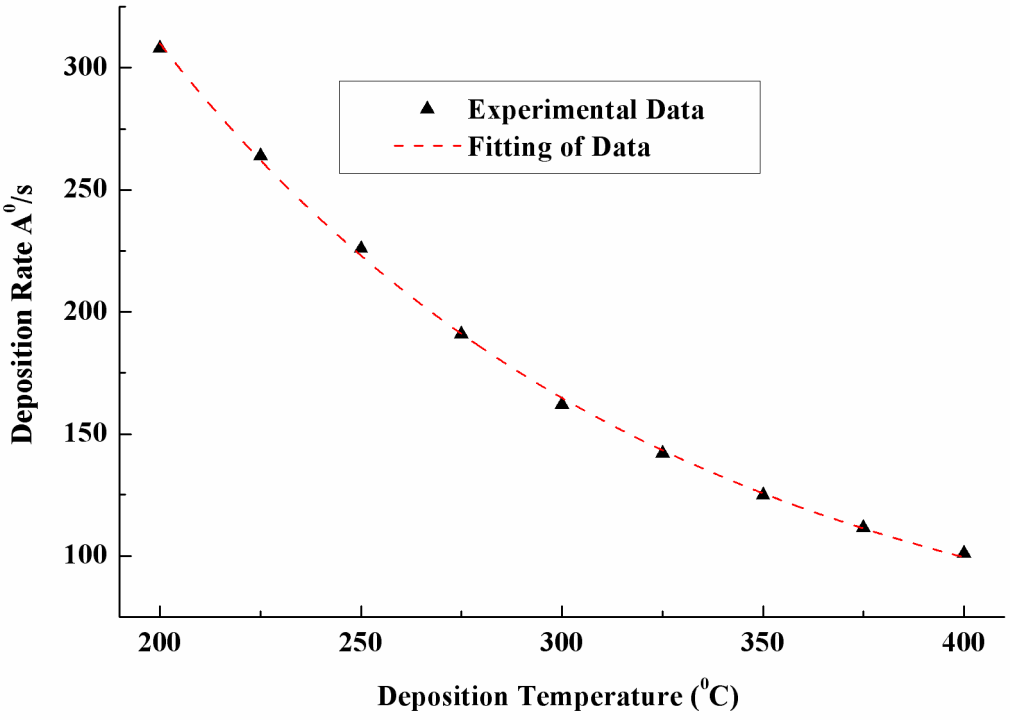

Fig. 4.8 Deposition rate of SiOCH film at different temperatures (^{0}C)

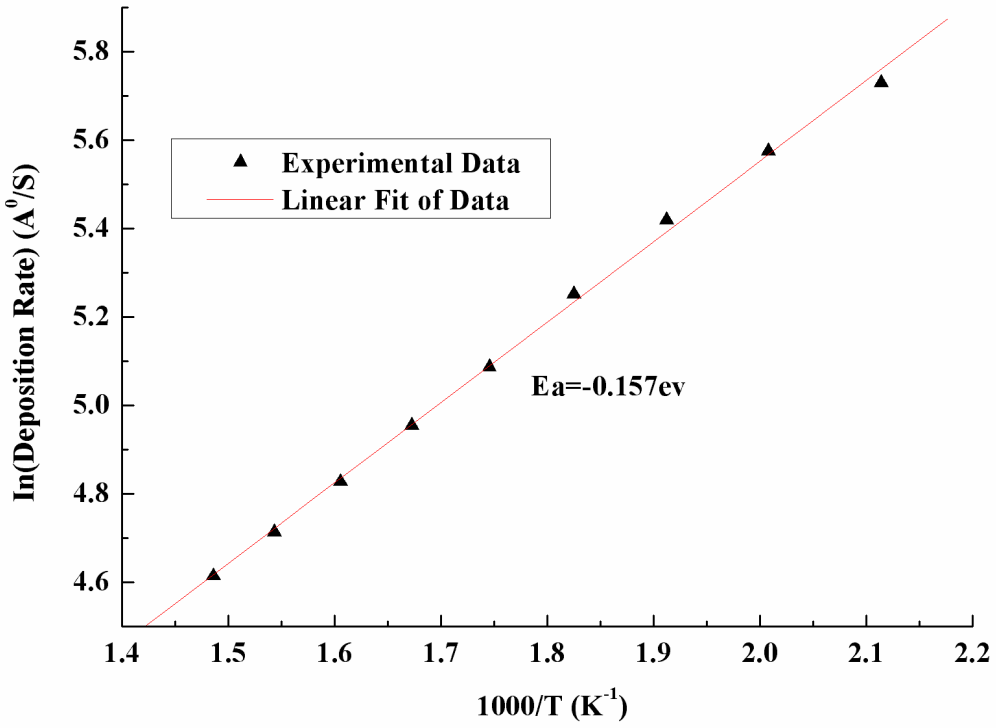

Fig. 4.9 Arrhenius plot of deposition rate vs absolute temperature (T)

It should be highlighted that all reaction rates generally increase with temperature, but Fig. 4.8 and Fig.4.9 show that higher deposition temperatures lead to lower film deposition rates in our chemical system, just as the case of deposition of GaAs [(99)]. This apparent paradox can be explained by considering the reversibility of chemical reactions [(99-100)]. The net reaction rate is the difference of the individual rates between forward reaction and reverse reaction. Each individual chemical reaction could be exothermic or endothermic reaction. For exothermic reaction, $\triangle H$ is negative, and the reactants have more energy than the products. On the contrary, the $\triangle H$ of endothermic reaction is positive, and the reactants have less energy than the products. Fig.4.10 shows an example of reversible chemical reaction with forward exothermic reaction and reverse endothermic reaction. If the activation energy barrier

(or slope) for the forward exothermic reaction get behind that for the reverse endothermic reaction, the net reaction rate will show negative activate energy, and decrease as the deposition temperature increases. Therefore, for PE-(3MS+O_2) SiOCH deposition process, it may contain forward exothermic reaction with lower activation energy barrier and reverse endothermic reaction with higher activation energy barrier. The net reaction rate increases monotonically with the decrease of temperature, and shows negative activation energy barrier. The film deposition rate will also increase monotonically with the decrease of temperature.

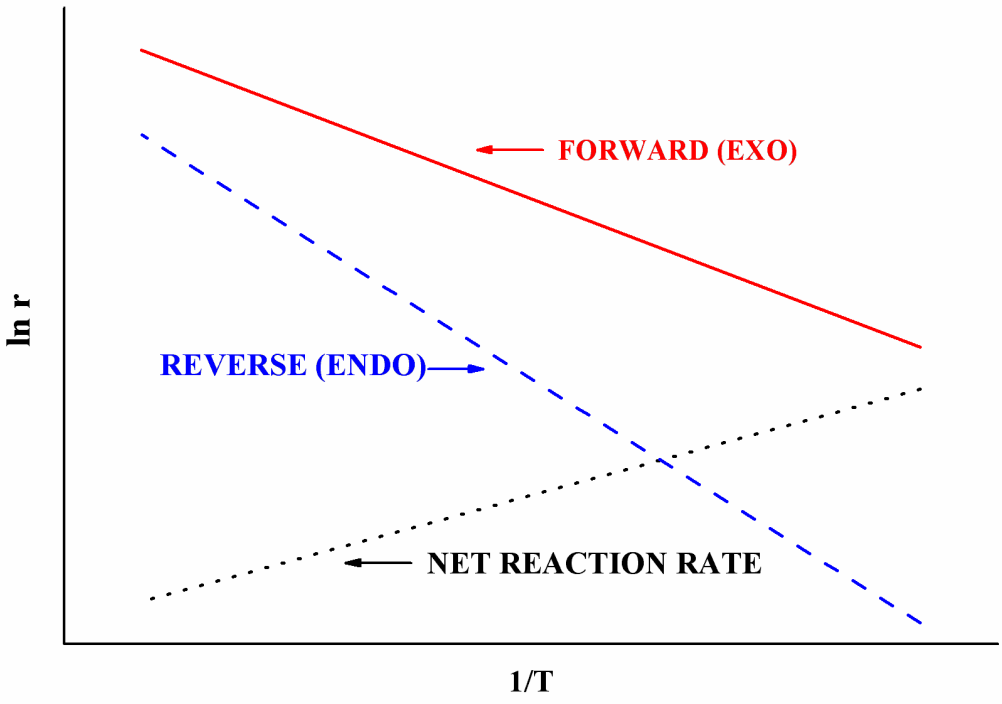

Fig. 4.10 Chemical Reaction energetics: Active energy for forward exothermic reaction is less than that for reverse endothermic reaction

4.4.3 Dielectric constant and refractive index

Generally the dielectric constant of ILD materials includes wafer in-plane (lateral) dielectric constant $k_{\parallel}$ and wafer out-of-plane (vertical) dielectric constant $k_{\perp}$. The directional dependence of dielectric constant relies on the structurally anisotropic properties of the dielectric materials. The typical reported dielectric constant k is wafer out-of-plane (vertical) dielectric constant, which obtained, usually at 1 MHz, by measuring the capacitance of a parallel-plate capacitor with know area, A, dielectric thickness, T, and the dielectric constant of free space ε_0, and given by following equation:

$$k = \frac{C \times T}{\varepsilon_0 \times A} \quad \text{..... (4.7)}$$

The capacitance area must be large so as to minimize the contribution of stray capacitance arising from perimeter fringing fields. The planar metal-insulate-silicon (MIS) capacitance is the typical measurement structure, which is fabricated on a P-type (boron doped) silicon substrate with resistivity ranging from 0.5 to 100 Ω-cm. Although the principle of the measurement is trivial, an accurate evaluation of dielectric constant requires not only an accurate value of the dielectric thickness, but also good contact to the wafer backside and deep accumulation status of silicon surface. If the latter two conditions are ignored, the dielectric constant may often be underestimated due to neglected series capacitance.

The dielectric constant is evaluated at 0.9216 MHz using an automatic mercury probe C-V measurement, SSM495, from Solid State Measurement Inc. The system uses mercury probe electrode to make a non-invasive electrical contact as it avoids the fabrication process of the pattern and etch to form aluminum electrode.

The mercury is kept inside a capillary and the contact area is maintained in constant, typically 0.2 X 10^{-2} cm^2 which must be calibrated before measurement every time. The bias voltage ranges from -250 V to +250V, but negative voltage bias should be carefully set up to ensure the P-type silicon surface remained in deep accumulation status to behave essentially as a grounded plate. A typical C-V measurement curve is shown in figure 4.11.

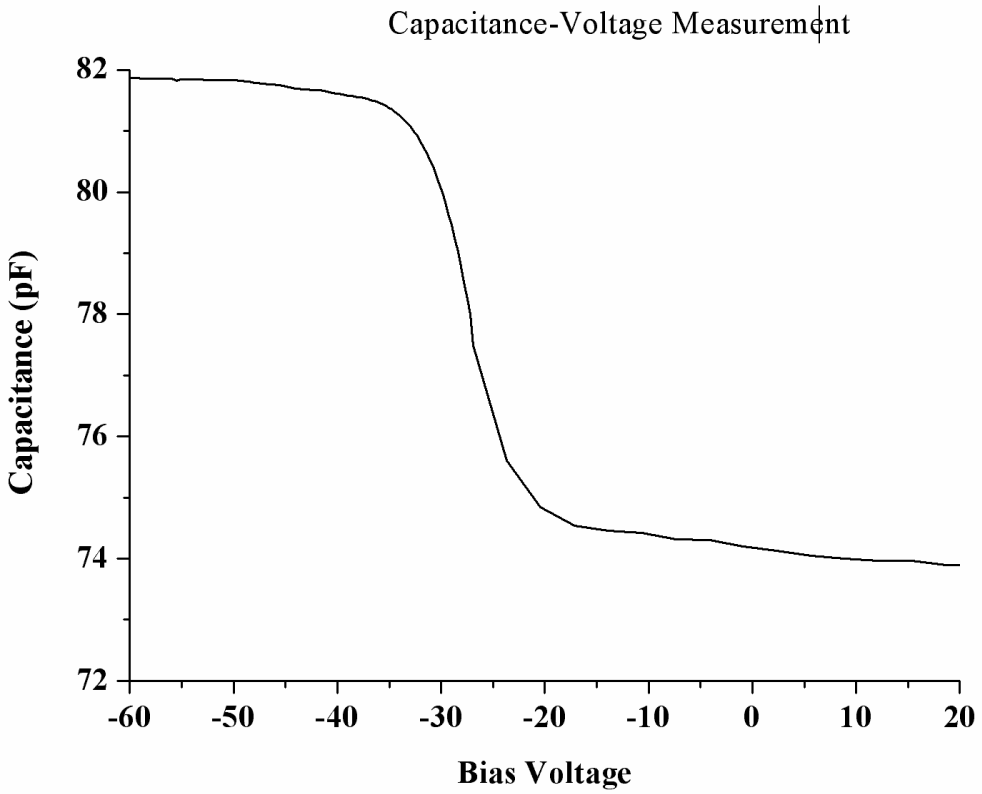

Fig. 4.11 Typical C-V measurement plot

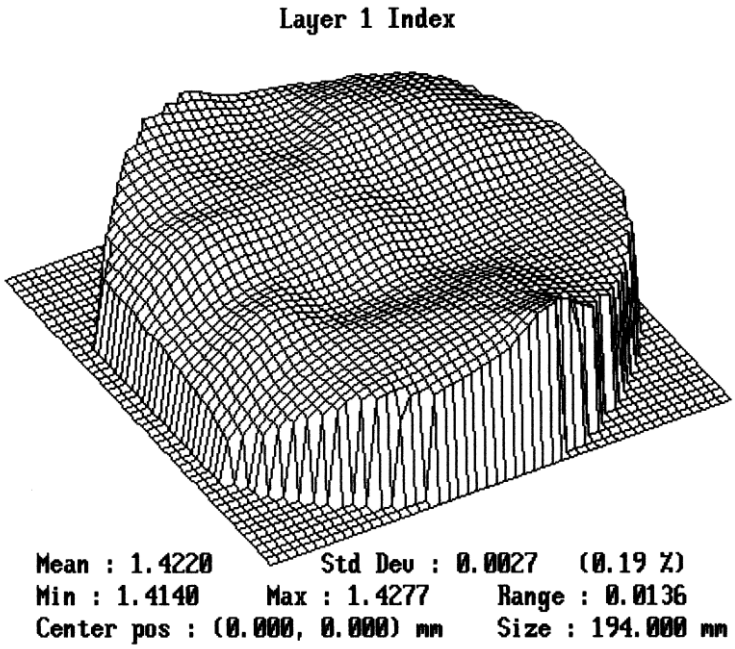

Fig. 4.12 3D map of Refractive index of SiOCH

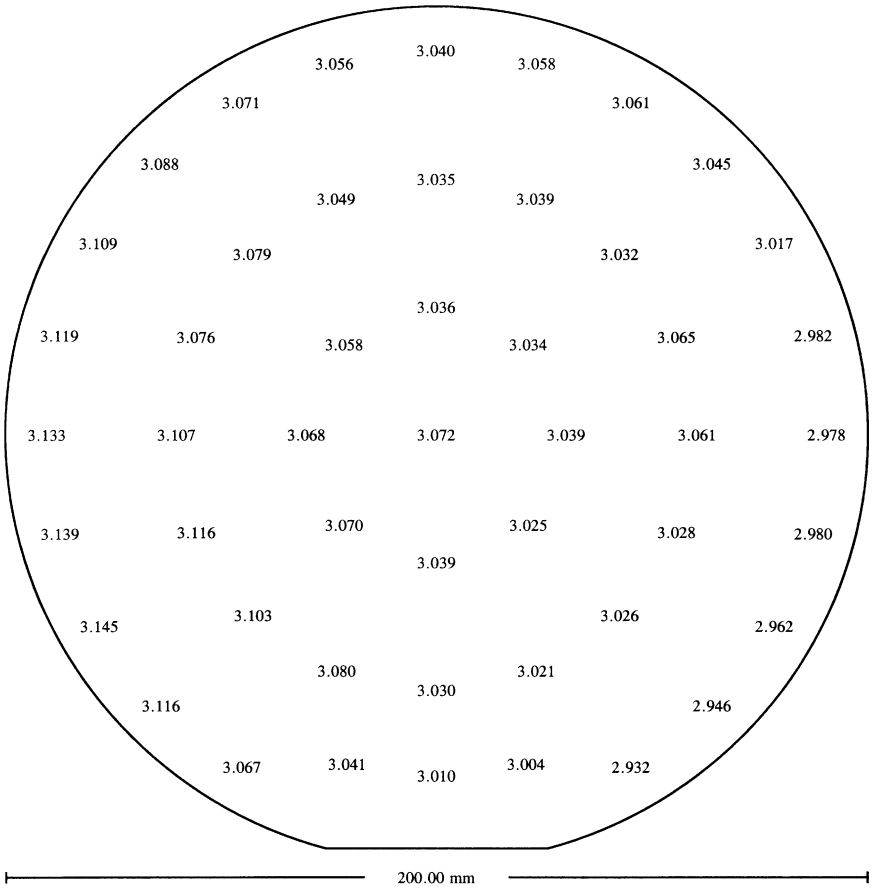

Fig. 4.13 Dielectric constant map of SiOCH

The refractive index is measured at 632.8 nm using ellipsometry, and the dielectric constant is obtained at frequency of 0.9216 MHz using conventional electrical capacitance in the accumulation region. Each reading is taken at 49 points per wafer (as shown in Fig. 4.12 and Fig. 4.13) and averaged.

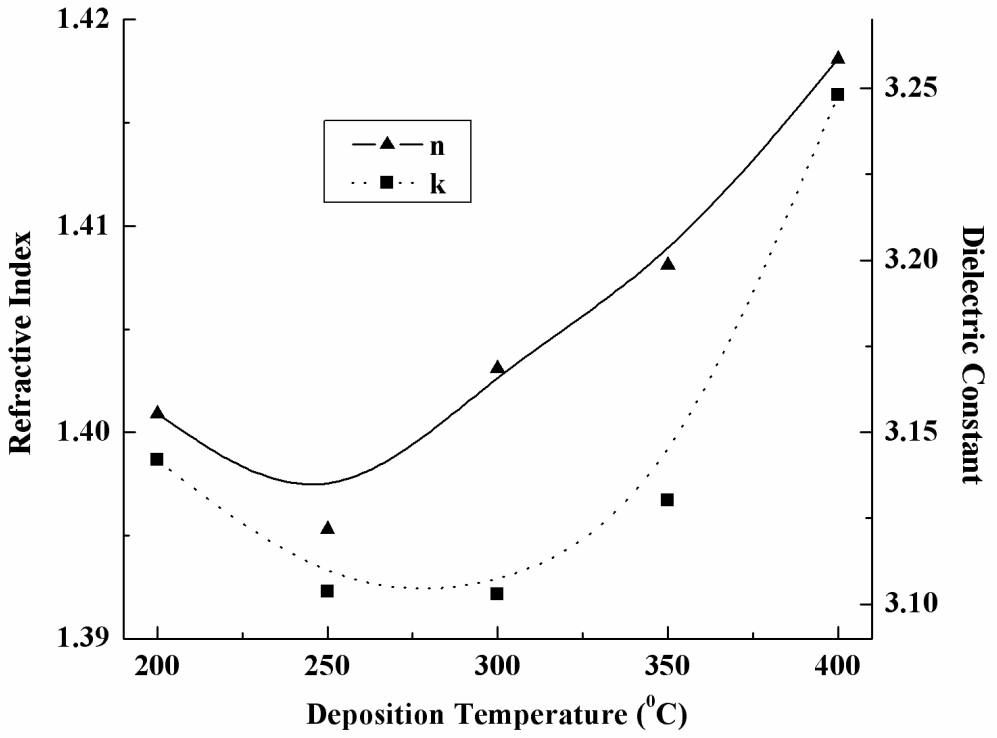

Fig. 4.14 Refractive index and dielectric constant of SiOCH films deposited at different temperatures

Figure 4.14 displays refractive index and dielectric constant of SiOCH films deposited at different temperatures. It can be found a trend that both the refractive index and dielectric constant increase slightly with deposition temperature. The observed dip in Figure 4.14 at 250 ^{0}C is formed by the abnormal higher values at 200 ^{0}C. Since the variation is so small, measurement errors or very little (thus undetectable) –OH bonds can result in abnormal higher values at 200 ^{0}C.

The variation trend of the refraction index can be understood in terms of the Lorenz-Lorentz (L-L) (or Clausius- Mossotti) formalism where two factors are considered: (1) changes in the density of the films; (2) differences among the polarizations of the bonds consisting of Si, O, C and H atoms. The L-L relationship is given by following equation [(101)] :

$$\frac{\varepsilon-1}{\varepsilon+2}=\frac{\rho}{3\varepsilon_0}(\sum_{i=1}^{k}N_i\alpha_i) \quad \text{.....(4.7)}$$

where ε is the dielectric constant, ε_0 is the permittivity of free space, ρ is the density of the SiOCH film, N_i is the number of bond i per cm^3, and α_i is the polarizability of bond i. In the visible optical range, extinction coefficient (k) can be neglected, and $\varepsilon=n^2$, where n is the refractive index. It should be clarified here that both ε and k represent the dielectric constant. Symbol ε is usually used in academic field, whereas symbol k often appears in engineering field.

As shown in Fig. 4.6, the concentration of cage structure will decrease when the deposition temperature increases, thus producing microporous structure in the film and a reducing film density. According to the above L-L relationship, lower density film is expected to demonstrate lower refractive index. In addition, it is easier to break weaker Si-CH_3 and C-H_m (m=1~3) bonds at higher deposition temperature, resulting in less content of Si-CH_3 and C-H_m (m=1~3) bonds in the film, which is presented in figure 4.5. This mechanism could further decrease the refractive index of the films, because the polarizations of carbon-related bonds are less than silicon or oxygen-related bonds. Therefore, figure 4.7 manifestes higher refractive index at higher deposition temperature. The variation of dielectric constant with deposition

temperature may also be ascribed to the change of content of Si-O cage structure, Si-CH_3 and C-H_m (m=1~3) bonds in the film.

4.4.4 Hardness and Young's modulus

As discussed in Chapter one, Cu/low-k interconnect system is needed to replace AL/SiO2 interconnect system in order to reduce RC delay, cross-talk and power dissipation for deep sub-micron integrated circuits. Copper has the potential to meet future requirements, especially with its low electrical resistivity and high resistance against electromigration. In 1997, Sematech announced that it had successfully deposited copper interconnectes onto silicon wafer. IBM, Motorola, Texas Instruments and VLSI Technology had all subsequently announced copper chip plans for higher speed, lower power consumption and lower manufactureing cost [(102)]. However, one of the technical issues to successfully integrate copper metallization into integrated circuits is that copper is not feasible for plasma to etch. To overcome this problem, single or dual damascene process is required to define the etching features through chemical mechanical planarization (CMP) process [(103)]. CMP process polishes the surface of the wafer so as to maintain depth of focus (DOF) for subsequent steps and ensure that the interconnects are not deformed over contour steps [(104)].

It is a challenge to develop a kind of low-k material that can withstand chemical mechanical polishing (CMP) without delaminating and cracking or fracturing, because many of the mechanical properties of low-k materials fall at least one order of magnitude lower than those of silicon dioxide. During the CMP process,

films experience high stress and any defect such as delaminating and cracking or fracturing can lead to yield and reliability issue. Hence, local mechanical properties of the films are critical parameters in process integration and should be thoroughly studied before low-k materials can be introduced into CMP process.

Besides CMP process, other process steps also require good mechanical properties for low-k materials. For example, when the low-k material is placed under stress by a film deposited on it at elevated temperatures, significant distortion can occur. If the processing temperature is higher than their T_g (glass transition temperature), materials are particularly vulnerable to distortion. Since the Young's modulus of most organic and inorganic low-k candidate materials is at least an order of magnitude lower than that of standard SiO_2 films prepared from TEOS (E ~ 59 GPa) [(105)], the mechanical reliability of these alternative dielectrics is an important integration concern.

The elastic modulus and hardness are the two major mechanical properties of the material. The elastic modulus of a material represents the relative stiffness of the material within the elastic range and can be determined from a stress-strain curve by calculating the ratio of stress to strain while hardness refers to resistance to bending, scratching, abrasion or cutting.

Nanoindenter with a Berkovich diamond tip pyramid-shaped is used to measure the hardness and Young's modulus of film. To avoid surface and substrate effects, the average hardness and Young's modulus are calculated using the load-displacement data with penetration depths between one tenth and one fifth of the film

thickness. Before each measurement, a standard sample, bulk silicon is used for calibration.

One of the cruelest tricks Mother Nature has played on us is that the mechanical strength and the dielectric constant appear to have a strictly inverse relationship. A low-k material film with a lower dielectric constant is usually accompanied with a weaker mechanical strength and vice versa. Density oxides will typically have hardness values of approximately 10 Gpa and elastic around moduli 70 Gpa [106], whereas the SiOCH low k films usually have hardness values between 0.13 and 1.7 Gpa and elastic moduli between 2.5 and 12.2 Gpa [107]. Our results shown in Fig. 15 agree with that of Ref. 19. It can be seen in Fig. 15 that, as the deposition temperature increases from 200^0C to 400^0C, hardness of the SiOCH film increases from 0.21 Gpa to 1.25 Gpa and elastic modulus rises from 2.4 Gpa to 12.5 Gpa.

Figure 4.15 shows the hardness and Young's modulus of SiOCH films deposited at different temperatures. The pattern in figure 4.15 is to be expected, because the samples deposited at higher temperature would be expected to be more rigid due to the increased crosslink and less film density. The hardness and modulus results shown in Fig. 15 can also be interpreted by analysing Si-CH_3 band between 1240 cm^{-1} to 1320 cm^{-1} of the FTIR spectrum [106]. The position of this band can vary with increasing oxidation that shifts the band to higher wavenumbers, based upon the degree of oxidation of the silicon atom [108]. According to the continuous random network theory and rigidity concept [109,110], the more degree of oxidation, the more rigid of the film. In Fig. 4.5, it can be found that the peak of the Si-CH_3 band between 1240 cm^{-1} to 1320 cm^{-1} of the FTIR spectrum shifts to higher wavenumber as the

deposition temperature increases, indicating more degree of oxidation. Such changes of micro-structure are reflected in the variation of hardness and modulus shown in Fig. 4.15.

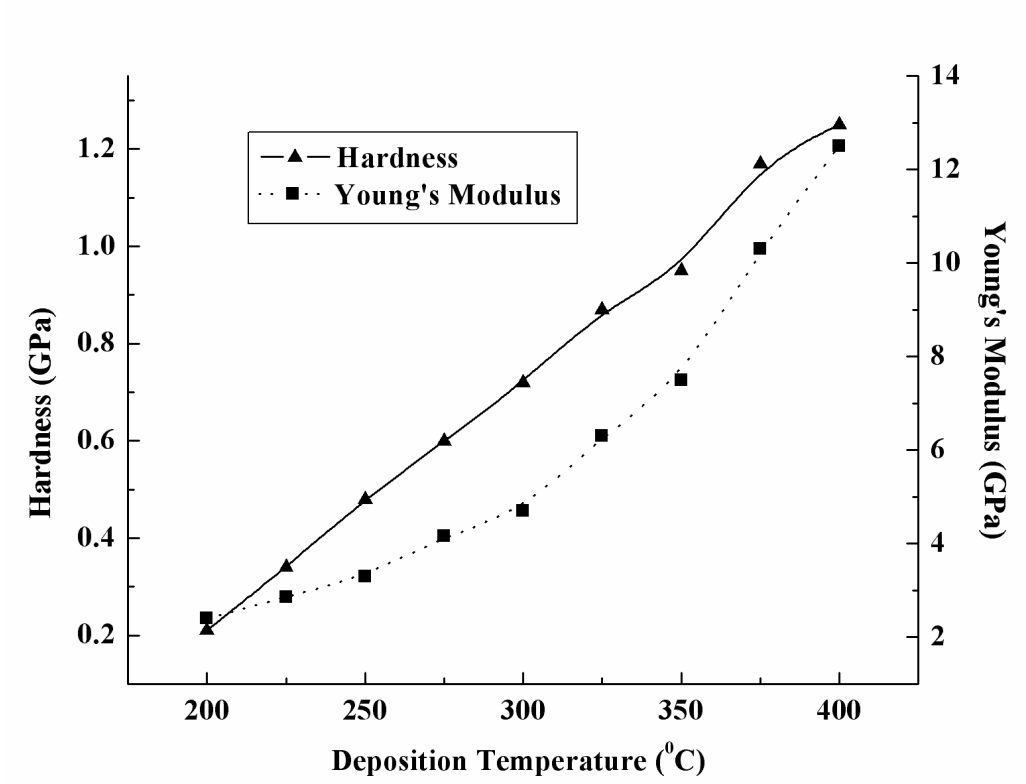

Fig. 4.15 Hardness and Young's modulus of SiOCH films deposited at different temperatures

4.4.5 Thermal Stability

Excellent thermal stability is required for low-k materials to withstand as many as 10~15 temperature excursions (~400-425^{0}C) in the fabrication of multilevel structures. Outgassing of volatile solvents or reaction/decomposition products can cause via poisoning, delamination, and blistering in the inter-level dielectric. Changes in the degree of crystallinity or crystalline phases lead to properties dependent on

thermal history. Thermal cycling also causes stresses in the interconnect structure due to the coefficient of thermal expansion mismatch between the ILD material and the metal or substrate. Such stresses may cause delamination if adhesion is poor. In the process of copper damascene interconnect which process temperatures are expected to be below 350^0C, the thermal stability requirements are expected to be lower than that in the aluminum case. However, the dielectric films must still be able to withstand the final alloy process which temperature typically reaches 400^0C. Therefore, it is important to investigate the thermal stability of the low k SiOCH films.

The SiOCH films deposited at 350^0C are used to study thermal stability. The as-deposited films are annealed for 30 minute at N_2 ambient with a gas flow rate of 1000 sccm and a pressure of 7.0 Torr in the system TEL ALPHA-8S-ZVFNS. The annealing is performed at temperatures of 450^0C, 500^0C, 600^0C, 700^0C, and 800^0C with ramping-up rate of 50°C/min and ramping-down rate of 9°C/min.

Fig. 4.16 shows the FTIR spectra of SiOCH films at different annealing temperatures. All the peak height of each spectrum is normalized to that of Si-O stretching band at 1034 cm^{-1}, which has the strongest peak in the spectrum. The label arrows in the figure represent the annealing temperature from low to high. The height of all carbon-related bonds almost remains no change at as high as 500^0C to 600^0C, but significantly decreases at above 700^0C and almost disappears after annealing at 800^0C. Z.-C. Wu et al. reported that Si–CH_3 bonds can be broken starting at 500 °C [111,112]. It was also reported that the FTIR spectra of silica-based materials showed almost no changes in Si–O peak shape when annealed at temperatures up to 500–600 °C [111 -116]. Our observation of SiOCH films also shows that the thermal energy

can break Si-CH_3, Si-C, Si-H and C-H bonds, and kick them off during annealing at high temperatures from 500 to 600°C. These terminating groups in SiOCH films play a waterblocking role [117-118], such that the films are normally hydrophobic. Once the terminating groups decrease after annealing at high temperature, the SiOCH film becomes more similar to SiO_2, and can easily absorb moisture (-OH bonds) which can be clearly seen at high wavenumber range of the FTIR spectrum as presented in

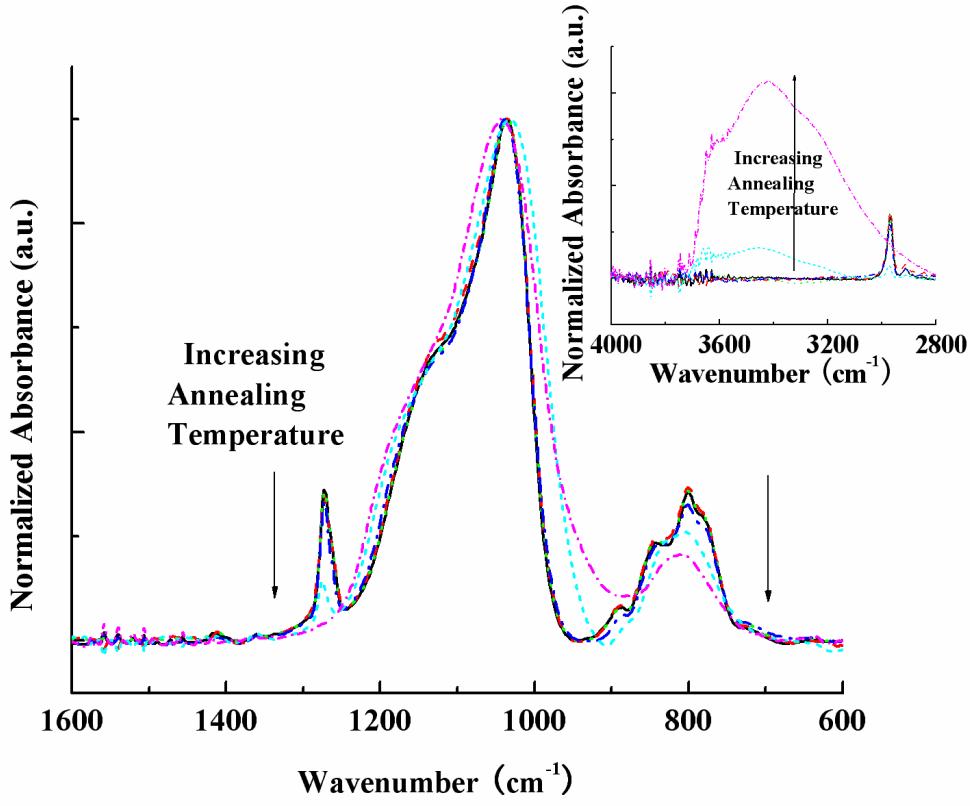

Fig. 4.16 FTIR spectra of SiOCH films at different annealing temperatures

the insert graph. In addition, the shoulder at wavenumber of about 1135 cm^{-1} remains almost no change at annealing temperature 600^0C, but becomes smaller after annealing at 700^0C, and almost disappears at annealing temperature 800^0C. Since such shoulder contains cage structure Si-O-Si which can produce a microporous

structure and a lower film density [96], the change of this shoulder indicates that microvoids in the films may be stable at 600^{0}C, but begin to collapse at 700^{0}C. It seems that the cage structure is not very stable and can be decomposed to the more stable silica network by high temperature thermal process.

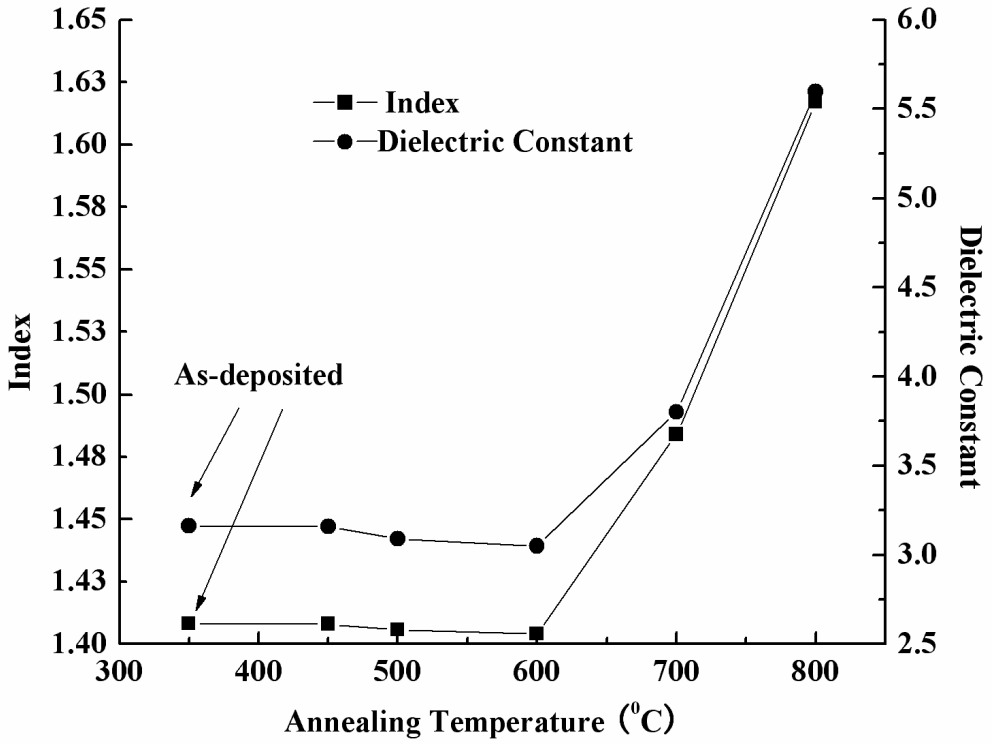

Fig. 4.17 Refractive Index of SiOCH films at different temperatures

Fig. 4.17 presented the annealing effect on index and dielectric constant of SiOCH films at different temperatures. The index and dielectric constant show the same trend as the annealing temperature increases. It reveals that both the index and the dielectric constant of the SiOCH films slightly decrease with annealing temperatures up to 600^{0}C. The obtained results can be considered in terms of some degree of thermal decomposition with dissociation methyl -CH_3 groups and low molecular weight components (e.g. C-H), which can be seen in FTIR results in

Fig.4.16. Such thermal decomposition increases the porosity of the film and results in a slight decrease of density and refractive index [(119)], and the dielectric constant slightly decreases due to lower electronic polarization and lower density. As the annealing temperature increases above 700^0C, the existing dangling bonds will re-bond and lead to an increase in cross-linking and density in the films. In addition, an increase in the number of Si–O bonds relative to Si(–CH_3)m bonds will enable the film to uptake moisture, which can be seen in the FTIR in Fig. 4.16. These lead to higher refractive index and dielectric constant.

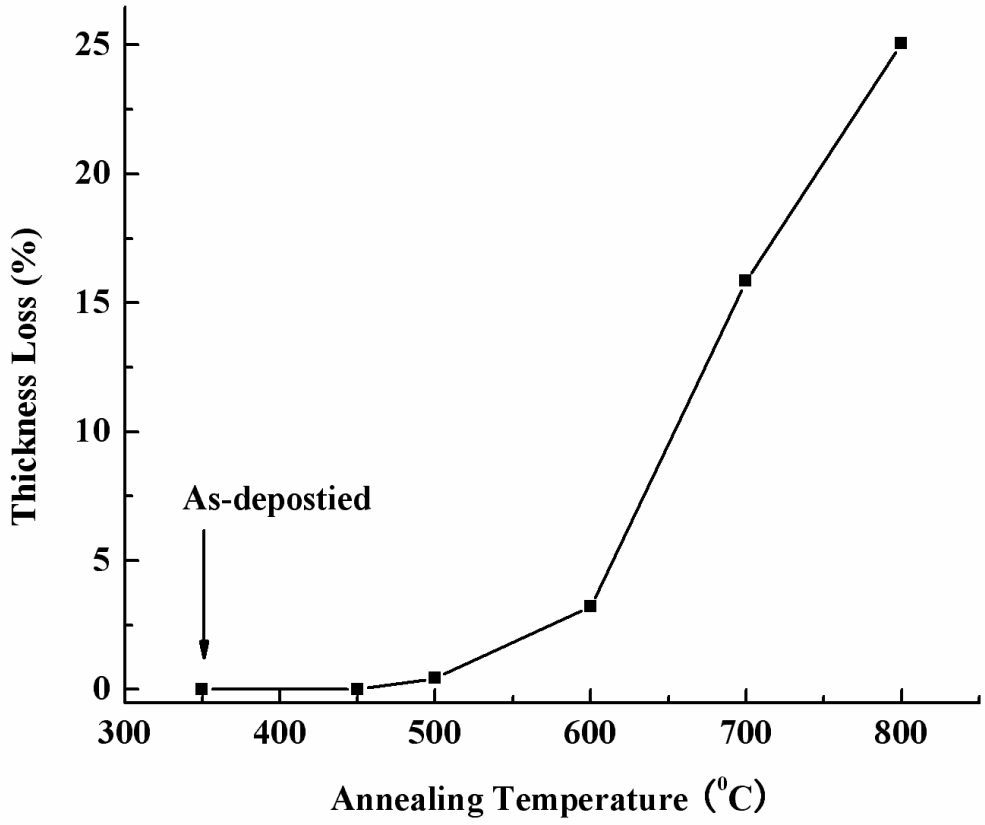

Fig. 4.18 Thickness loss of SiOCH films after annealing at different temperatures

The thickness loss after annealing at different temperatures for SiOCH films is showed in Fig.4.18. There is almost no thickness loss after annealing below 600^0C for 30 minutes, but the films have shrunk for about 16% and 28% in thickness after annealing for 30 minutes at 700^0C and 800^0C, respectively. The shrinkage in thickness can be ascribed to the loss of carbon and hydrogen due to significant thermal decomposition and densification due to a collapse of microvoids in the films when annealing at high temperature.

4.5 Summary

PECVD SiOCH low-k thin films are deposited using trimethylsilane (3MS) and oxygen mixtures at different deposition temperatures. The influence of deposition temperature on the properties of SiOCH films is investigated. The results indicate that lower refractive index and dielectric constant could be obtained at lower deposition temperature, but the mechanical properties become poorer due to less degree oxidation and incorporation of more CH3 bonds and Si–O cage structure into the film. The deposition rate follows a first exponential decay function with the temperature (^{0}C), which has apparent activation energy of -0.157 eV.

The thermal stability of PECVD SiOCH films deposited at 350^0C from trimethylsilane and oxygen with O_2 /3MS flow ratio of 100/600 sccm has been also studied. All the results of FTIR spectra, thickness loss and refractive index suggest that the film is thermally stable at as high temperature as 500^0C, which exceeds the highest temperature (400–450 ^{0}C) encountered during typical interconnect processing

steps. When the annealing temperature increases above 600^0C, thermal energy can significantly break Si-CH_3, Si-C, Si-H, and C-H bonds, which results in change of composition, shrinkage of thickness, and increase of dielectric constant.

Chapter 5

Effect of Gas Flow Rate and RF Power on Properties of PECVD SiOCH Low k Films

5.1 Introduction

The properties of films deposited with plasma-assisted CVD will be affected by the deposition variables such as deposition temperature, gas composition, flow rate, total pressure, reactant partial pressure, pumping speed, RF power density, frequency, electrode materials, electrode spacing and reactor geometry. Optimization and carefully control of these process parameters are necessary to meet the requirement of low k materials.

In chapter 4, control of the deposition temperature has been shown to be effective in tuning the properties of PECVD SiOCH low k films. In this chapter, variations in the details of SiOCH film properties will be delineated with changes in other deposition conditions: gas flow rate and RF power.

5.2 Experiments

All the SiOCH films are deposited on p-type (100) orientation bare 8-inch silicon wafer in the PECVD chamber using 3MS-O_2 as precursors. The films are prepared at different O_2 gas flow rates ranging from 30 to 700 sccm with 3MS gas flow rate of 600 sccm, RF power of 600 W, total pressure of 4 Torr, and substrate

temperature of 350^{0}C. The films are also deposited at different RF power ranging from 400 to 800 W with other conditions remained constant: O_2/3MS gas flow rate is 100/600 sccm, total pressure in chamber is 4 Torr, and substrate temperature is 350^{0}C. Then, the prepared films are studied how the deposition condition in gas flow rate and RF power affects the SiOCH film properties in terms of FTIR spectra, index of refraction (RI), dielectric constant, deposition rate, surface energy, surface roughness, hardness and Young's Modulus.

5.3 Result and Discussion

5.3.1 Effect of O_2 gas flow rate

5.3.1.1 FTIR Spectra Analysis

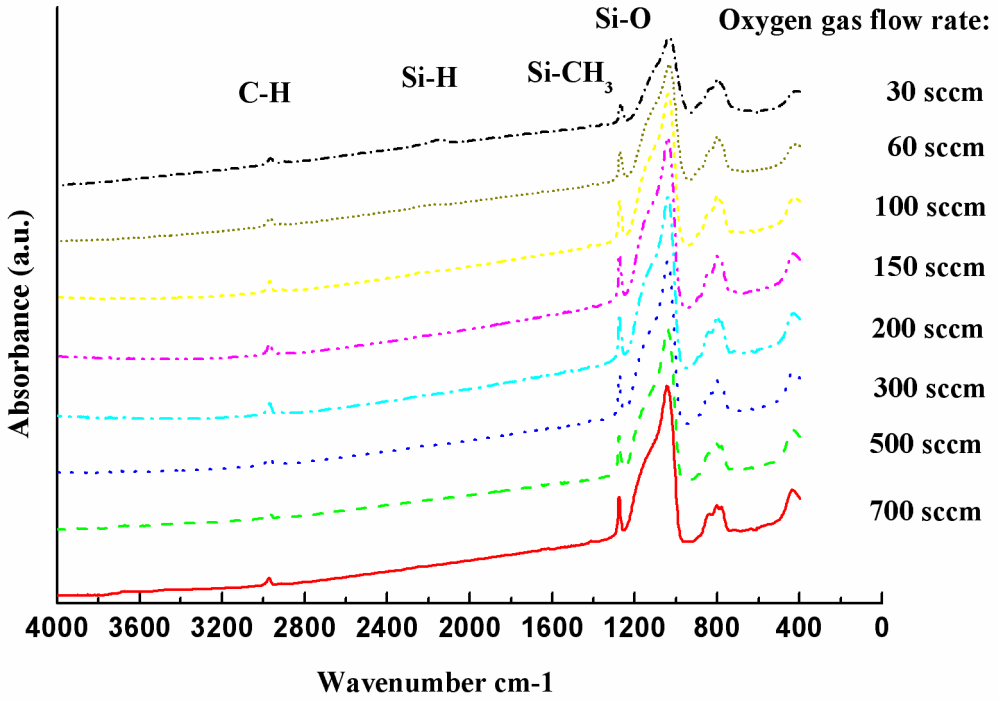

Fig. 5.1 FTIR absorption spectra of SiOCH films at different oxygen gas flow rates

The experimental data on the vibrational states as studied using FTIR is shown in Figure 5.1 for the as-deposited SiOCH films at different oxygen gas flow rates. The absorption bands are assigned as in Section 4.4.1 of Chapter 4. All the films exhibit the same bond structure, except that the absorption band of CH_m (m=1~3) stretching modes at about 2890 to 2990 cm^{-1} disappears as the oxygen gas flow rate increases above 150 sccm. Every spectrum presents the characteristic absorption band of SiOCH with a sharp peak at about 1273 cm^{-1}, corresponding to stretching vibration modes of $Si\text{-}CH_3$. Stretching Si-O band is the strongest band centered at about 1038 cm^{-1} in each spectrum. The area of the two main absorption bands, $Si\text{-}CH_3$ stretching band and stretching Si-O band, can be used to estimate the carbon content in the films. Although the area ratio of the two bands may not give the accurate carbon content quantitatively, it could still be used as an indicator to study the effects of gas flow rate. The relative concentration of carbon incorporated in SiOCH composite films is calculated by the following equation normalized to the peak area of the Si–O stretch band:

$$\text{Relative carbon content (\%)} = \{A_C /(A_O+A_C)\}X100 \quad \text{----------(5.1)}$$

where A_C and A_O are the band areas of $Si–CH_3$ stretching vibration mode at 1273 cm^{-1} and the Si–O stretching vibration mode at 1038 cm^{-1}, respectively. From Figure 5.2, the relative carbon content is found to decrease monotonously from 3.8% to 2.7% as the oxygen gas flow rate increases from 30 to 700 sccm with keeping the 3MS gas flow rate constant. More oxygen can result in a decrease of methyl groups and Si-C bonds. It is possible because that selective oxidation of Si-C is the mechanism of oxygen atoms incorporated into the PECVD SiOCH films [(120)].

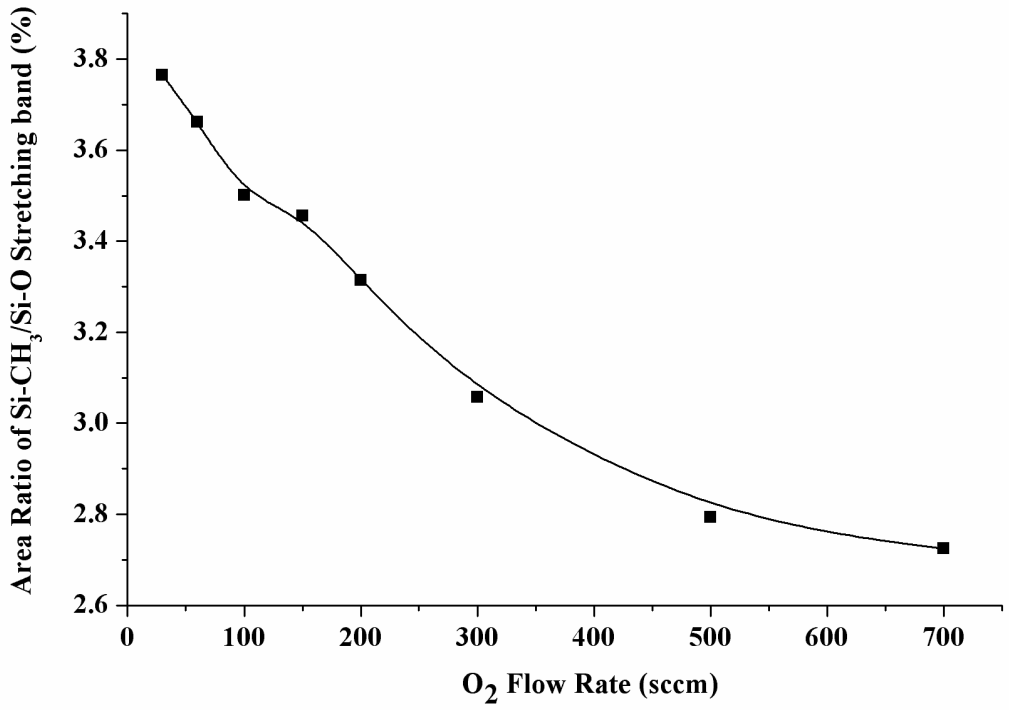

Fig. 5.2 The integrated absorption area ratio of Si-CH_3/Si-O stretching band at different O_2 gas flow rates

The FTIR spectra in Figure 5.1 also presents that variation of the oxygen gas flow rate could affect the position of the absorption peaks. Figure 5.3 shows the wave-number of the absorption peak of Si-O stretching vibration modes. As the oxygen gas flow rate increases from 30 sccm to 700 sccm, the frequency of the Si-O stretching peak at about 1034 cm^{-1} shifts slightly from about 1031.6 cm^{-1} to higher frequency 1042.2 cm^{-1} (blue-shift). These frequency shifts in FTIR spectra indicates the change of the bonding characteristics, such as bond angle and bond length. According to the central force model for the vibrational properties [121,122], the frequency of the Si–O stretching vibration mode in amorphous SiO_2 can be approximated by an expression of the form:

$$\nu^2 = (k/m_0)[\sin^2(\theta/2)] \quad \text{----------(5.2)}$$

where k is a nearest-neighbor effective force constant, which is presumed to vary inversely with the Si–O bond length r_0, m_0 is the mass of an oxygen atom, and θ is the Si–O–Si bond angle, assumed to be 144° in amorphous SiO_2 [123,124]. The expression 5.2 neglects the relative motion of the silicon atoms. If the Si–O bond length r_0 is assumed to be unchanged with incorporation of carbon to amorphous SiO_2, the expression 5.2 could be simply expressed as the following equation [125]:

$$\nu = \nu_0 \sin(\theta/2) \quad \text{----------(5.3)}$$

where ν_0=1135.6 cm^{-1}, which is experimentally obtained for ν =1080 cm^{-1} in thermally grown SiO_2 films. Based on the above equation, the observed blueshift as O_2 gas flow rate increases (shown in Fig. 5.3) imply that the Si-O-Si bond angles increase with increasing O_2 gas flow rate.

The carbon doped in the silicon dioxide matrix could account for the frequency shift of the Si-O stretching peak shown in Fig. 5.3. Y. H. Kim *et al.* [125] reported that more carbon atom could result in redshift of the Si-O stretching peak in the SiOC film. The same correlation is found in Fig. 5.2 and Fig.5.3. As the oxygen gas flow rate increases, carbon content decreases in Fig. 5.2 and the frequency shift of the Si-O stretching peak increases. It suggests less carbon will result in blueshift of the Si-O stretching peak.

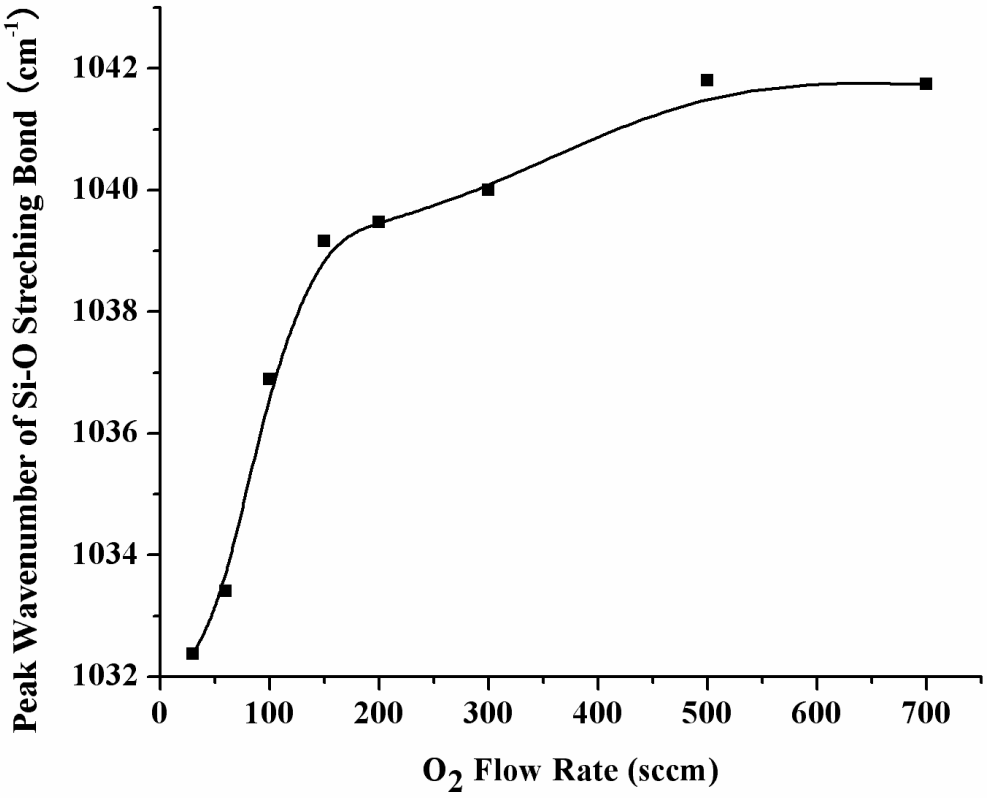

Fig. 5.3 Frequency of Si-O stretching bond in SiOCH as a function of O_2 gas flow rates

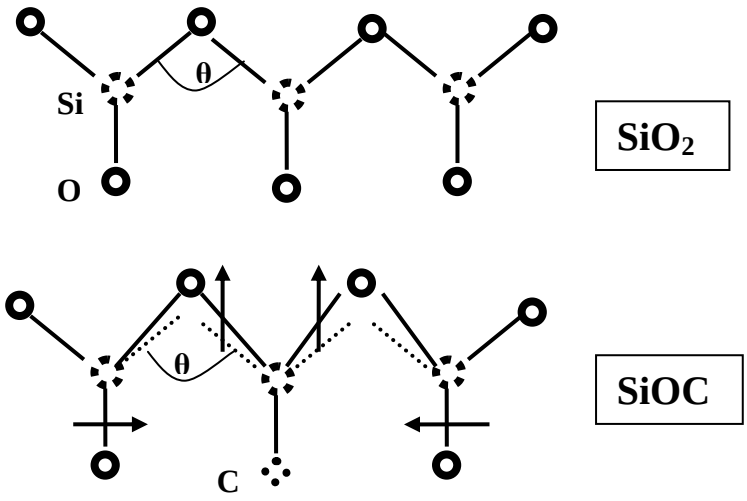

Fig. 5.4 Change of bond angle of Si-O bonds in SiOC films

The correlation between the additive carbon concentration and the frequency shifts of the Si-O stretching bond in FTIR spectra of SiOCH films could be described with the bonding structure model based on the electronegativity of an atom [125,126]. Fig.5.4 presents the bond angle of a two-dimensional model for SiO_4 and SiO_3C tetrahedral structures. Since all the four outer electrons of silicon atom in the SiO_4 tetrahedral structure are bound by the same atoms (oxygen), all the repulsive force strength between bonding electrons pairs are equal, thus resulting in same bond angle of "O-Si-O". However, the repulsive force strength between bonding electron pairs of the adjacent oxygen atoms in the SiO_3C tetrahedral structure is smaller than that in the SiO_4 tetrahedral structure because electronegativity of carbon atom (~2.5) is lower than that of oxygen atom (~3.5) [127], so the bond angle of "O-Si-O" in the SiO_3C tetrahedral structure is smaller than that in the SiO_4 tetrahedral structure if we assume the "Si-O" bond length is not changed by Si-C bond. Therefore, increase of carbon content in the SiOC film should result in redshift of the Si-O stretching peak. This is verified by the results shown in Fig. 5.3, which indicates that the carbon concentration increased but the position of the Si-O stretching peak shifts to lower frequency as oxygen gas flow rate decreases.

It should be highlighted that as the oxygen gas flow rate increases, the carbon content almost lineally decreases (shown in figure 5.2), but the frequency of Si-O stretching peak increases not in lineal mode. It increases much faster in the range of 30 to 150 sccm than in the range of 150 to 700 sccm of oxygen gas flow rate (shown in figure 5.3). Therefore, besides carbon content, there should be other mechanism to involve in the frequency shift of the Si-O stretching peak.

The bond-stretching frequency is usually expected to increase with increase in film density in a material that is considered to be three dimensional in its local bonding structure [128]. Lucovsky *et al.* [123] reported that an increase of film density could lead to redshift of Si-O stretching peak. According to their microscopic model, the Si-Si distance would decrease when the film density increase because the Si-O bond length is essentially unchanged, thus leading to the decrease of the Si-O-Si bond angle which produced redshift of the Si-O stretching bond. Since denser film is expected to possess larger refractive index (n), increase of refractive index should accompany with redshift of Si-O stretching peak. In the other word, less refractive index should result in blueshift of Si-O stretching peak. This is demonstrated by the results shown in figure 5.2, figure 5.3 and figure 5.5. As oxygen gas flow rate increases from 30 to 150 sccm, carbon content in figure 5.2 decreases and causes the frequency of the Si-O stretching peak to shift to higher side, and the significant decrease of refractive index in figure 5.5 further increases the frequency of the Si-O stretching peak. But as oxygen gas flow rate increase from 150 sccm to 7000 sccm, refractive index in figure 5.5 almost no change thus no contribution of the frequency shift of Si-O stretching peak, and only the continuous decrease of carbon content in figure 5.2 plays the role to increase the frequency of Si-O stretching peak. The two mechanisms that cause frequency shift of the Si-O stretching peak overlap each other and give the pattern shown figure 5.3.

5.3.1.2 Dielectric Constant and Refractive index

Figure 5.5 shows the dielectric constant and refractive index of SiOCH films as a function of O_2 gas flow rates. The refractive index of SiOCH films ranges from

1.395 to 1.438, which is less than those of amorphous silicon carbide (about 2) and amorphous silicon dioxide (about 1.45). The dielectric constant of SiOCH films ranges from 3.1 to 3.65, which is less than those of amorphous silicon carbide (about 7) and amorphous silicon dioxide (about 3.9). Since the atomic structure of the films is identified as a mixture of a dominant and totally amorphous SiO_2-like phase with a partially polycrystalline SiC phase [129], the lower dielectric constant and lower refractive index than those of the two main components in the films could be ascribed to the presence of microvoids in the films, which is closely related to the incorporation of CH_3 moieties into the films from the organosilicon precursor 3MS [130] . S.-K. JangJean et. al. also reported [131] that the SiOCH film is the form of amorphous SiOC:H compound with a lot of open volume and ‘‘imperfect’’ Si-O–Si sp3 tetrahedral bonds terminated by CH_3 and/or H, plus some loose, unsaturated methyl groups (CHx) trapped in the open cores of the structure. The microvoids can decrease the density of the SiOCH films, and the methyl groups (CHx) in the films can lower the polarizations of the bonds, therefore the dielectric constant and refractive index of SiOCH films are lower than those of the two main components in the films, the amorphous SiC and amorphous SiO_2.

The refractive index decreases sharply from 1.435 to 1.395 with increasing O_2/3MS flow ratio from 30/600 sccm to 150/600 sccm. This may be attributed to the decrease in the volume fraction of silicon carbide compared to silicon dioxide in the films. Indeed, if the precursors are short of oxidant, amorphous SiC:H with higher refractive index can be obtained on the PECVD using 3MS [132,133]. The variation of the film density can also explain the change of the refractive index. Using low-angle specular x-ray reflectivity (XRR) technique, It was reported [129] that the electron

density of SiOCH films decreased as the 3MS/O_2 flow rate decreased from 800/100 to 400/100 sccm. This variation of 3MS/O_2 gas flow rate is similar as O_2/3MS flow rate change from 75/600 sccm to 150/600 sccm in term of ratio of gas flow ratio in Fig. 5.5. Since the hydrogen influence on the effective mass density can be ignored [129,134], the effective mass density is proportional to the electron density. Therefore we could conclude that as the O_2/3MS flow rate changes from 75/600 to 150/600 sccm, the decrease of the effective mass density (electron density) result in the decrease of the refractive index. However, no obvious change of the refractive index can be found as O_2/3MS flow rate changes above 150/600 sccm. It needs further study on the properties (such as film density) of the SiOCH films deposited at this range.

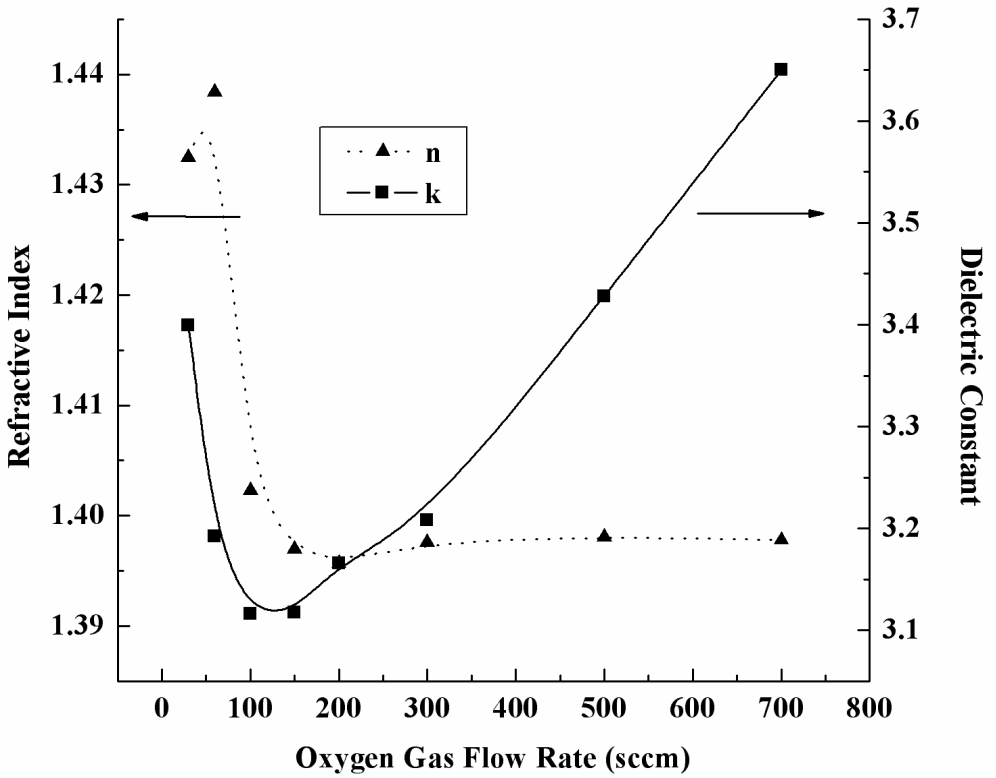

Fig. 5.5 Dielectric constant and refractive index of SiOCH films as a function of O_2 gas flow rates

As the O_2/3MS flow rate increases from 30/600 sccm to 150/600 sccm, the dielectric constant decreases in the same trend as the refractive index. It may be due to decrease of volume fraction of SiC phase and density. However, the dielectric constant began to increase significant when O_2/3MS flow rate increased above 150/600 sccm. The lowest dielectric constant 3.1 is observed for the films deposited at about 100/600 to 150/600 sccm. The increase of dielectric constant at higher oxygen gas flow rates may be due to the replacement of Si-CH_3 bonds with Si-O bonds, as can be seen from the FIIR spectra in figure 5.1 and the Si-CH_3 in figure 5.2.

5.3.1.3 Deposition Rate, Surface Morphology and Roughness

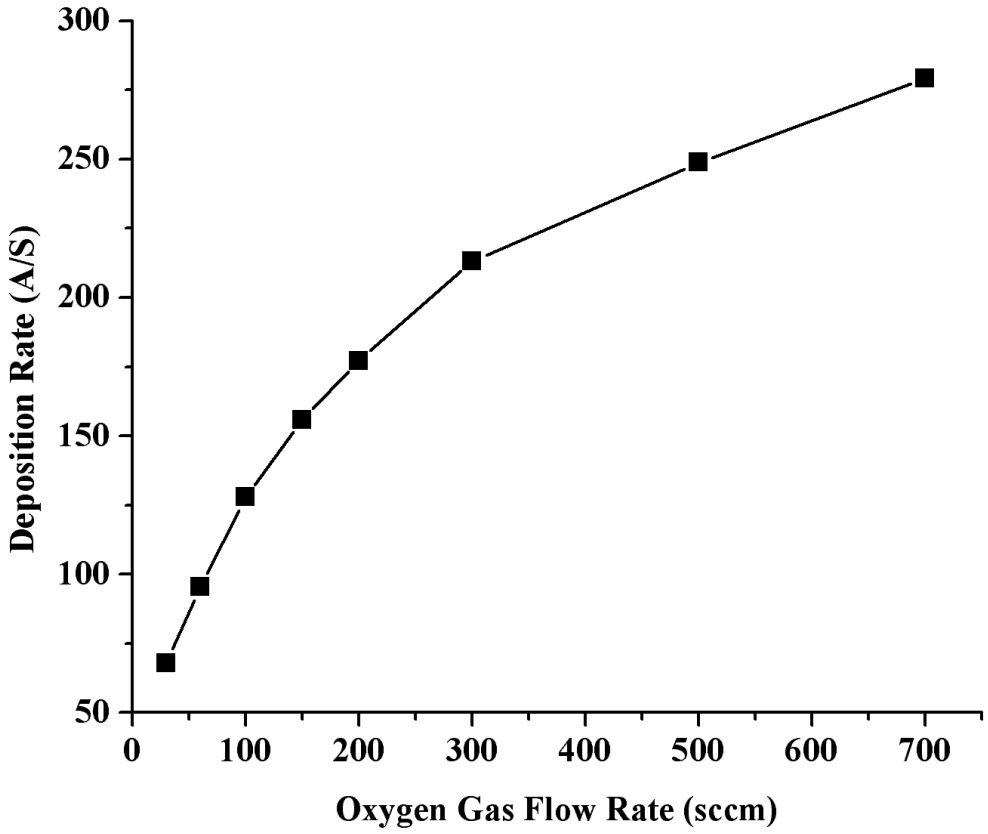

Fig. 5.6 Deposition rate of SiOCH films as a function of O_2 gas flow rates

Film deposition rates of PECVD 3MS/O2 are measured as a function of oxygen gas flow rates with fixed 3MS gas flow rate. As shown in figure 5.6, the deposition rate increases with the oxygen gas flow rate, suggesting that the dissociation of 3MS is enhanced by oxygen. It increases much faster at lower O_2 gas flow rate than at higher O_2 gas flow rate, which suggests there should be a maximum deposition rate if the O_2 gas flow rate further increases. L.M. Han et. al. [135] observed highest deposition rate of SiOCH films using N_2O/4MS as precursors when they increased the oxidant N_2O gas flow rate. The PECVD process is surface-reaction-limited [136], and the film deposition rate has a complicated dependence on reactivated reactant concentration on the substrate surface. The Si-O bonds of the SiOCH films were formed from the selection oxidation of Si-C bonds by oxygen radicals [137]. In figure 5.6 at higher oxygen concentrations, the surface may be nearly saturated with adsorbed oxygen and further oxidation with Si-C radicals decomposed from 3MS may be blocked. Similar surface reaction behavior was also observed in SiO_2 deposition process with silence-oxygen reaction [138,139].

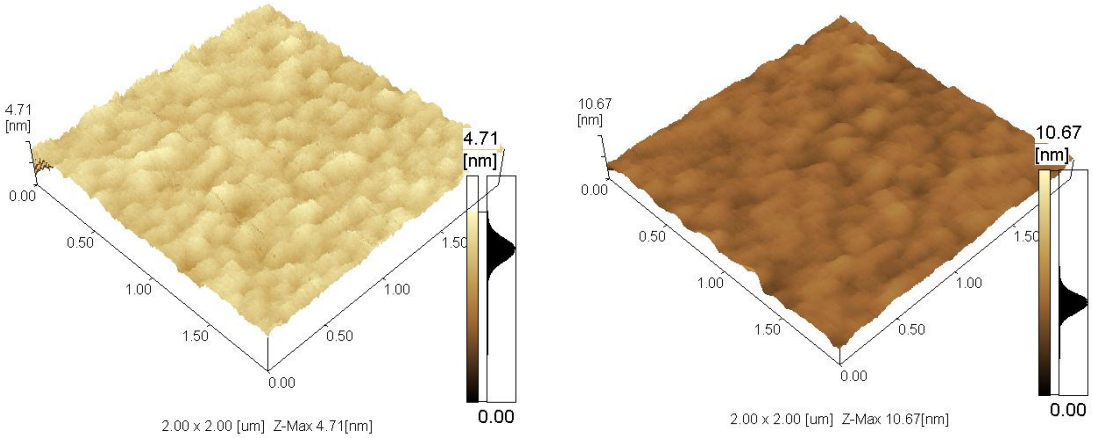

Fig. 5.7 AFM images of SiOCH films deposited at O_2 flow rate of 30 sccm (left) and 700 sccm (right)

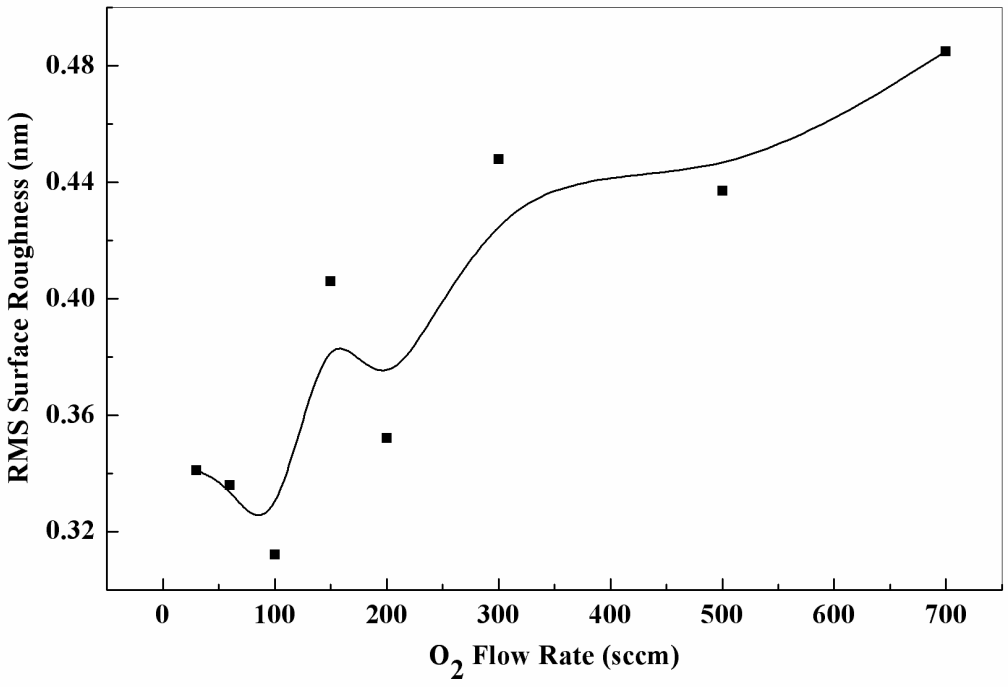

Fig. 5.8 Surface roughness of SiOCH films deposited at different O_2 flow rates

The surface morphology and roughness of SiOCH films are of concern for its application as interlayer dielectric, and are characterized on the SHIMADZU SPM 9500 atomic-force microscope (AFM). Figure 5.7 shows the AMF images of the surface morphology of SiOCH films within area of 2um X 2um. Different vertical scales are used due to different roughness among samples. The film deposited at 700 sccm O_2 flow rate is much rougher than the film deposited at 60 sccm O_2 flow rate. The root-mean-square (RMS) roughness value of surface within the area of 2 um X 2 um of SiOCH films ranges from 0.32 nm to 0.48 nm, and increases with the increase of oxygen flow rate as illustrated in figure 5.8. The higher roughness can be ascribed to the higher deposition rate at higher O_2 flow rate. However, all the samples are quite smooth because the RMS surface roughness is less than 0.5 nm for all the films in thickness of about 500 nm.

5.3.1.4 Hardness and Young's Modulus

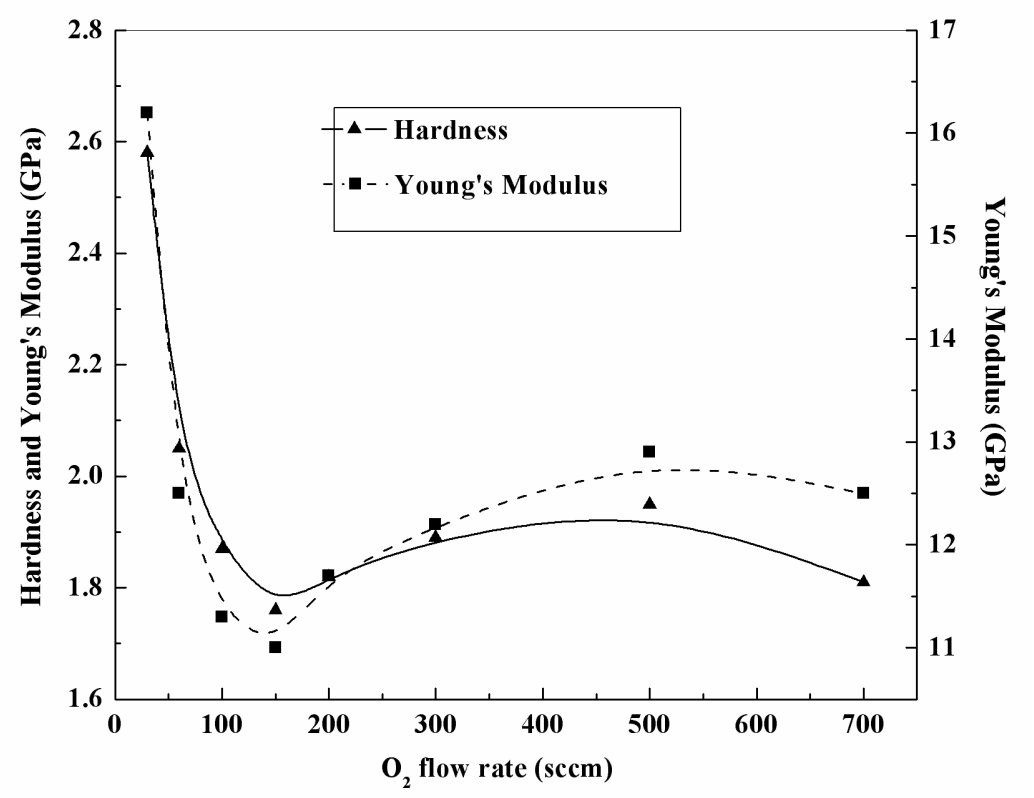

Fig. 5.9 Hardness and Young's Modulus for the SiOCH films as a function of O_2 flow rates

Both the hardness and Young's Modulus for the SiOCH films as a function of oxygen flow rates are illustrated in figure 5.9. It can be seen that the hardness decreases from the highest value 2.58 GPa to lowest value 1.76 GPa as the oxygen gas flow rate increases from 30 to 150 sccm, then it rises slightly and maintains at about 1.9 GPa as the oxygen gas flow rate further increases from 150 to 700 sccm. The dependence of the Young's Modulus on oxygen gas flow rate is similar to that of the hardness. Both the hardness and Young's Modulus strongly depend on the density of the material. The higher the density of the material is, the higher the hardness and Young's modulus. This is confirmed by the refractive index in Fig. 5.5 which

illustrates the same trend as the hardness and Young's modulus when the oxygen gas flow rate changes.

5.3.1.5 Surface Energy

The dielectric constant of SiOCH films is reduced through the introduction of CH_m bonds or porosity. Both of CH_m bonds or porosity may deteriorate the mechanical properties, such as hardness, Young's modulus, adhension, wetting behavior. The successful implement of SiOCH low k films needs detailed characterization of these mechanical properties.

Adhesion between two materials occur owing to a physical bonding attributed to Van Der Waal's forces and chemical bonding across the interface between the two materials. It is the chemical bonding that is strong and provides stability (or adhesion) when subjected to forces of thermal or mechanical nature. In order to be successfully integrated into multilevel interconnect structure, a low k candidate material must have adequate adhesion to both the underlying material and the films deposited on them. Delamination during fabrication or operation can occur if the adhesion between adjacent layers is poor. Interfacial adhesion in Copper/low-*k* interconnects is a critical issue. Good correlation between fracture toughness and CMP survival rate was found after evaluation of the adhesion of SiOCH, spin-on polymers, and spin-on glasses to Ta, TaN, and TiN barrier layers [140,141]. Poorly adhering layers can also provide low mechanical resistance channels for lateral metal extrusion growth. They also provide channels for corrosion if metallic residue and moisture are left or trapped in or between the films.

Some wetting steps, such as wet cleaning and wet stripping, may involve in the process integration of SiOCH low k inter-layer dielectric (ILD) material. Trapped moisture in ILD films can cause a variety of problems, such as increase of dielectric constant, enhancement of metal corrosion, delamination of overlying film, and via poisoning. Via poisoning can occur even when relatively small amounts of moisture are present [(142)]. Moisture outgassing from vias can oxidize the metals used for multilevel interconnect during deposition steps, thus forming high resistive material and poor step coverage and even causing via open failure. Absorbed moisture can also reduce the interfacial bonding strength between a low dielectric constant material and a metal [(143)].

The adhesion property, wetting behavior, and control quality in process of cleaning and coating of thin films could be evaluated with analysis of surface energy by contact angle measurement [(144-147)]. Young had developed famous Young's equation to first link the contact angle with the surface free energy of liquid and solid surface when a drop of liquid lies on the solid surface as following [(144)]:

$$\gamma_{sv} = \gamma_{sl} + \gamma_{lv}\cos\theta \text{ ----------(5.4)}$$

where γ_{sl} denotes the solid/liquid interfacial energy, θ refers to the contact angle, and γ_{sv} and γ_{lv} represent the solid and liquid surface energy respectively. Surface energy is composed of both specific (polar) and non-specific (dispersive or non-polar) forces. The sum of these forces is equal to the total surface energy. In equation 5.4, contact angle θ and liquid surface energy γ_{lv} are measurable parameters, and the solid/liquid interfacial energy γ_{sl} can be described by the harmonic-mean method as a function of liquid and solid surface energy (γ_{lv} and γ_{sv}) [(148)]:

$$\gamma_{sl} = \gamma_{sv} + \gamma_{lv} - 4\left(\frac{\gamma_{sv}^{d}\gamma_{lv}^{d}}{\gamma_{sv}^{d}+\gamma_{lv}^{d}} + \frac{\gamma_{sv}^{p}\gamma_{lv}^{p}}{\gamma_{sv}^{p}+\gamma_{lv}^{p}}\right) \text{----------(5.5)}$$

where the superscripts *d* and *p* indicate the dispersion (non-polar) and polar components of the surface energy respectively, and the sum of them is the total surface energy. Equation 5.4 and equation 5.5 are independent from each other, and from them it can be derived:

$$(1+\cos\theta)\left(\gamma_{lv}^{d}+\gamma_{lv}^{p}\right) = 4\left(\frac{\gamma_{sv}^{d}\gamma_{lv}^{d}}{\gamma_{sv}^{d}+\gamma_{lv}^{d}} + \frac{\gamma_{sv}^{p}\gamma_{lv}^{p}}{\gamma_{sv}^{p}+\gamma_{lv}^{p}}\right) \text{----------(5.6)}$$

Since the contact angle θ is measurable parameter, if two kinds of liquid with known values of γ_{lv}^{d} and γ_{lv}^{p} are used, solution of two simultaneous equations (5.6) can give the dispersive and polar components (γ_{sv}^{d} and γ_{sv}^{p}), and the total solid surface energy is the sum of them: $\gamma_{sv} = \gamma_{sv}^{d} + \gamma_{sv}^{p}$.

Table 5.1 The total surface energy γ_{lv} with dispersive γ_{lv}^{d} and polar γ_{lv}^{p} components of selected liquid for measurement

Liquid Name	Dispersive (dyne/cm)	Polar (dyne/cm)	Total (dyne/cm)
Water	22.10	50.70	72.8
Methylene iodide	48.50	2.30	50.8
Formamide	39.50	18.70	58.2

In order to make the measurement as accurate as possible, three kinds of liquid, water, methylene iodide and formamide, are used in our work. Table 5.1 lists their surface energy γ_{lv} with dispersive γ_{lv}^{d} and polar γ_{lv}^{p} components. Since each couple of liquid can give one independent solution for equation 5.6, three groups of

value of surface energy could be obtained for each sample after testing with three types of liquid, and the average surface energy from the three groups of value may provide more accurate evaluation of the film properties.

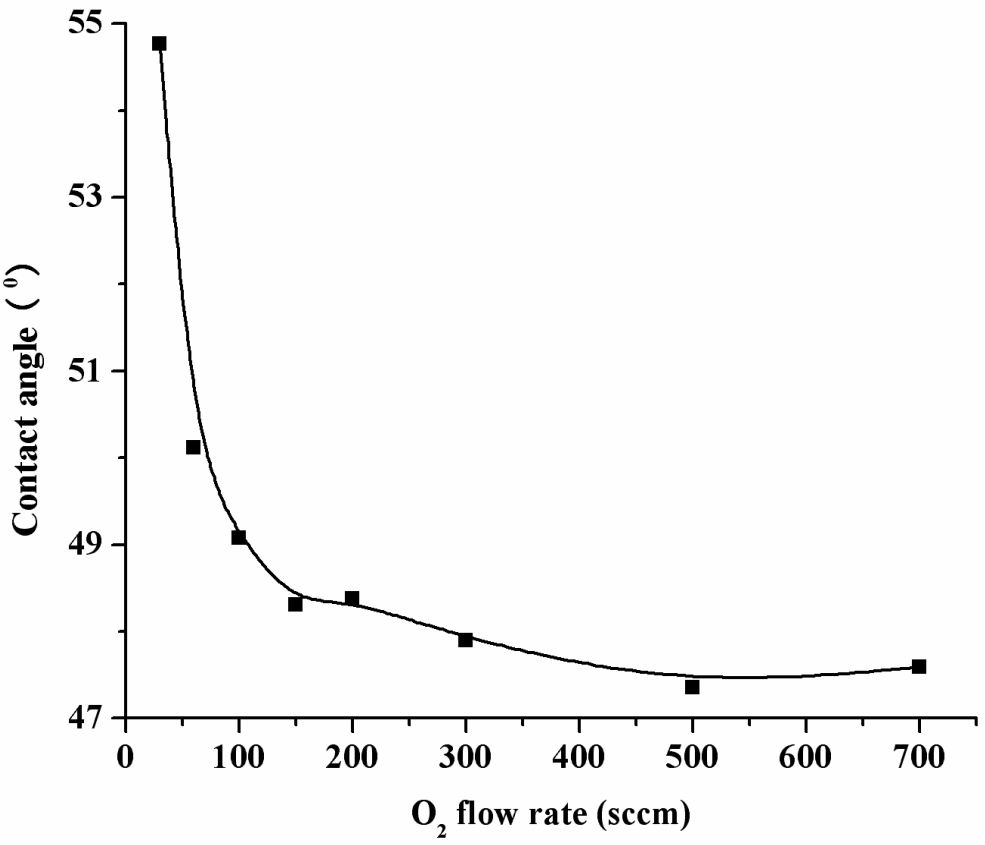

Fig. 5.10 Contact angle of water with SiOCH films deposited at different O_2 gas flow rates

The variation of oxygen gas flow rate can affect the contact angle of deposited SiOCH films with water. As can be found in figure 5.10, the contact angle of water with SiOCH film monotonously decreases from 54.8 to 47.6 as the oxygen flow rate increases 30 sccm to 700 sccm. The variation of contact angle is more dramatic at lower oxygen flow rate than that of higher oxygen flow rate. This may due to the decease of carbon content on the surface of the SiOCH film as the oxygen flow rate increase, which is confirmed indirectly by the FTIR result in Fig. 5.1 and Fig. 5.2.

The contact angle can be used to quantify the wettability of a solid surface. Generally, the contact angle is less than 70 for a hydrophilic surface, whereas it is 70 or above for hydrophobic surface [(149)]. Figure 5.10 indicates all the SiOCH films have hydrophilic surface but become more hydrophobic (waterproofing) at lower oxygen flow rates.

The surface roughness can affect the contact angle. The relationship between surface roughness and contact angle can be described by Wenzel's equation [(150)]:

$$\gamma(\gamma_{sv} - \gamma_{sl}) = \gamma_{lv} \cos\theta_w \quad \text{----------(5.7)}$$

where γ is a roughness factor, defined as the ratio of the real and apparent surface areas, and θ_w is the contact angle for a rough surface. Comparing the trend of contact angle in figure 5.10 with the roughness in figure 5.8, especially in higher oxygen flow rates, it is hardly to find the correlation between the contact angle and roughness. This may be due to that the roughness is so smooth that the roughness factor may approximately be one, and the roughness effect on the contact angle could be negligible.

Figure 5.11 shows the total surface energy including dispersive and polar components of SiOCH films as a function of oxygen flow rates. In the lower oxygen flow rate, variation is observed for the total surface energy and its dispersive and polar components, but they almost stable on a certain value in the higher oxygen flow rate. As the oxygen flow rate increases from 30 sccm to 150 sccm, the total surface energy and its polar component increase from 52.5 to 56 dyne/cm and from 20.8 to 26 dyne/cm, respectively. In contrast, the dispersive component of the surface energy

decreases from 31.6 to 30 dyne/cm. The increase of polar component determines the increase of total surface energy.

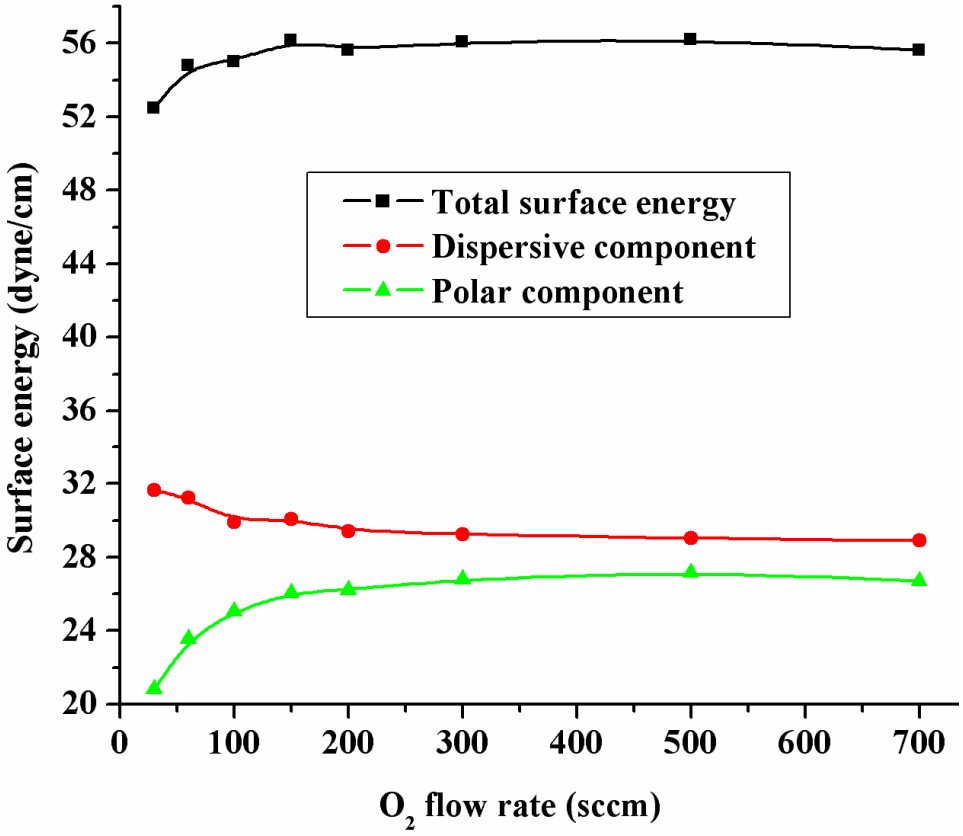

Fig. 5.11 Surface energy with dispersive and polar components of SiOCH films deposited at different O_2 gas flow rates

Surface energy arises from the unbalance of the force between atoms or molecules inside and interface. Its dispersive component of the surface energy comes from the interaction of instantaneous dipoles, whereas its polar component is due to hydrogen bonding and the interaction of two permanent dipoles or permanent dipolar-induced dipolar. The dispersion force interaction is dependent upon the sixth power of the distance separating the two species. The distance must be close together for the

potential energy of interaction to have any effect. So the density of the film might affect the dispersive component of the surface energy. The reduction of dispersive component in figure 5.9 may due to the reduction of the film density, which can be indicated by the variation of refractive index in figure 5.5. The increase of polar component of surface energy might result from the hydrogen bonding provided by the oxygen atom or the dandling bond induced by the oxygen plasma as the oxygen flow rate increase. It will be helpful to analyze the surface energy if more detail change of elemental distributions and the chemical compositions on the surface of the films are determined by X-ray photoelectron spectroscopy (XPS).

5.3.2 Effect of power

Thickness and refractive index (n) of the film are measured at 632.8 nm on Opti-Probe 5000 (Therma-Wave, Inc.). Figure 5.12 shows the variation of SiOCH film deposition rate as a function of RF power. It can be found that the deposition rate increases linearly as the RF power increases. This behavior could be considered in terms of decomposition of precursors. In PECVD deposition, the film deposition rate depends on the concentration of activated reactants on the substrate surface. At low supply flow rate, plasma power can completely dissociate the incoming supply precursors, and the deposition rate may not depend on plasma power. At high supply flow rate, the RF power can not keep up with the supply of precursors, and increase of RF power may result in higher dissociation of the precursors and higher density of reactive species, which accounts for the larger deposition rate.

.

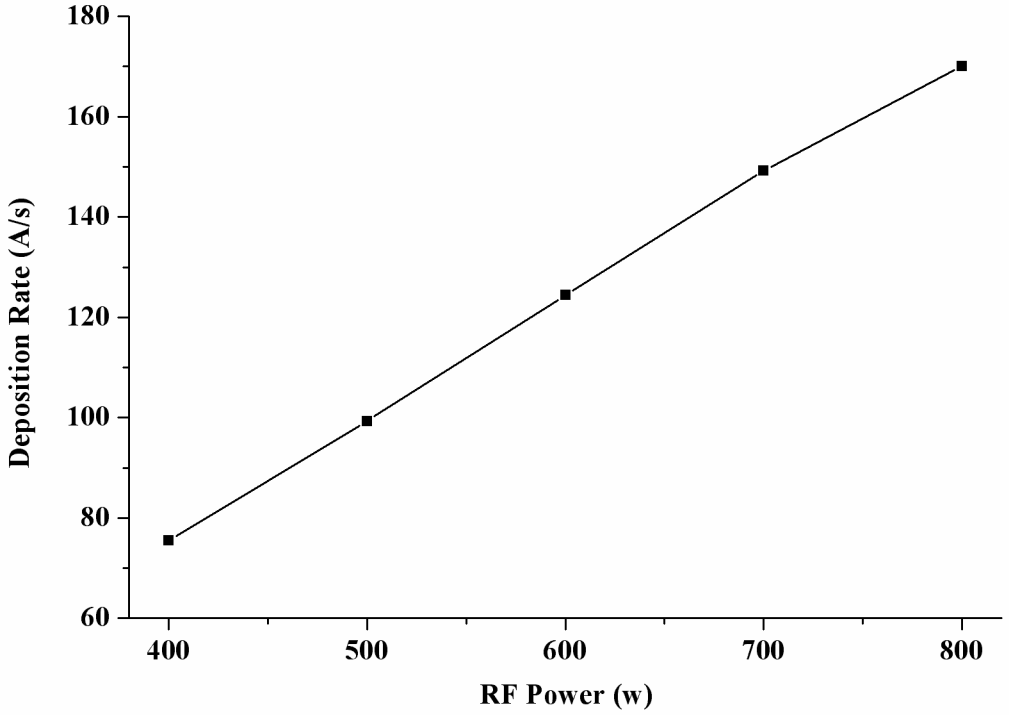

Fig. 5.12 Deposition Rate of SiOCH films as a Function of RF Power

Figure 5.13 details the FTIR absorption spectra over the range of 400~4000 cm^{-1} of SiOCH low k film deposited at different RF power with other condition fixed. All the films show very similar bonding structure, and their absorbance bands are quite typical for the PECVD SiOCH material and were identified as previous chapter. The shoulder in the higher frequency side of the Si-O stretching band (the dominating band of such films) is attributed to the porosity of an oxide with caged Si–O bonds and supports the presence of microvoids in the films. Such shoulder becomes less obvious in higher RF power, which suggests that less porosity exist if the RF power increases.

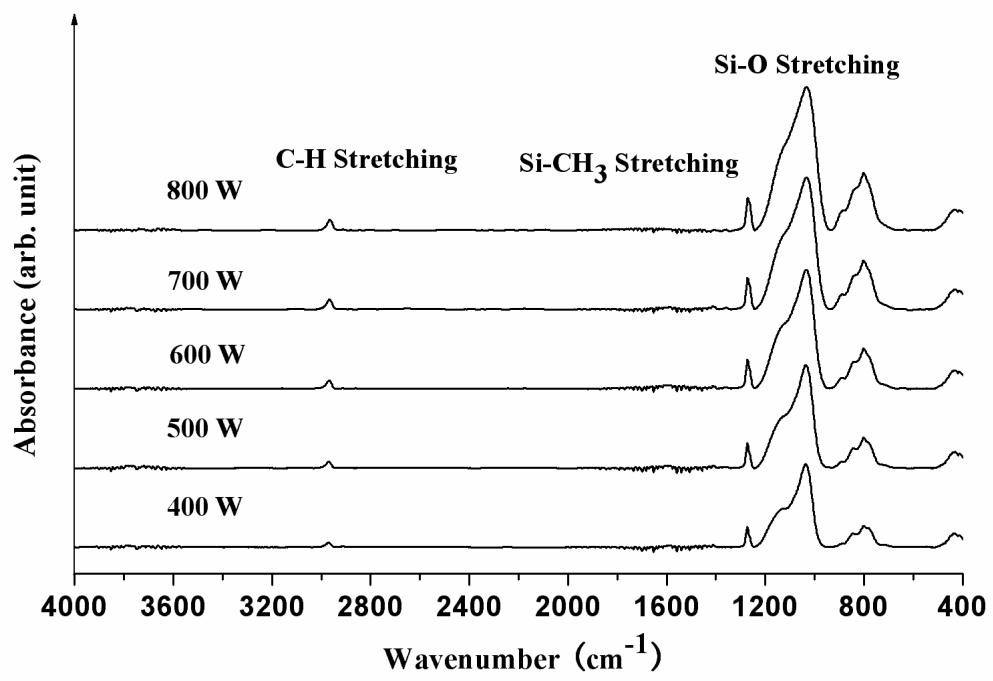

Fig. 5.13 FTIR absorption spectra of SiOCH films deposited at different RF power

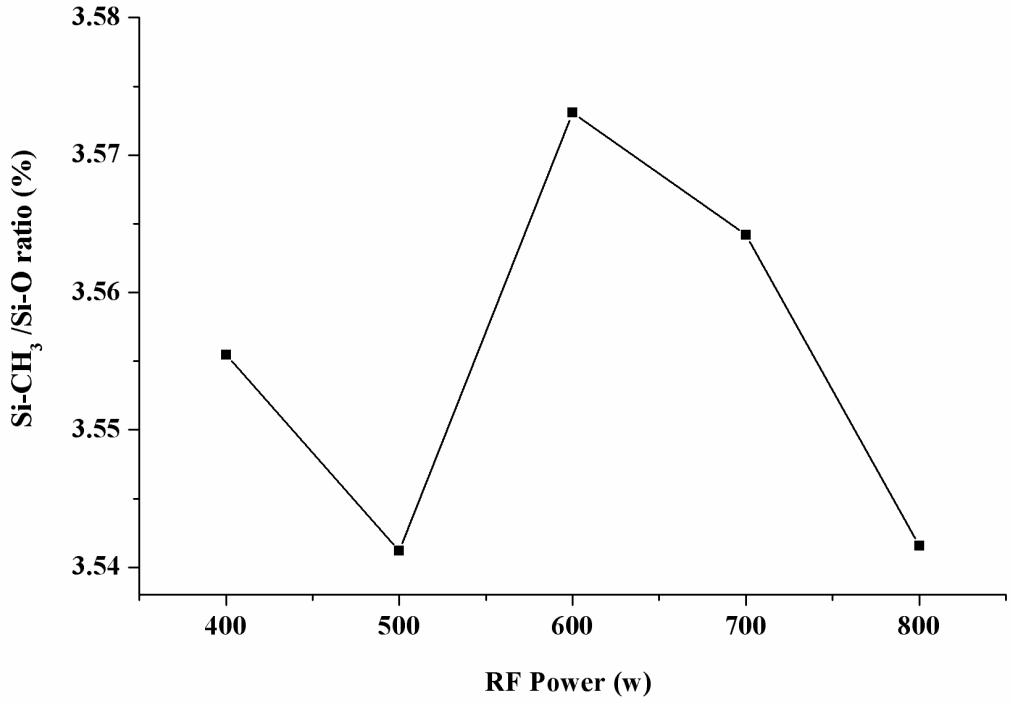

Fig. 5.14 FTIR absorption integrated area ratio of the Si-CH_3/Si-O stretching band of SiOCH films as a Function of RF power

The sharp peak at about 1273 cm^{-1} in figure 5.13, corresponding to stretching vibration modes of Si-CH_3, is the characteristic absorption band of SiOCH films. The relative concentration of Si-CH_3 bonds incorporated in SiOCH composite films could be estimated from the FTIR absorption integrated area ratio of the Si-CH_3/Si-O stretching band, and the result is shown in figure 5.14. There is no significant variation in the absorption integrated area ratio of Si-CH_3/Si-O stretching bands when the RF power changes.

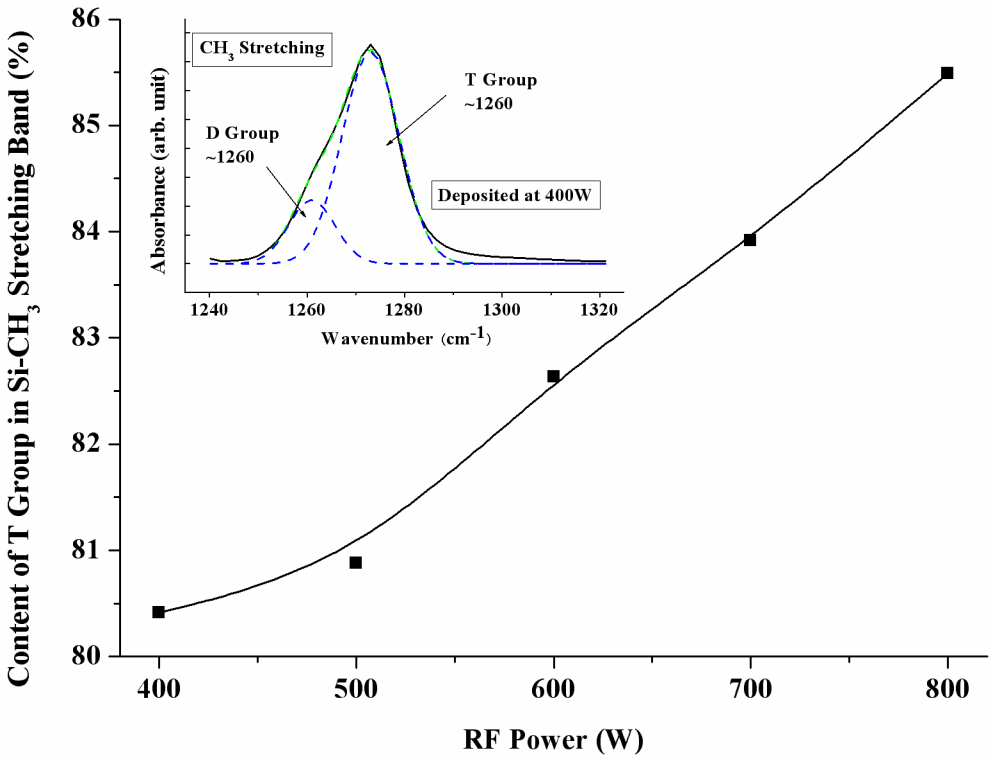

Fig. 5.15 Content (%) of T group in Si-CH_3 stretching band of SiOCH films as a function of RF power

The Si-CH_3 stretching band in the 1240 cm^{-1} to 1300 cm^{-1} region of the FTIR spectrum can vary in position based upon the degree of oxidation of the silicon atom,

with higher wavenumber as oxidation increases [151]. The configuration of silicon in $SiO_x(CH_3)_{4-x}$ has three most basic possibilities with either mono-, di-, or trisubstitution of the silicon atom by oxygen atom, which is represented as "M", "D" and "T" group respectively. The typical band position in the FTIR spectrum is 1250 cm^{-1} for M group ($OSi(CH_3)_3$), 1260 cm^{-1} for D group ($O_2Si(CH_3)_2$), and 1270 cm^{-1} for T group ($O_3Si(CH_3)$) [151]. A mixture of these three configurations is possible in a plasma enhance CVD film. Since all the FTIR absorption spectra of Si-CH_3 stretching bands in figure 5.13 distribute between 1250 cm^{-1} and 1290 cm^{-1}, M group ($OSi(CH_3)_3$) at 1250 cm^{-1} in the films can be negligible. Therefore, the Si-CH_3 band can be de-convoluted into D and T groups with Gauss fitting curve as shown in the insertion graph in figure 5.15. To investigate more detail of the Si-CH_3 stretching band, the relative concentration (%) of T group is calculated from the ratio of integration area of T group and the whole Si-CH_3 stretching band, and shows in figure 5.15. It can be seen that the T group ($O_3Si(CH_3)$) dominates the structure of the configuration with more than 80%, and increases monotonously from 80.4% to 85.5% as the RF power increases from 400 W to 800 W. The absence of M group ($OSi(CH_3)_3$) in the deposited films indicates that at lease one -CH_3 bond in the 3MS ($HSi(CH_3)_3$) precussor is oxidated before it is incorporated in to SiOCH films. Since the relative concentration of Si-CH_3 bonds almost remains constant at different RF power as seen early, the increase of T group ($O_3Si(CH_3)$) at higher RF power may due to the further break of Si-CH_3 in the 3MS precussor and more oxidation degree of the CH_3-contained species.

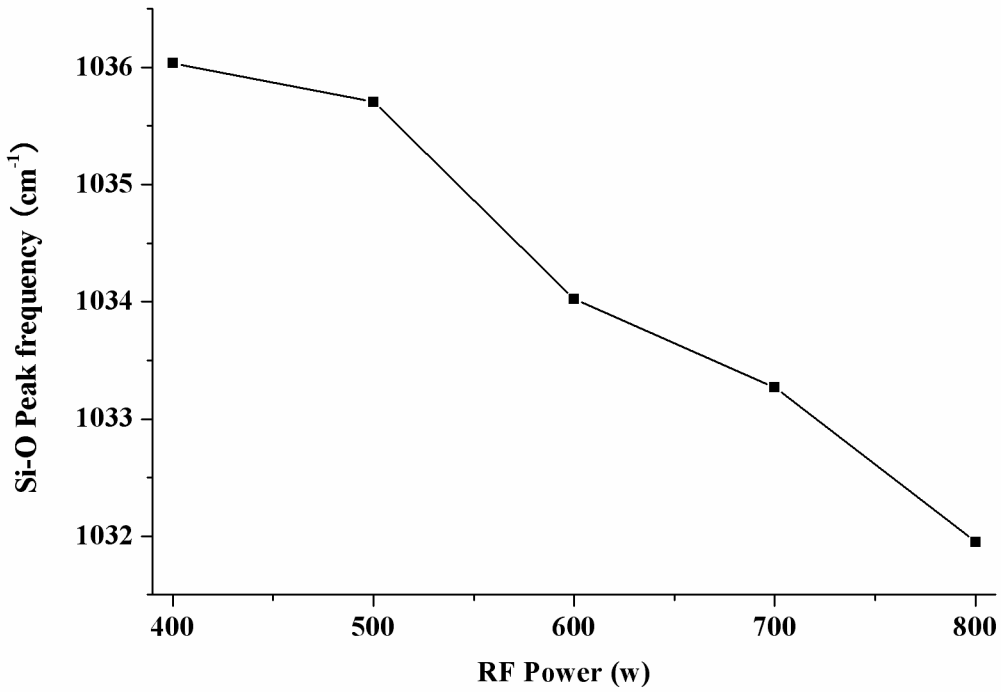

Fig. 5.16 Position of Si-O stretching band of SiOCH films as a function of RF power

The deposition conditions can affect the position of the peaks in the FTIR spectrum. Figure 5.16 demonstrates the peak frequency of the Si-O stretching absorption band as a function of RF power. The frequency of the Si-O stretching peak at about 1034 cm^{-1} shift slightly from about 1036 cm^{-1} to lower frequency 1032 cm^{-1} (red-shift) as the RF power increases. These frequency shifts in FTIR spectra is ascribe to the change of the bonding characteristics, such as bond angle and bond length, as discussed in section 5.3.1. Section 5.3.1 also suggests that increase of film density and/or carbon content in silicon dioxide matrix will result in red-shift of the Si-O stretching peak. However, no significant change is found in the carbon content of SiOCH films when RF power changes as seen in figure 5.14. Therefore, the red-shift of the Si-O stretching peak with increase of RF power shall be ascribe to the

increase of film density, which is verified later from the variation of refractive index shown in figure 5.17.

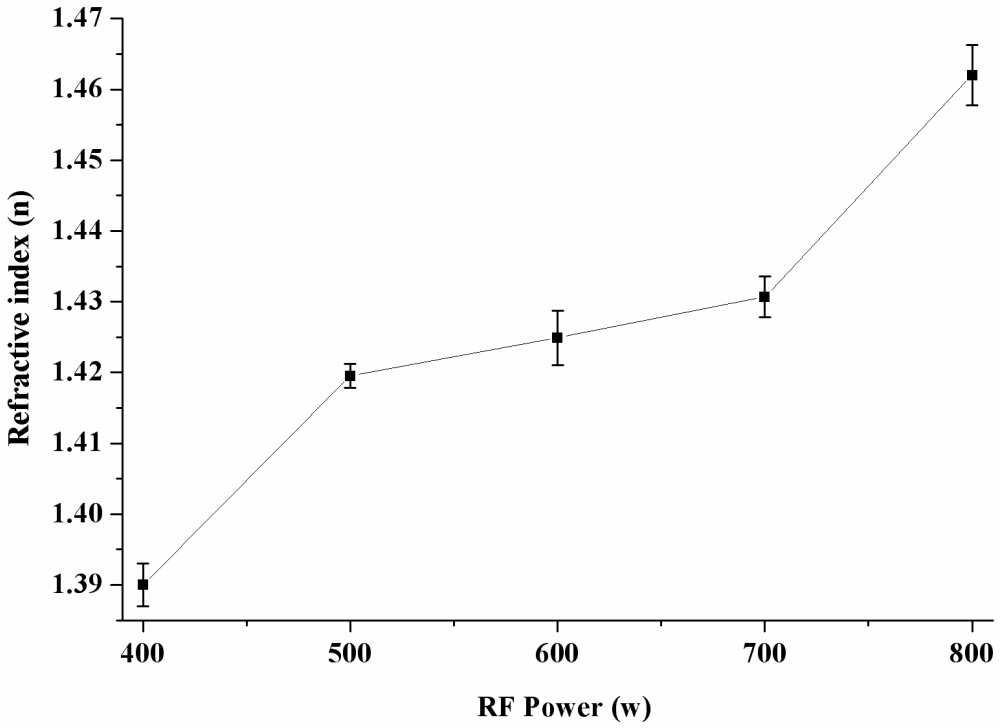

Fig. 5.17 Refractive index of SiOCH films as a function of RF power

Figure 5.17 shows the refractive index with error bar at 632.8 nm of SiOCH films as a function of RF power. It can be found that the films with higher RF power exhibit higher refractive index values. The variation in the index of refraction in SiOCH films depicted in figure 5.17 can be ascribed to the changes in the density, structure, and/or bonds of the films. The incorporation of CH_3 groups is believed to terminate the O–Si–O bonding network and results in loosely linked structures with more voids, lower mass density, and lower refractive indices. However, the variation of CH_3 bond concentration is so small that the effect of bonds in the films could be ignored, so the film density is the main factor for the change of refractive index. Since high RF plasma power in the reactive chamber will increase the incident

energies of charged reactive species generated from the precursor by plasma, it could make the SiOCH film denser, which is consistent with the smaller shoulder of Si-O stretching band in higher RF power shown in figure 5.13. The increased densification of deposited films could also result from the increase of cross-linking by plasma at elevated power. As a result, the refractive index should increase with RF power.

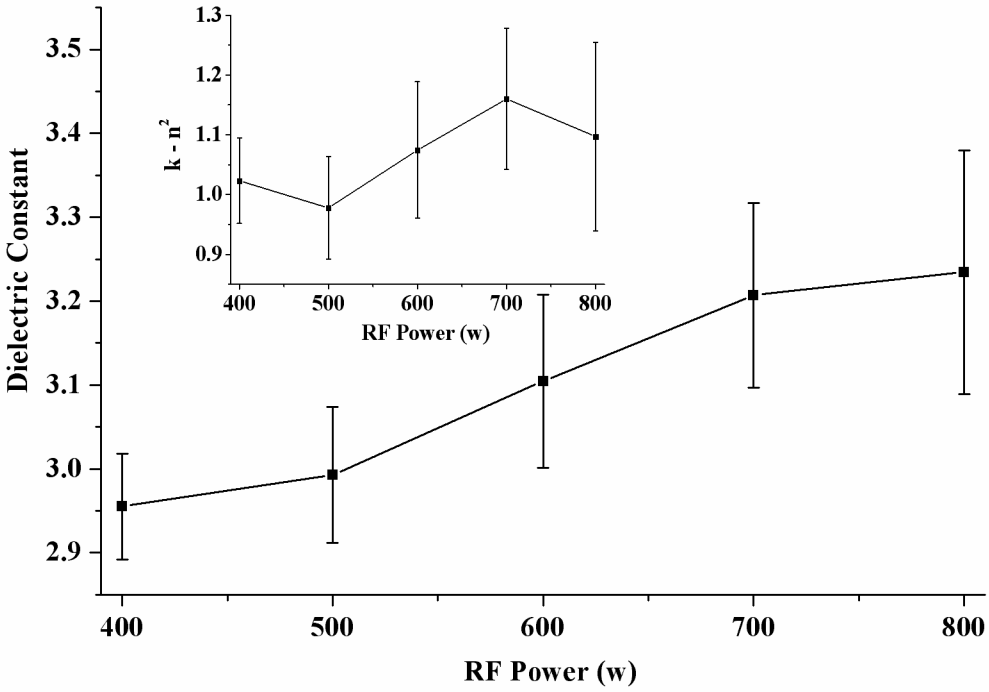

Fig. 5.18 Dielectric constant of SiOCH films as a function of RF power

Figure 5.18 shows the dielectric constant with error bar of SiOCH films as a function of RF power. It reveals that the dielectric constant of SiOCH film increases as the RF power increases. The dielectric constant is measured at frequency of 0.9216 MHz using conventional electrical capacitance in the accumulation region. It is well known that the dielectric constant is a frequency-dependent intrinsic material property. At low frequency (e.g. 0.9216 MHz), dielectric constant is usually divided

into three parts: dipolar, ionic and electronic polarizations as discussed in Chapter two. At visible optical range, electronic polarization is the only contribution to the dielectric constant, which is equal to the square of refractive index. Therefore, the change of refractive index provides a clue for determination of how the dielectric constant changes with the RF power. If the square of refractive index is excluded from the dielectric constant, the remaining part ($k-n^2$) of dielectric constant should be the contribution of dipolar and ionic polarization. The insertion diagram in figure 5.18 demonstrates that the variation of $k-n^2$ of SiOCH films as a function of RF power is within err bar and could be negligible. It means that the variation of dipolar and ionic polarization with RF power shall be ignorant. Therefore the increase of dielectric constant with the increase of RF power was mainly due to the increase of refractive index which has been ascribed to the increase of film density in early discussion.

Figure 5.19 shows the relationship of the hardness and elastic modulus of SiOCH films to RF power. Both the hardness and Young's modulus increase with the increase of RF power. With the change of plasma power from 400 to 800 W, hardness increase from 0.97 to 1.51 GPa and E-modulus increase from 6.85 to 13.9 GPa. It is believed that with high RF power, the energies of the charged reactive radicals in the deposition chamber and incident onto the surfaces of the growing films increase, resulting in the formation of films with higher density and thus higher hardness and Young's modulus values.

More detailed analysis of the bonding structure could explain the hardness and Young's modulus results. The average connectivity number, <r>, which is defined as

the average number of bonds per network forming atom, could be used to quantitatively investigate the change in the bonding structure within the framework of the continuous random network theory [152-153]. If the average connectivity number increases above 2.4 for solids in which all atoms are able to form two or more bonds, the system will transitions from an underconstrained (nonrigid) state to an overconstrained (rigid) state and shall have superior mechanical properties [154]. For example, the tetrahedral (SiO_4), a fully networked structure of silicon dioxide (SiO_2), has a connectivity number of 2.67, thus holding excellent mechanical properties.

As a simple example to calculate the average connectivity number, in the tetrahedral (SiO_4) of SiO_2, silicon bonds with four oxygen atom, and each oxygen has two bonds with one bond linking the silicon within local tetrahedral structure and another bond liking silicon in the adjacent network node, so, all the silicon and oxygen atoms take part in the network formation. To avoid double counting, each oxygen atom is counted as half, and the number of network forming atoms is three for the tetrahedral (SiO_4) of SiO_2. The sum number of bonds of its network forming atoms is 8 (one silicon has 4 and each oxygen has 2). Therefore, average connectivity number of the tetrahedral (SiO_4) is 2.67 (8 bonds/3 atoms).

For our SiOCH films, the calculation of network forming atoms should exclude carbon and hydrogen. The structure of SiOCH film could be described as $SiO_x(CH_3)_{4-x}$ if all the carbon atoms are assumed to be in the form of methyl groups bound to silicon. The carbon atom does not bond to any atom outside the local $SiO_x(CH_3)_{4-x}$ structure, whereas the hydrogen has only one bond thus no contribution for any network. Therefore, both the carbon and hydrogen atom in methyl groups,

which is usually described as termination groups of network, are considered non-network forming and can not be counted for such analysis in $SiO_x(CH_3)_{4-x}$ structure. For T group ($O_3Si(CH_3)$), the total number of network-forming atom is 2.5 (one silicon and 3/2 oxygen), and the bond number is 6 (1si X 3 bonds + 1.5oxygen X 2 bonds), thus giving average connectivity number of 2.4 (6/2.5). Similar calculation of D group ($O_2Si(CH_3)_2$) gives average connectivity number of 2, as would be expected for a linear structure without branch points. So, the SiOCH sample with more T group should have larger average connectivity number.

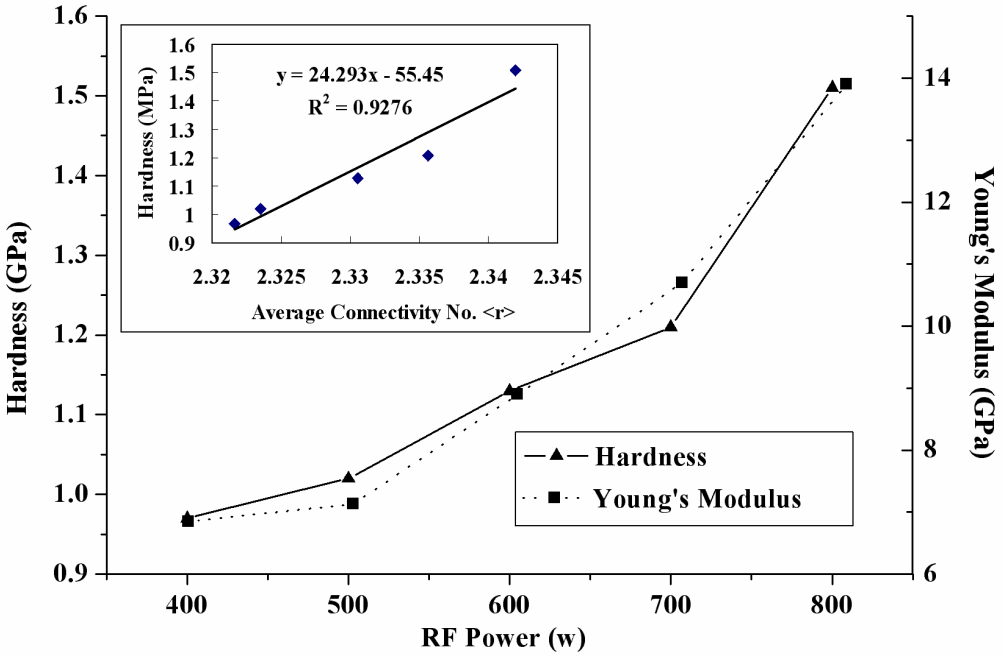

Fig. 5.19 Hardness and Young's Modulus of SiOCH films as a function of RF power

As indicated early, there are T and D groups in our SiOCH films, and their content (%) of each sample could be obtained from the deconvolution of Si-CH_3 stretching band (seen in figure 5.15). With the connectivity number of each group (T

with 2.4, D with 2), the average connectivity number of each film is simply the sum of the weighted contributions from every groups in the sample. The correlation between hardness and average connectivity number <r> is very strong as shown in the insertion diagraph of figure 5.19. As the RF power increases, the average connectivity number increases so as to improve the mechanical properties, but the carbon content almost remains constant without much deteriorating dielectric constant. Therefore, it is possible to get larger the average connectivity number for better mechanical properties without sacrifice of other properties if the deposition condition and chemistry are carefully optimized

5.4 Summary

SiOCH low-k thin films are deposited with PECVD at different gas flow rates of trimethylsilane (3MS) and oxygen with other condition fixed. Lowest dielectric constant and refractive constant are obtained at O_2/3MS gas flow rate of 100~150/600, but the hardness and Young's modulus are also weakest at this deposition condition. As the oxygen gas flow rate increases, deposition rate increases with less incorporation of carbon into the films, and the surface of the films also become more hydrophilic and rougher.

The effect of RF power on the properties of PECVD SiOCH films is also investigated. As the RF power increases, the deposition rate linearly increases but no significant variation of CH_3 content is found. The mechanical properties become much better with limited sacrificing of the electrical constant and refractive index.

Chapter 6

Conclusions and Recommendations for Future Work

6.1 Conclusions

The multilevel interconnect system of advanced integrated circuit in deep submicron region requires low permittivity (low k) materials to act as interlayer dielectric to reduce the propagation delay time, cross-talk noise and power dissipation. This project has investigated comprehensively the properties of carbon-doped hydrogenated silicon oxide (SiOCH) low k material deposited in plasma-enhanced chemical vapor deposition (PECVD) system with trimethylsilane (3MS) and oxygen as precursors at different deposition conditions. The deposition rate, bonding structure, electrical and mechanical properties, together with their relationships, have been studied with several techniques including nanoindentation, ellipsometry, atomic-force microscope (AFM), Fourier transform infrared (FTIR) spectroscopy, contact angle and C–V measurement techniques.

6.1.1 Influence of deposition temperature on the properties of SiOCH films

As the temperature increases from 200 to 400 ^{0}C, the deposition rate of SiOCH low k film is found to decrease more than 67%, and follows a first exponential decay function with the temperature (^{0}C), which has apparent activation energy of -0.157 eV. The SiOCH films prepared at lower temperature show lower dielectric constant and refractive index, but the mechanical properties become poorer,

which can be seen from the significant decrease of the hardness and Young's modulus. FTIR spectra reveal that more –CH and $–CH_3$ groups are introduced into the SiO_2 network of the films at lower deposition temperature. The –CH and $–CH_3$ groups and cage structure of Si–O bonds in the films are thought to be responsible for lowering the dielectric constant, refractive index, hardness and Young's modulus. Variation of dielectric constant is within 5% (from 3.12 to 3.26), whereas the variation of hardness is 500% (from about 0.25 Gpa to 1.25 Gpa).

The as-deposited films deposited at 350^0C are thermally stable in terms of FTIR spectra, thickness, dielectric constant and refractive index after annealing for 30 min at as high temperature as 500^0C, which exceeds the highest temperature (400–450^0C) encountered during typical interconnect processing steps. When the annealing temperature increases above 600^0C, thermal energy can significantly break Si-CH_3, Si-C, Si-H, and C-H bonds, which resulting in change of composition, shrinkage of thickness, and higher dielectric constant.

6.1.2 Effect of oxygen gas flow rate on the properties of SiOCH films

FTIR spectra reveal that the relative carbon content decreases monotonously from 3.8% to 2.7% as the oxygen gas flow rate increases from 30 to 700 sccm. The dielectric constant of SiOCH films ranges from 3.1 to 3.65, and the hardness varies from 1.76 GPa to 2.58 GPa. The lowest dielectric constant and refractive index can be obtained at O_2/3MS flow rate ratio of about 100:600 sccm, but hardness and Young's modulus become worst at this gas flow rate region. At lower O_2/3MS flow rate ratio region, the dielectric constant, refractive index, and hardness are very high, which

may due to some SiC phase in the SiOCH films. At higher O_2/3MS flow rate ratio region, the dielectric constant and refractive index of SiOCH films increase significantly and is closed to that of SiO_2. As the oxygen gas flow rate increases, the deposition rate and surface roughness of the films increase, and the films become more hydrophilic due to increase of polar component of the surface energy. The contact angle of water with SiOCH film monotonously decreases from 54.8 to 47.6 as the oxygen flow rate increases 30 sccm to 700 sccm. The variation of contact angle is more dramatic at lower oxygen flow rate than that of higher oxygen flow rate.

6.1.3 Impact of RF power on the properties of SiOCH

Increments of the deposition rate, refractive index, dielectric constant, hardness and Young's modulus, are observed at the higher RF plasma power. These effects are attributed to enhancement of precursors' decomposition and ionic bombardment, which cause the change in mass density and bond structure in the film. With the change of plasma power from 400 to 800 W, hardness increases from 0.97 to 1.51 GPa and dielectric constant increases from about 2.95 to 3.23. The increase of dielectric constant with the increase of RF power is mainly due to the increase of refractive index which has been ascribed to the increase of film density, whereas the variation of dipolar and ionic polarization with RF power shall be ignorant. Although the Si-CH_3 content in the film shows no obvious variation with the RF power, T group ($O_3Si(CH_3)$) in the films is found to increase linearly as the RF power increases, which is thought to result in higher hardness and Young's Modulus. It is found that the mechanical properties become much better with limited sacrificing of the electrical constant and refractive index at high RF power.

6.2 Recommendations for Future Work

This work has touched on a few of many technical challenges that must be resolved before SiOCH low k material can be successfully implemented in advanced interconnect system. As the extensions of this project, the following proposals should be useful, relevant and complementary to industrial research.

This study has revealed the change of bonding structure at different deposition conditions, and the presence of possible porosity or micro voids especially after annealing films. Further investigation of deposition kinetics study would lead to more insights of PECVD process of SiOCH low k material, and give more precise understanding on how deposition conditions affect the microstructure and properties of SiOCH films. Detail exploration of microstructure should focus on the relative amount of bonding and species, the amorphous and semi crystalline phase, voids or pore size and its distribution, and different pore conditions (open or closed).

The integration of SiOCH low k materials will include lots of process steps, such as dry resist removal processes (ashing) and sputter and reactive pre-clean, which involves plasma treatment. Further study should assess the interactions between SiOCH low k material and the plasma treatment, and how the plasma treatment conditions (gas species, power, pressure, time, etc.) affect the properties of the SiOCH low k materials.

The most important parameter of low k materials is the dielectric constant. If the SiOCH film is structurally anisotropic, the electrical properties may exhibit directional dependences with different dielectric constant in lateral (in-plane) and

vertical (out-of-plane) direction. Moreover, the dielectric constant is the function of frequency, and the high-performance IC benefiting from low k dielectrics will invariably operate at high frequencies usually exceeding one GHz. It is very important to carefully investigate the dielectric constant and its anisotropy at these high frequencies region. In this work, the dielectric constant is evaluated at very low frequency (0.9216 MHz) only in vertical direction. However, the same electrical measurements at GHz frequencies are greatly complicated duo to test setup impedance mismatches, on-chip parasitics, and dielectric loss (imaginary component of dielectric constant).

Adhesion between SiOCH low k materials with adjacent layers is crucial for integration and reliability. Poor adhesion may result in gap or delamination during fabrication or operation. The adhesion strongly depends on the film surface condition, such as roughness, bonding structure. Surface energy is one of the main parameter to evaluate the surface condition. This work has touched on the investigation of surface energy. There are ample opportunities for more detail study of surface properties.

The research and development of low k dielectric applications in advanced multilevel interconnect leave a wide effort with much progress as the semiconductor device continuously scaling down. It is hoped that the findings in this work have contributed somewhat to the growing pool of knowledge in the field of semiconductor.

List of Publications

1. T.K.S. Wong, B. Liu, B. Narayanan, V. Ligatchev, R. Kumar, "Investigation of deposition temperature effect on properties of PECVD SiOCH low-k films", Thin Solid Films, 462-463 (2004), pp.156--160.

2. V. Ligatchev, T. K. S. Wong, B. Liu, Rusli, "Atomic structure and defect densities in low dielectric constant carbon doped hydrogenated silicon oxide films, deposited by plasma-enhanced chemical vapor deposition" Journal of Applied Physics,Vol.92, No.8, (2002), pp.4605--4611.

3. V. Ligatchev, T.K.S. Wong, Rusli, B. Liu, "SiC-Like Phase and Room-Temperature Photoluminescence of Low-K SiOCH Films", Mat. Res. Soc. Symp. Proc. Vol. 737 © 2003 Materials Research Society, F3.39.1-- F3.39.6.

4. V. Ligatchev, T.K.S.Wong, Rusli, B. Liu, K. Ostrikov, "Nano-Scale Morphology and Electron Spectrum of Defect States in Low-k SiOCH Films", Mat. Res. Soc. Symp. Proc. Vol. 737 © 2003 Materials Research Society, F3.41.1-- F3.41.6.

Bibliography

1. R. H. Dennard, F.H. Gaensslen, H.N. Yu, V.L. Rideout, E. Bassous, A.R. Leblanc, IEEE J. *Solid-State Circuits*, SC-9 (1974), pp. 256.
2. D.C. Edelstein, G.A. Sai—Halasz, and Y-J. Mii, IBM J. *Res.Dev*. 39(4) (1995), pp.383.
3. S.R. Wilson and C.J. Tracy, ends., *Handbook of Multilevel Metallization for Integrated Circuits* (Noyes Publications, Park ridge, NJ, 1993).
4. M.T. Bohr, *Electron Devices Meeting 1995. international,* (1995), pp.241~244.
5. W. W. Lee and P. S. Ho, *Mater. Res. Soc*. Bulletin 22 (11), (1997), pp.19-23.
6. R. Liu, C. –S. Pai, H. –I. Cong, W. Lai, and E. Martinez, *Proc. Int. Interconnect Technol. Conf*. IEEE, (1999), pp. 21-23.
7. S.P. Jeng, R.H. Havemann, M.C. Chang, *Mater. Res. Soc. Symp. Proc.* 337 (1994), pp. 25.
8. M.E. Thomas, *Mater. Res. Soc. Symp. Proc.* 337 (1994), pp. 25.
9. M.E. Thomas, I.A. Sadat, S. Sekigahama, *IEEE IEDM 1990, Techn. Digest, IEEE, Parisipanny*, NJ, (1990) p. 351.
10. T. Sakurai, *IEEE Trans. Electr. Dev.* 40 (1993), pp. 118.
11. H. B. Bakoglu, *Circuits , Interconnections, and Packaging for VLSI*. Reading, MA: Addison-Wesley, 1990.
12. T. Quarles, A. R. Newton, D. O. Pederson, and A. Sangiovanni-Vincentelli, *SPICE 3B1 User's Guide,* EECS, Univ. of California, Berkeley, 1988.
13. Rabaey, Jan M., *Digital integrated circuits : a design perspective*, Upper Saddle River, N.J. : Prentice Hall, c1996

14. H.B. Bakoglu, *Circuits, Interconnection, and Packaging for LSI*, New York, Addison-Wesley, 1990.

15. G.K. Rao, *Multilevel Interconnect Technology*, McGraw-Hill, New York, 1993.

16. J.-Q. Lu, A. Kumar, Y. Kwon, E.T. Eisenbraun, R.P. Kraft, J.F. McDonald, R.J. Gutmann, T.S. Cale. P. Belemjain, O. Erdogan, J. Castracane, and A.E. Kaloyeros, "3-D Integration Using Wafer Bonding," in *Advanced Metallization Conference 2000 (AMC 2000)*, v16, 515-521, Eds. D. Edelstein, G. Dixit, Y. Yasuda and T. Ohba, The Materials Research Society, (2001).

17. J. D. Meindl, J. A. Davis, P. Zarkesh-Ha, C. S. Patel, K. P. Martin, and P. A. Kohl, "Interconnect opportunities for gigascale integration", *IBM J. Res Develop.* 46 (2002), pp. 245-264.

18. G.A. Sai-Halasz, *Proceedings of the IEEE*, 83 (1995), pp. 20.

19. T. N. Theis, *Electrochemical Processing in ULSI Fabrication I and Interconnect and Contact Metallization: Materials, Processes, and Reliability*, Vol. 98-6, *The electrochemical Society, Inc., Pennington, NJ*, (1999), pp. 1-11.

20. G.K. Rao, *Multilevel Interconnect Technology*, McGraw-Hill, New York, 1993.

21. Metals handbook, 8th edition, Vol. 1, *Properties and Selection of Metals/ prepared under the direction of the ASM Handbook Committee* ; Taylor Lyman, editor, Metals Park, Ohio : American Society for Metals, -c1961.

22. D.Edelstein, J. Heidenreich, R. Goldblatt, W. Cote, et al., *Proc. IEEE IEDM*, (1997) pp. 773.

23. C.H. Ting, T.E. Seidel, *Mater. Res. Soc. Symp*. 381 (1995) pp.3-9.

24. Davis S. Soane and Zoya Martynenko, *Polymers in Microelectronics: Fundamentals and Applications*, Elservier Science Publisher, 1989, pp. 119

25. N. H. Hendricks, "Organic Polymers for IC Intermetal Dielectric Applications", *Solid State Technology*, July 1995, pp. 117

26. N. H. Hendricks, "Low Dielectric Constant Materials for Intermetal Dielectric Applications: A status Report on the Leading Candidates", *Mat. Res. Soc. Symp. Proc*. 443 (1997), pp. 3

27. L. Peters, "Solving the Integration Challenges of Low-k Dielectrics," *Semiconductor International, November* 1999, pp. 56~64

28. L. Peters, "Low-k Dielectric: Will Spin-on or CVD Prevail?", Semiconductor International, June 2000, pp. 108~124

29. International Technology Roadmap for Semiconductors, International SEMATECH, 2001.

30. N. H. Hendricks, "Low Dielectric Constant Materials for Intermetal Dielectric Applications: A Status Report on the Leading Candidates", *Mat. Res. Soc. Symp. Proc*. Vol. 443,1997, pp.3.

31. L.J.Buckley, et al., *Mat. Res. Soc. Symp. Proc*. Vol. 381,1995, pp.111.

32. B.C. Aumann, in "*Proceedings of the 1st International VMIC Conference on Dielectrics for Multilevel Interconnections (DUMIC)*", 1995, pp295.

33. Ikeda et al., *J. electronic Mat*. Vol. 19 (1), 1990, pp45.

34. T. V. Herak, T.T. Chau, et al., *J. Appl. Phys.* Vol. 65, 1989, pp2459.

35. T. Furusawa, N. Sakuma, D. Ryuzaki, et al., *Proc. Internat. Interconnect Technol. Conf*. IEEE, Vol. 224, 2000, pp. 222.

36. A. Grill, V. Patel, *J. Appl. Phys*. Vol.85 (6), 1999, pp. 3314.

37. M.J. Loboda, *Microelectronic Engineering* Vol. 50, 2000, pp. 15.

38. W.-F. Yau, Y.-C. Lu, K. Liu, et al., *Proc. of Advanced Matallization Conference, Mater. Res. Soc.*, 1999. pp.379.

39. Kazuhiko Endo, Toru Tatsumi, *J. Appl. Phys*. Vol. 78 (2), 15 July 1995, pp. 1370.

40. P.B. Leezenberg, T.C. Reiley, G.W. Tyndall, *J. Vac. Sci. Technol*. A Vol.17, 1999, 17, pp.275.

41. S.-S. han, B.-S. Bae, *J. Electrochem. Soc*., Vol.148 (4), 2001 pp. F67.
42. N.P. Hacker, G. Davis, L. Figge, et al., *Mater. Res. Soc. Symp. Proc. San Francisco*. Vol. 476, 1997, pp.25.
43. J. Waeterloos, J. Meynen, B. Coenegrachts, et al., *Proc. of the third international dielectrics for ULSI multilevel interconnection conference, Santa Clara*, 1997, pp. 310.
44. D. M. Smith, J.Anderson, C.C. Cho, G.P. Johnston, and S.P. Jeng, "Preparation of Low-Density Xerogels at Ambient Pressure for Low k Dieletrics", *Mat. Res. Soc. Symp. Proc*. Vol. 381,1995, pp.261.
45. D. Burdeaux, P. Townsend, J. Carr, P. Garrou, *J. Electron. Mater*. Vol.19, 1990, pp.1357.
46. P.H. Townsend, S.J. Martin, J. Godschaix, et al., *Mater. Res. Soc. Symp. Proc. San Francisco*. Vol. 476,1997, pp.9.
47. K.J. Miller, H.B. Hollinger, J. Grebowicz, et al., *Macromolecules*, Vol.23, 1990, pp.3855.
48. C.T. Rosenmayer, J.W. Bartz, J. Hammes, *Mater. Res. Soc. Symp. Proc. San Francisco*. Vol. 476, 1997, pp.231.
49. N. H. Hendricks, "Low Dielectric Constant Materials for Intermetal Dielectric Applications: A Status Report on the Leading Candidates", *Mat. Res. Soc. Symp. Proc*. Vol. 443,1997, pp.3.
50. L.J.Buckley, et al., *Mat. Res. Soc. Symp. Proc*. Vol. 381,1995, pp.111.
51. B.C. Aumann, in "Proceedings of the 1st International VMIC Conference on Dielectrics for Multilevel Interconnections (DUMIC)", 1995, pp295.
52. Ikeda et al., *J. electronic Mat*. Vol. 19 (1), 1990, pp45.
53. T. V. Herak, T.T. Chau, et al., *J. Appl. Phys.* Vol. 65, 1989, pp2459.
54. T. Furusawa, N. Sakuma, D. Ryuzaki, et al., *Proc. Internat. Interconnect Technol. Conf*. IEEE, Vol. 224, 2000, pp. 222.
55. A. Grill, V. Patel, *J. Appl. Phys*. Vol.85 (6), 1999, pp. 3314.
56. M.J. Loboda, *Microelectronic Engineering* Vol. 50, 2000, pp. 15.
57. W.-F. Yau, Y.-C. Lu, K. Liu, et al., *Proc. of Advanced Matallization Conference, Mater. Res. Soc.*, 1999. pp.379.
58. Kazuhiko Endo, Toru Tatsumi, *J. Appl. Phys*. Vol. 78 (2), 15 July 1995, pp. 1370.

59. P.B. Leezenberg, T.C. Reiley, G.W. Tyndall, *J. Vac. Sci. Technol*. A Vol.17, 1999, 17, pp.275.

60. S.-S. han, B.-S. Bae, *J. Electrochem. Soc*., Vol.148 (4), 2001 pp. F67.

61. N.P. Hacker, G. Davis, L. Figge, et al., *Mater. Res. Soc. Symp. Proc. San Francisco*. Vol. 476, 1997, pp.25.

62. J. Waeterloos, J. Meynen, B. Coenegrachts, et al., *Proc. of the third international dielectrics for ULSI multilevel interconnection conference, Santa Clara*, 1997, pp. 310.

63. D. M. Smith, J.Anderson, C.C. Cho, G.P. Johnston, and S.P. Jeng, "Preparation of Low-Density Xerogels at Ambient Pressure for Low k Dieletrics", *Mat. Res. Soc. Symp. Proc*. Vol. 381,1995, pp.261.

64. D. Burdeaux, P. Townsend, J. Carr, P. Garrou, *J. Electron. Mater*. Vol.19, 1990, pp.1357.

65. P.H. Townsend, S.J. Martin, J. Godschaix, et al., *Mater. Res. Soc. Symp. Proc. San Francisco*. Vol. 476,1997, pp.9.

66. K.J. Miller, H.B. Hollinger, J. Grebowicz, et al., *Macromolecules*, Vol.23, 1990, pp.3855.

67. Arthur von Hipped, Dielectric Materials and Applications, 1954.

68. P. W. Atkins, Physical Chemistry, 5th Edition, Oxford University Press, New York, 1994.

69. Charles Kittel, Introduction to Solid State Physics, Chap. 13, 7th edition, John Wiley & Sons, New York, 1996.

70. J. D. Livingston, Electronic Properties of Engineering Materials, Chap. 4, Willey, New York, 1999.

71. M. A. Omar, "Elementary Solid State Physics", Addision-Wesley, New York, 1975, pp.58.

72. W. D. Kingery, H. K. Bowen, and D. R. Uhlmann, "Introduction to Ceramics," Chap. 18. Wiley, New York, 1976.

73. L. L. Hench and J. K. West, "Principles of Electronic Ceramics", Chap. 5, John Willey & Sons, New York, 1990.

74. K. J. Miller, H. B. Holinger, J. Grebowicz, B. Wunderlich, "Behavior of Adsorbed Macromolecules Between Two Solid Surfaces", Macromolecules 23, 1990, pp.3855.

75. S. H. Pine, "Organic Chemistry", New York, McGraw-Hill, 5th ed., 1987.

76. L. W. Hrubesh, L. E. Keene. and V. R. Latorre, J. Mater. Res. 8, 1993, pp.1736.

77. W.E. Sawyer, A. Man, U.S. Pat 229, 335 (1880).

78. J.W. Aylsworth, U.S. Pat 553, 296 (1896).

79. A. DeLodyguine, U.S. Pats 575,002 and 575,668 (1897).

80. H. F. Sterling, R.C.G. Swann, Solid-State Electron., 8, pp. 653 (1965).

81. Proceedings of the 1st International Symposium on Plasma Process-Induced Damage (Santa Clara, 1996).

82. U. Beck, D.T. Smith, G. Reiners and S.J. Dapkunas, *Thin Solid Films* 332 (1998), pp.164.

83. H. Ishikawa, S. Fudetani and M. Hirohashi, *Appl. Surf. Sci.* 178 (2001) pp.56.

84. X. Chudoba, N. Schwarzer, F. Richter and U. Beck, *Thin Solid Films* 377/378 (2000) pp. 366.

85. M.J. Loboda, *Proc. of Advanced Matallization Conference*, Mater. Res. Soc., (1999). P. 371.

86. H. Dun, P.Pan, F.R. White, and R.W.Douse, Mechanisms of Plasma-Enhanced Silicon Nitride Deposition Using SiH_4/N_2 Mixture, J. Electrochem. Soc. 128, No. 7, 1981, pp.1555-1563.

87. L. M. Han, J. S. Pan, S. M. Chen, N. Balasubramanian, J. Shi, L. S. Wong, P. D Foo, J. Electrochem. Soc., 148 (7) (2001) F148.

88. A. Grill, L. Perraud, V. Patel, C. Jahnes, C. Cohen, Mater. Res. Soc. Symp. Proc., 565 (1999) 107.

89. G. Socrates, Infrared Characteristics Group Frequencies, Wiley, New York, 1994, Chap 18.

90. C. Rau and W. Kulisch, Thin Solid Film, 249 (1994) 28.

91. P. G. Pai, S. S. Chao, Y. Takagi, G. Lucovsky, J. Vac. Sci. Technol. A 4 (3) (1986) 689.

92. F.L. Galeener, Phys. Rev. B 19, (1979), pp.4292.

93. G.Lucovski, P.D.Richard, D.V.Tsu, S.Y.Lin, and R.J.Markunas, J. Vac. Sci. Technol. A4, (1986) pp. 681.

94. M. J. Loboda, C. M. Grove, and R. F. Schneider, J. Electrochem. Soc.145, (1998) pp. 2861.

95. D. A. Neumayer, J. Appl. Phys. 90, (2001) pp. 1801.

96. A. Grill, L. Perraud, V. Patel, C. Jahnes, C. Cohen, Mater. Res. Soc. Symp. Proc., 565 (1999) pp.107.

97. Y. H. Kim, S. K. Lee, H. J. Kim, J. Vac. Sci. Technol. *A*. 18 (2000), pp.1216.

98. Byung Keun Hwang, Mark J. Loboda, Glenn A. Cerny, Ryan F. Schneider and Jeffrey A. Seifferly, Electrochemical Society Proceedings Volume 2000-5, pp.63.

99. Milton Ohring, Materials Science of Thin Films: Deposition and Structure, Chap. 6, 2nd Edition, Academic Press, San Diege, 2002.

100. W.S. Ruska, Microelectronic Processing, McGraw-Hill, New York, 1987.

101. H. Treichel, G. Ruhl, P. Ansmann, R. Wurl, Ch. Muller, M. Dietlmeier, Microelectronic Engineering 40 (1) (1998) pp.1.

102. Semiconductor International, August (1998).

103. R Bajaj, A. Zutshi, R. Surana, M. Naik and T. Pan, "Integration Challenges for CMP of Copper", *MRS Bull.* 27 (2002) pp.776-778.

104. R.K. Singh and R. Bajaj, "Advances in Chemical-Mechanical Planarization", *MRS Bull.* 27 (2002) pp.743-747.

105. J.H. Zhao, T.Ryan, P. Ho, A.J. McKerrow, W.Y. Shih, *J. Appl. Phys*. 85 (1999), p. 6421.

106. D. D. Burkey and K. K. Gleason, J. Appl. Phys. 93 (9) (2003) pp. 5413.

107. T. M. Moore, C. D. Hartfield, J. M. Anthony, B. T. Ahlburn, P. S. Ho, and R. Miller, Characterization and Metrology for ULSI Technology: 2000,Gaithersburg, MD, Melville, NY, 2000, pp. 431.

108. B.Arkles, Silicone Compounds Register and Review, Petrarch Systems, Bristol, PA, 1987.

109. J. C. Phillips, J. Non-Cryst. Solids 34 (1979) pp.153-181

110. M. F. Thorpe, J. Non-Cryst. Solids 57 (1983) pp.355-370.

111. Z.-C. Wu et al., J. Electrochem. Soc. 148, F127, (2001);

112. Z.-C. Wu et al., J. Electrochem. Soc. 148, F115, (2001).

113. T. Furusawa, D. Ryazaki, R. Yoneyama, Y. Homma, and K. Hinode, J.Electrochem. Soc. 148, F175, (2001).

114. L. M. Han, J.-S. Pan, S.-M. Chen, N. Balasubramanian, J. Shi, L. S.Wong, and P. D. Foo, J. Electrochem. Soc. 148, F148, (2001).

115. S. Sugahara, T. Kadoya, K.-i. Usami, T. Hattori, and M. Matsumura, J.Electrochem. Soc. 148, F120, (2001).

116. S. Sugahara, K.-i. Usami, and M. Matsumura, Jpn. J. Appl. Phys., Part 138, pp.1428, (1999).

117. E. T. Ryan, A. J. McKerrow, J. Leu, and P. S. Ho, MRS Bull. 22, pp.49, (1997).

118. M. Loboda and G. Toskey, Solid State Technol. 41, pp.99, (1998).

119. Licheng M. Han, June 27–29, 2000 VMIC Conference, 2000 IMIC–200/00/0401(c), pp. 401.

120. M.J.Loboda, Mater. Res. Soc. Symp. Proc. Vol 612, 2000, pp.371.

121. P. N. Sen and M. F. Thorpe, Phys. Rev. B 15, 1977, pp.4030.

122. G. Lucovsky, Philos. Mag. B 39, 1979, pp.513.

123. G. Lucovsky, M. J. Manitini, J. K. Srivastava, and E. A. Irene, J. Vac. Sci.Technol. B 5, 1987, pp.530.

124. I. Simon, *Modern Aspects of the Vitreous Silica* (Gordon and Breach, New York, 1975).

125. Y. H. Kim, M. S. Hwang, H. J. Kim, J. Y. Kim, Y. Lee, J. Appl. Phys. 90 (7) (2001), pp.3367-3370.

126. D. W. Oxtoby, N. H. Nachtrieb, and W. A. Freeman, *Principles of Modern Chemistry*, 2nd ed. (Saunders, Philadelphia, 1987).

127. W. D. Kingery, H. K. Bowen, and D. R. Uhlmann, *Introduction to Ceramics*, (Wiley, New York, 1976).

128. R. Zallen and M.L.Slade, Phys. Rev. B18, 1978, pp.5775.

129. V. Ligatchev, T. K. S. Wong, B. Liu, and Rusli, J. Appl. Phys. 92 (8) (2002), pp.4605-4611.

130. Zhen-Cheng Wu, Zhi-Wen Shiung, Chiu-Chih Chiang, et.al., Journal of the Electrochemical Society 148 (2001), F127.

131. S.-K. JangJean, Y.-L. Wang, C.-P. Liu, W.-S. Hwang, W.-T. Tseng,C.-W. Liu, Journal of Applied Physics 94 (2003), pp. 732–737.

132. P. Xu, K. Huang, A. Patel, S. Rathi, J. Ferguson, B. Tang, J. Huang, C. Ngai, and M. Loboda, Proc. of Advanced Materization Conference, MRS, (1999), pp.437-441.

133. P. Xu, K. Huang, A. Patel, S. Rathi, J. Ferguson, B. Tang, J. Huang, C. Ngai, and M. Loboda, Proceedings of the 1999 International Interconnect Technology Conference (IITC99), (1999), pp.109.

134. A. C. Ferrary et. al., Phys. Rev. B 62, (2000), pp.11089.

135. L.M. Han, J.-s. Pan, S.-M. Chen, N. Balasubramanian, J. Shi, L.S.Wong, P.D. Foo, J. Electrochem. Soc. 148 (7) (2001) F148–F153.

136. C. Y. Chang, and S.M. Sze, *ULSI Technology*, Chapter 5, (The McGRAW-HILL COMPANIES, INC, Singapore, 1996).

137. M. J. Loboda, *Mater. Res. Soc. Symp. Proc*., 612, (2000), pp.371.

138. S.M. Sze, *VLSI Technology*, 2nd edition, Chapter 6, (The McGRAW-HILL COMPANIES, INC, Singapore, 1988).

139. C. Cobianu and C. Pavelescu, Thin Solid Films, 117, (1984), pp.211.

140. T. Sherban, B. Sun, J. Blaine, C. Block, B. Jin, and E. Andideh, Proceedings, of the International Interconnect Technology Conference, IITC, 2001, pp.257.

141. S. Maitrejean, F. Fusalba, M. Patz, V. Jousseaume, and T. Mourier, Proceedings, of the International Interconnect Technology Conference 2002, pp.206.

142. C. Chiang, N.V. Lam, J.K. Chu, et al., *Proceedings of the Fourth International IEEE VLSI Multilevel Interconnection Conference*, Santa Clara, 1987, pp. 404.

143. Q. Ma, Q. Tran, C. Pan, et al., *Mater. Res. Soc. Symp. Proc., Low-Dielectric Constant Materials IV Pittsburgh: (MRS 1998)*, pp. 329.

144. T. Young, Philos. Trans. R. Soc. Lond. 9, (1805), pp.255.

145. J.S. Chen , S.P. Lau , Z. Sun , G.Y. Chen , Y.J. Li , B.K. Tay , J.W. Chai, Thin Solid Film, Vol. 398-399, (2001), pp.110.

146. http://www.jobinyvon.co.uk/ukdivisions/Contact/wafer.htm.

147. http://www.ipfdd.de/research/res12/adsa_p.html.

148. S. Wu, *Polymer Interface and Adhesion*, (Marcel Dekker, New York, 1982), pp. 178–181

149. Adachi, T. Arai, K. Kobayashi, J. Appl. Phys. 80, (1996), pp. 5422.

150. A.W. Neumann, Adv. Collid. Interface. Sci., 4, (1974), pp.438.

151. B. Arkles, *Silicone Compounds Register and Review*, (Petrarch Systems, Bristol, PA, 1987).

152. J. C. Phillips, J. Non-Cryst. Solids, Vol. 34, (1979), pp.153.

153. M. F. Thorpe, J. Non-Cryst. Solids, Vol. 57, (1983), pp.355.

154. G. H. Dohler, R. Dandoloff, and H. Bilz, J. Non-Cryst. Solids, Vol. 42, (1980), pp.87.